g-C₃N₄-Based Nanomaterials for Visible Light-Driven Photocatalysis

Santosh Kumar [1], Sekar Karthikeyan [1] and Adam F. Lee [2,*]

[1] European Bioenergy Research Institute, Aston University, Birmingham B4 7ET, UK;
s.kumar10@aston.ac.uk (S.K.); k.sekar@aston.ac.uk (S.K.)

[2] School of Science, RMIT University, Melbourne, VIC 3000, Australia

[*] Correspondence: adam.lee2@rmit.edu.au; Tel.: +61-(0)399252623

Abstract: Graphitic carbon nitride (g-C₃N₄) is a promising material for photocatalytic applications such as solar fuels production through CO_2 reduction and water splitting, and environmental remediation through the degradation of organic pollutants. This promise reflects the advantageous photophysical properties of g-C₃N₄ nanostructures, notably high surface area, quantum efficiency, interfacial charge separation and transport, and ease of modification through either composite formation or the incorporation of desirable surface functionalities. Here, we review recent progress in the synthesis and photocatalytic applications of diverse g-C₃N₄ nanostructured materials, and highlight the physical basis underpinning their performance for each application. Potential new architectures, such as hierarchical or composite g-C₃N₄ nanostructures, that may offer further performance enhancements in solar energy harvesting and conversion are also outlined.

Keywords: g-C₃N₄; photocatalysis; nanomaterials; CO_2 reduction; H_2 evolution; semiconductor; environmental remediation

1. Introduction

1.1. Background

Future energy production, storage and security, and combating anthropogenic environmental pollution, represent key global challenges for both developed and emerging nations [1,2]. Sunlight, an essentially limitless source of clean energy, has the potential to address both these challenges [3,4], and its utilization to this end entered mainstream science following breakthroughs in semiconductor light harvesting for photocatalysis by Honda and Fujishima in the 1970s [5–7]. This discovery led to extensive research into titania semiconductor photocatalysts, principally for water splitting and the degradation of aqueous or airborne organic pollutants under UV light irradiation [8–13]. However, efficient harnessing of visible light (the major component of solar radiation that reaches the Earth's surface) by photocatalysts to drive chemical transformations remains problematic [14–16] due to identifying suitable materials that possess narrow band gaps, high quantum yields, efficient charge carrier transport, and low rates of charge carrier recombination, and good thermo-, photo-, and chemical stability. The development of such low cost photocatalysts from earth abundant, and ideally non-toxic elements for visible light harvesting would unlock opportunities for their large-scale application to supplement existing renewable energy networks and pollution control systems.

1.2. Semiconductor Photocatalysis

Semiconductor photocatalysis refers to the acceleration of chemical transformations (most commonly oxidations and reductions) brought about through the activation of a catalyst, comprising a semiconductor either alone or in combination with metal/organic/organometallic promoters, through light absorption, with subsequent charge and/or energy transfer to adsorbed species. Note that the direct activation of reactants and intermediates through light absorption is the realm of photochemistry; in establishing whether a transformation is truly photocatalytic it is therefore crucial to establish that photons are absorbed by the catalyst rather than adsorbates [17,18]. In the photocatalytic production of so-called 'solar fuels', photoexcited charge carriers drive the conversion of water and CO_2 into H_2, CO, CH_4, CH_3OH and related oxygenates and hydrocarbons [19–21]. Such processes parallel those in nature wherein sunlight absorbed by chlorophyll in plants promotes starch and oxygen production from carbon dioxide and water), and are hence termed artificial photosynthesis (Figure 1). Photoexcited charge carriers can also either induce the total oxidation (mineralization) of organic pollutants such as those encountered in aquatic environments, either directly, or through the creation of potent oxidants such as hydroxyl radicals [22].
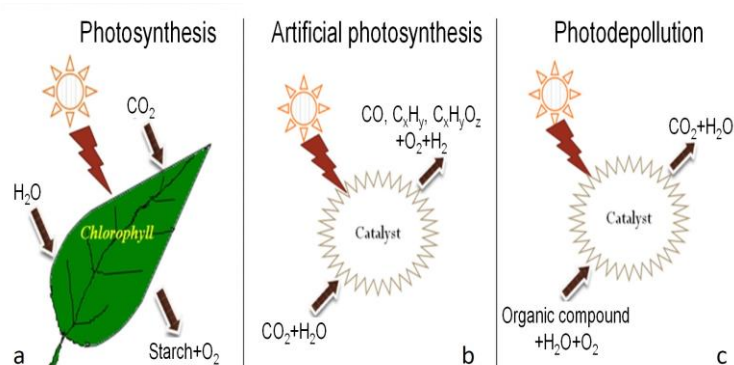

Figure 1. (**a**) Natural, and (**b**) artificial photosynthesis through water splitting and CO_2 reduction, and (**c**) photodegradation of aqueous organic pollutants.

1.3. Photocatalytic Mechanisms

Semiconductor photocatalysis is initiated by exciton formation following photon absorption and the excitation of electrons from the valence band into the conduction band (Step I). The resulting electron–hole pairs may recombine in either the bulk of the semiconductor, or at the surface, with the associated energy released through either fluorescence or thermal excitation of the lattice (Step II); recombination is the primary process that limits photocatalyst efficiency after photon capture. Electrons (and holes) that migrate to the surface of the semiconductor and do not undergo rapid recombination may participate in various oxidation and reduction reactions with adsorbates such as water, oxygen, and other organic or inorganic species (Steps III and IV) [9,10,23,24]. These steps are summarized below and illustrated in Figure 2:

Step I　　Light absorption　$SC + h\nu \rightarrow SC^*(e_{CB}^- + h_{VB}^+)$.
Step II　　Recombination　$e_{CB}^- + h_{VB}^+ \rightarrow h\nu + heat$.
Step III　Reduction　$Adsorbate + e_{CB}^- \rightarrow Adsorbate^-$.
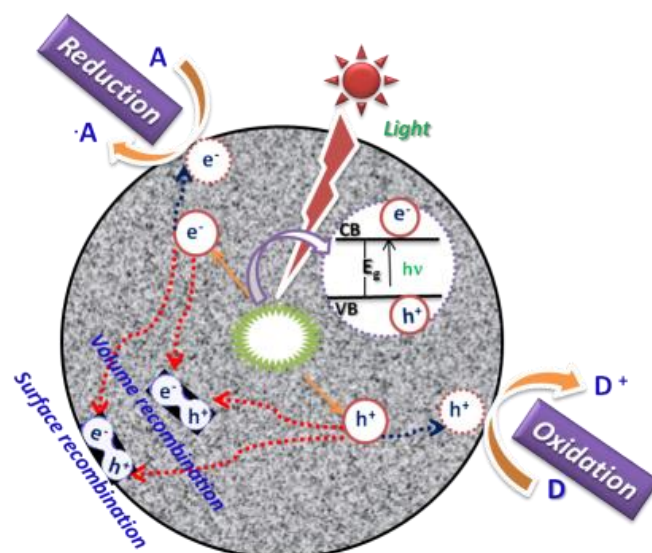Step IV　Oxidation　$Adsorbate + h_{VB}^+ \rightarrow Adsorbate^+$.

Figure 2. Principal photophysical processes for a semiconductor (SC) under light irradiation.

Oxidation and reduction reactions are fundamental to photocatalytic environmental remediation and solar fuel production, and are ultimately limited by the reduction potential of photoexcited electrons in the conduction band and oxidation potential of photogenerated holes in the valence band. The redox potential, band energies and gap of a semiconductor therefore largely determine the likelihood and rate of charge transfer, and hence are key design parameters for photocatalysts [12,25]. Although the underlying physics of space charge carriers and surface-electronic structure of photocatalysts varies between materials and applications, in essence, semiconductor photocatalysis represents interfacial reactions between electrons and holes generated through band gap excitation.

2. Photocatalytic Materials

The discovery of photocatalytic water splitting over titania electrodes under UV irradiation [5] has led to intensive research into explored H_2 production through this approach. Similarly, the first report on the photocatalytic oxidation of cyanide ions over TiO_2 powder [26] prompted a rapid expansion in environmental purification research and technologies, particularly for aqueous environments. In both cases, recent research has focused on identifying and developing alternative semiconductors to titania, offering superior performance under solar (rather than UV irradiation) [25]. Numerous semiconductors, including ZnO [27], Fe_2O_3 [28], WO_3 [29], $SrTiO_3$ [30], $NaTaO_3$ [31], CdS [32], Ag_3PO_4 [29], $BiPO_4$ [33], and $g-C_3N_4$ [34] are known photocatalysts, with their application dependent on their band gap (Figure 3). Despite a large body of literature, the practical utilization of such photocatalysts for solar fuels production or the degradation of organic pollutants remains a huge challenge due to poor visible light harvesting or efficient conversion of light energy to achieve chemical transformations [13,16,35].
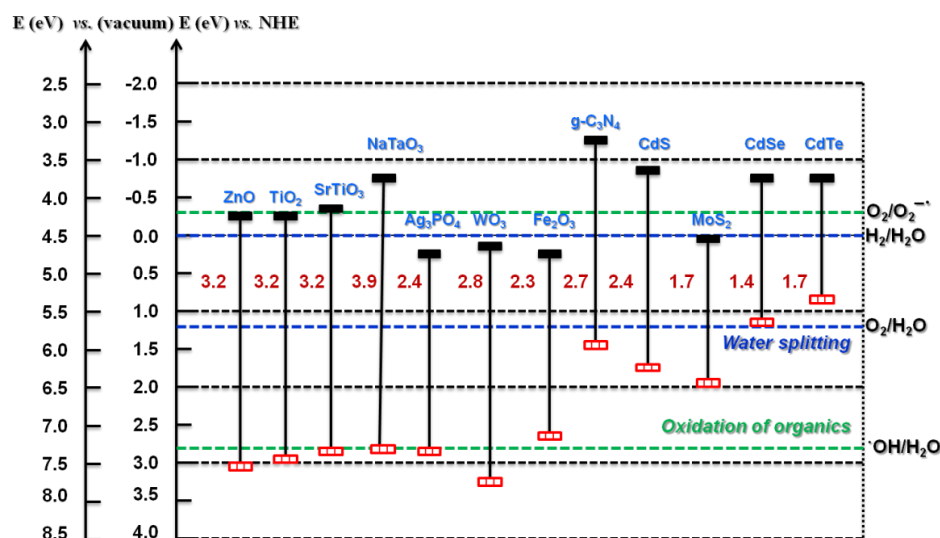
Figure 3. Band gap energy and band edge energies of different semiconductors.

3. Graphitic Carbon Nitride (g-C₃N₄)

Solar energy output reaching the Earth's surface is dominated by three regions (Figure 4) of the electromagnetic spectrum, UV (~5%), visible (~45%), and IR (~50%) [36]; visible light photocatalysis therefore offers the best opportunity to obtain maximum solar energy. However, most photocatalysts possess relatively wide band gaps, such as TiO_2 (3.0–3.2 eV) and are hence primarily active under UV irradiation (<385 nm) [8]. The quest for high performance visible light counterparts is reflected in the rapid growth of associated scientific papers and patents [8,10,15] for water splitting, CO_2 reduction and pollutants degradation [35]. Graphitic carbon nitride (g-C_3N_4) is a promising metal-free, polymeric semiconductor (Figure 5a) with a narrow band gap suited to visible light absorption (Figure 5b), [34] and amenable to large-scale synthesis. g-C_3N_4 may also be readily doped or chemically functionalized, permitting tuning of its photophysical properties, and in contrast to many other organic semiconductors, graphitic carbon nitride also exhibits high thermal and chemical stability to oxidation, even at temperatures of 500 °C. There is an extensive literature describing the synthesis of g-C_3N_4 and its derivatives for various applications. [37–43] This Review focuses on applications in photocatalytic environmental remediation and solar fuel generation, with an emphasis on emerging synthetic strategies to improve the photoactivity of g-C_3N_4-based nanostructures through controlling size, morphology, light absorption, charge separation, and ultimately surface reactions. Future research directions are also highlighted.
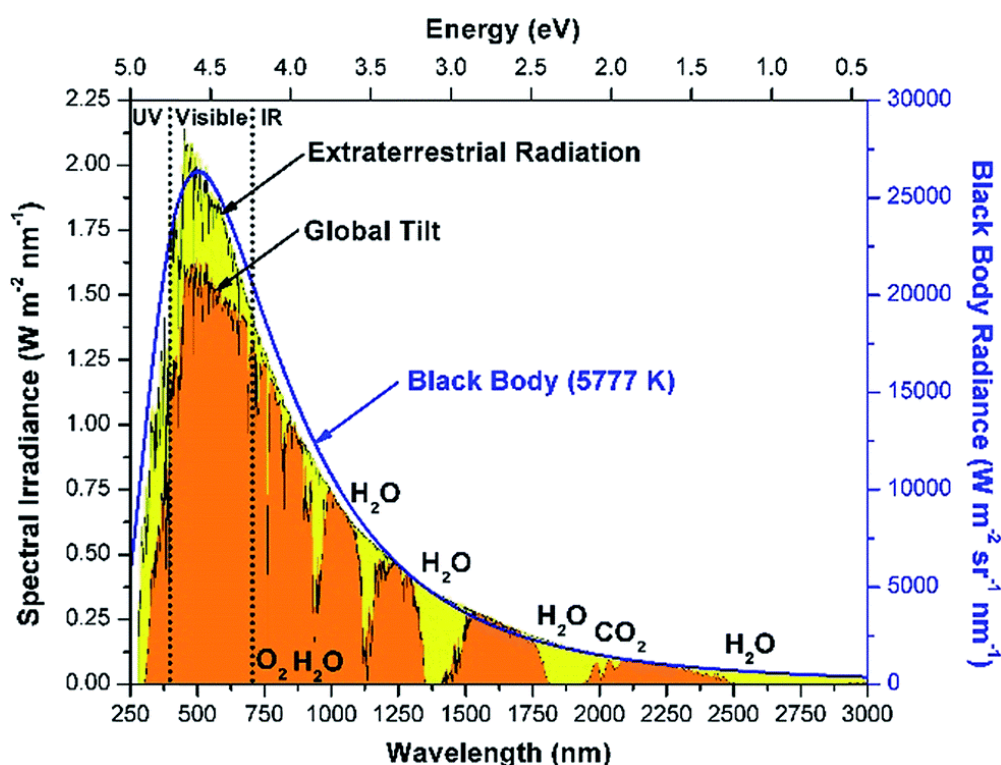
Figure 4. Spectral irradiance of solar light. Reproduced with permission from [36]. Copyright Royal Society of Chemistry, 2015.
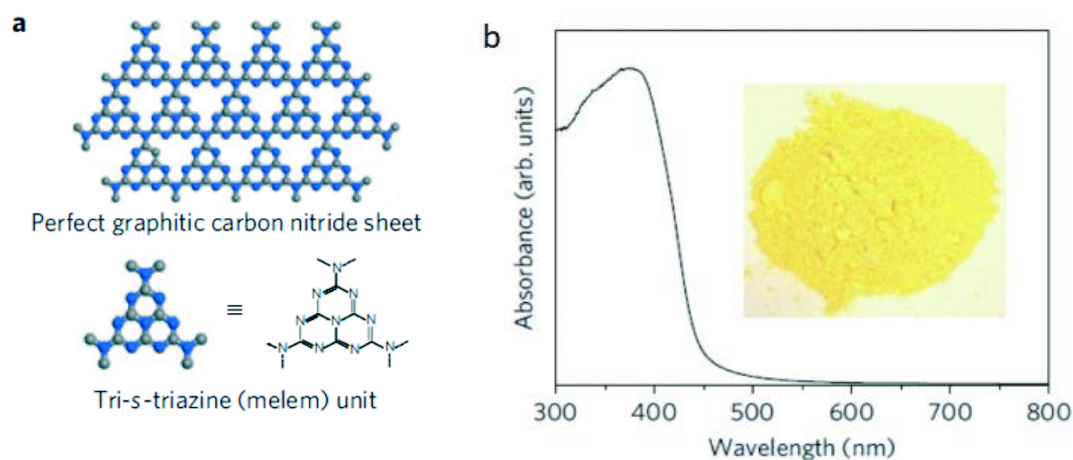

Figure 5. (**a**) Graphitic carbon nitride structure comprising melem units, and (**b**) UV-vis diffuse reflectance spectrum and image (inset) of g-C_3N_4. Reprinted with permission from [34]. Copyright Springer Nature, 2009.

4. g-C_3N_4 Nanostructures: Size and Shape

Engineering materials at the nanoscale is critical to the development of devices for the electronics [44], catalysis [45], biomedical [46], sensing [47], and smart materials [48] sectors, with nanoparticles now in widespread use across science and engineering [48–51]. A number of key aspects differentiate nanomaterials from their bulk analogues. Nanomaterials possess a high surface: bulk atom ratio, which heavily influences their thermodynamic properties resulting in, e.g., melting temperature depression, and elevated solid–solid phase transition temperature. Quantum confinement effects, which influence the electrical and optical properties of nanomaterials, arise from their evolving band structure and the emergence of atomistic like behaviour. Many heterogeneous catalysts exhibit strong size-dependencies due to quantum confinement [52], notably gold [53,54], high surface areas, and the

exposure of low-coordination, high energy sites [45,55–57]. In concert, these aspects may enhance the rate of interfacial charge transfer from a photocatalyst surface to an adsorbate [58,59]. The use of nanostructured g-C_3N_4 is a fast growing area of photocatalysis research, with nanoparticles, nanorods, nanowires, nanotubes, nanospheres, and particularly nanosheets, demonstrating unique features as components of photocatalyst systems [39].

　　2-dimensional g-C_3N_4: 2D-based materials offer an exceptionally high specific surface area, good crystallinity, rich options for host-guest interactions, maximal light absorption, and improved charge-carrier separation over their 3D analogues [60]. Numerous 2D nanomaterials have been reported as heterogeneous catalysts in recent years, with g-C_3N_4 emerging as one of the most promising photocatalysts. Ping and co-workers developed a facile method to prepare g-C_3N_4 nanosheets by direct thermal oxidative 'etching' of bulk g-C_3N_4 under air (Figure 6) [61]. In this method, the hydrogen-bond strands of polymeric melon units which form the interlayers, are gradually removed by oxidation such that the thickness of bulk g-C_3N_4 can be reduced to the desired nanoscale by controlling the etch time, and hence represents a simple, low-cost, and scalable synthesis. The resultant nanosheets exhibit a blue shift of the intrinsic absorption edge in their UV-vis spectra relative to the bulk. The increase in band gap of nanosheets (2.97 eV; Figure 7A) relative to their bulk counterpart (2.77 eV) is further confirmed by a blue shift in the fluorescence emission spectrum of 20 nm (Figure 7B). This widening of the band gap reflects quantum confinement which raises and lowers the conduction and valence band edges respectively [62]. Electronic properties of the nanosheets were determined from the corresponding I−V curve, semiconducting characteristics observed for single g-C_3N_4 nanosheets, suggesting electron transport within the nanosheet plane. In contrast, no current was detected for bulk particle under an applied bias spanning −10–+10 V, evidencing extremely poor electronic conductivity for bulk g-C_3N_4. The lifetime of charge carriers in the nanosheets from time-resolved fluorescence decay spectra also exceeded that of bulk g-C_3N_4.

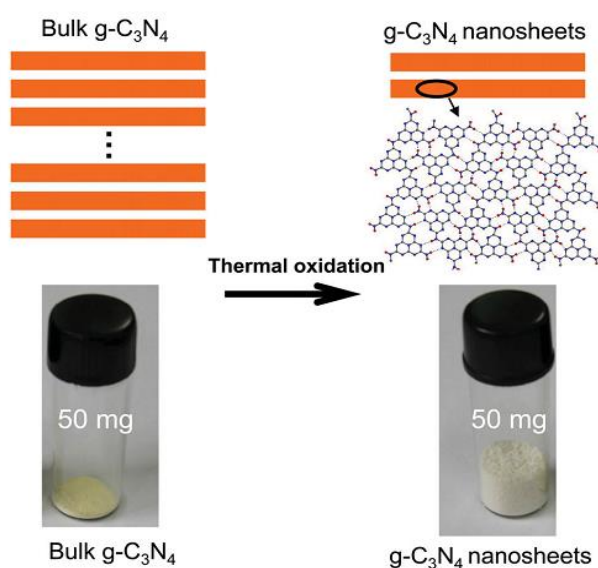**Figure 6.** Thermal exfoliation as a low-cost and green method to prepare ultrathin g-C_3N_4 nanosheets from bulk g-C_3N_4 in water. Reproduced with permission from [61]. Copyright John Wiley & Sons Inc., 2012.

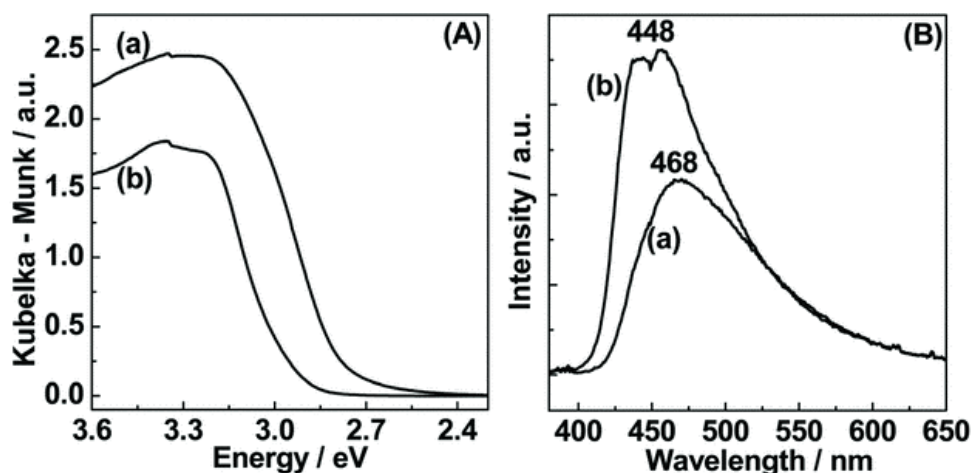**Figure 7.** (**A**) Diffuse reflectance UV-Vis spectra (DRUVS), and (**B**) photoluminescence (PL) spectra of bulk (**a**) and exfoliated nanosheet (**b**) g-C_3N_4. Reproduced with permission from [61]. Copyright John Wiley & Sons Inc., 2012.

Xiaodong and co-workers developed a different liquid exfoliation strategy as a low-cost and green route to ultrathin g-C_3N_4 nanosheets from bulk g-C_3N_4 in water, illustrated in Figure 8 [63]. From a range of solvents, water effectively exfoliated the g-C_3N_4 into ultrathin nanosheets, possibly reflecting its high polarity. The morphology of the exfoliated g-C_3N_4 showed free-standing nanosheets 120 nm across that were almost transparent, and displayed a well-defined Tyndall effect in solution (Figure 8 inset) indicating the presence of monodisperses ultrathin nanosheets. These g-C_3N_4 nanosheets were very stable in acidic and alkaline environments, but exhibited pH-dependent photoluminescence. The g-C_3N_4 nanosheets show superior photoabsorption to the bulk counterpart, resulting in an extremely high PL quantum yield of up to 19.6%. Liquid exfoliation of g-C_3N_4 in isopropanol [64] and methanol [65] resulted in nanosheets with improved photocatalytic performance for the degradation of organic pollutants relative to bulk g-C_3N_4.
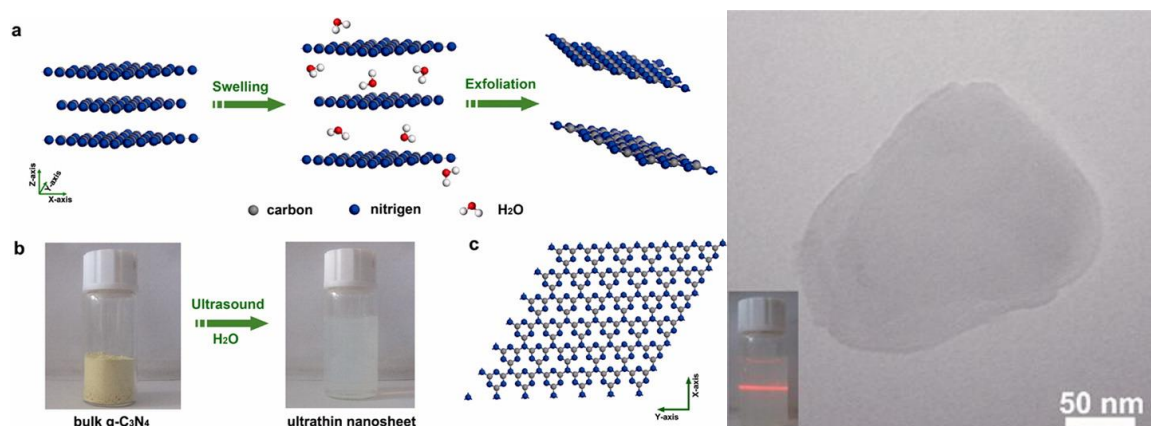
Figure 8. Liquid exfoliation route as a low-cost and green method to prepare the ultrathin g-C_3N_4 nanosheets from bulk g-C_3N_4 in water. Reprinted with permission from [63]. Copyright American Chemical Society, 2013.

1-dimensional g-C_3N_4: In recent years, 1D nanostructures have attracted interest as photocatalysts due to their unique morphology and photophysical properties [66,67], and hence there is interest in preparing 1D g-C_3N_4. 1D g-C_3N_4 nanorods with different aspect ratios were prepared by the reflux of g-C_3N_4 nanoplates as a function of solvent and reflux time [68]. The transformation from g-C_3N_4 nanoplates to nanorods reflects an exfoliation and subsequent re-growth process, which results in 'rolling-up' of individual nanosheets into rods (Figure 9a). The photocatalytic activity of the as-prepared nanorods for methylene blue (MB) degradation in water was explored under visible

light (λ > 420 nm) and simulated solar irradiation (λ > 290 nm). The resulting photocatalytic activity and photocurrent response of g-C_3N_4 nanorods under visible and solar light were about 50–100% greater than the g-C_3N_4 nanoplates.
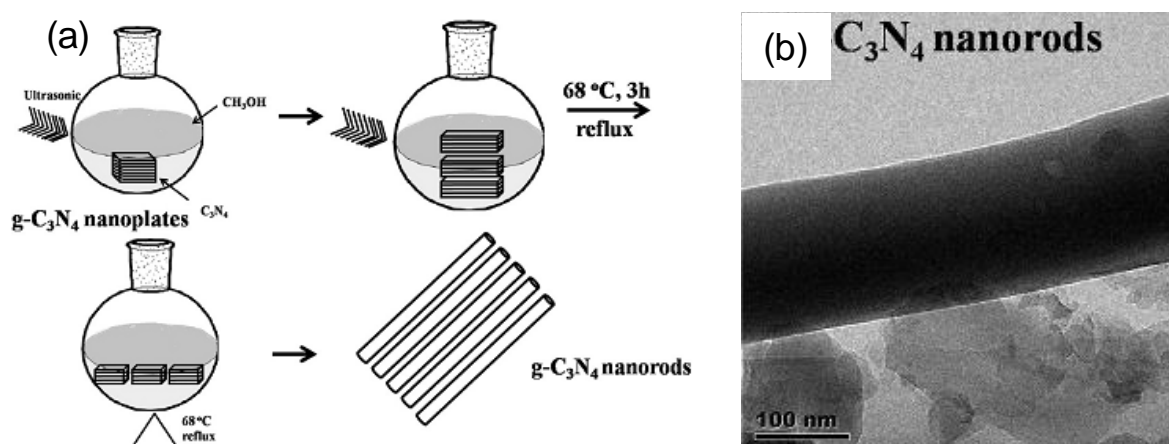

Figure 9. (**a**) Synthesis, and (**b**) Transmission electron microscopy (TEM) images of g-C_3N_4 nanorods. Reprinted with permission from [68]. Copyright American Chemical Society, 2013.

Zhihong and co-workers demonstrated a large-scale synthesis of well-aligned g-C_3N_4 nanorods via the reactive thermolysis of mechanically activated molecular precursors, $C_3N_6H_6$ and $C_3N_3Cl_3$, under heat treatment [69]. These nanorods exhibit peculiar optical properties, evidenced by PL emission and UV-vis absorption. Uniform g-C_3N_4 nanorods were also synthesized via a template of monodispersed, chiral, mesostructured silica nanorods, which were easily prepared via ammonia-catalyzed hydrolysis of tetraethyl orthosilicate with F127 and cetyltrimethylammonium bromide (CTAB) surfactants [70]. The one-dimensional, hexagonal mesostructure of the porous silica nanorods enabled carbon nitride condensation within the pores. The resulting g-C_3N_4 nanorods demonstrated a high photocatalytic activity in hydrogen evolution from water in the presence of triethanolamine and 1 wt % Pt as a co-catalyst compared to that obtained with a conventional g-C_3N_4 [71]. Porous g-C_3N_4 nanorods were also prepared by direct calcination of hydrous melamine nanofibers, precipitated from an aqueous solution of melamine [72]. Porosity provided an enhanced interfacial area for catalysis. Oxygen atoms doped into the g-C_3N_4 matrix altered the band structure, resulting in more effective separation of electron/hole pairs and a corresponding excellent visible light photocatalytic activity for hydrogen evolution in the presence of triethanolamine as a hole quencher. A simple wet-chemical route was also reported for the preparation of nanofiber-like g-C_3N_4 structures with an average diameter of several nm and 100 nm in length [73]. The g-C_3N_4 nanofibers exhibited a high surface area, and low density of crystalline defects, with a slight blue shift of 0.13 eV compared to bulk g-C_3N_4, possibly due to more perfect packing, electronic coupling, and quantum confinement effects. The catalytic activity of g-C_3N_4 nanofibers for Rhodamine B photodegradation was much higher than that of bulk g-C_3N_4, with the nanofibers also exhibiting superior stability. An alternative approach to the synthesis of g-C_3N_4 nanotubes adopted the direct heating of melamine, packed into a compact configuration to favour tubular structures (Figure 10a–d) [74]. This route was advantageous since it required no additional organic templates, facilitating commercial, low-cost and large-scale application. The resulting g-C_3N_4 showed intense fluorescence around 460 nm, and hence has potential application as a blue light fluorescence material. These g-C_3N_4 nanotubes exhibited better visible light photocatalytic activity for MB degradation than either bulk g-C_3N_4 or a p25 TiO_2 reference (the latter is unsurprising since pure titania is a UV band gap material). Muhammad and co-workers also prepared tubular g-C_3N_4 by pre-treating melamine with HNO_3 before thermal processing [75]. The g-C_3N_4 nanotubes were again active for MB and methylene orange (MO) degradation under visible light, and were more stable than bulk g-C_3N_4; the superior activity attributed to the higher surface area (182 $m^2{\cdot}g^{-1}$) of the tubes and improved light absorption

and charge separation/transfer of electron–hole pairs. g-C₃N₄ nanotubes can also be obtained through rolling-up nanosheets via a simple water-induced morphological transformation [76], avoiding the use of organic solvents and hence promoting green chemical principles.
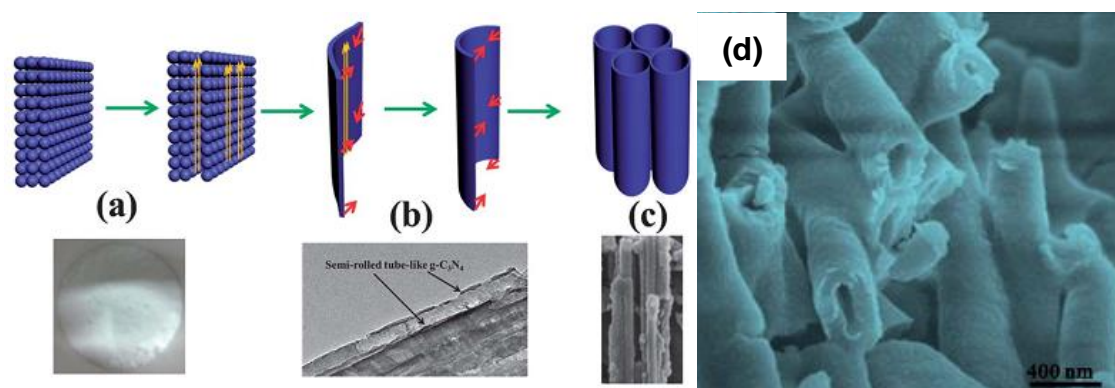

Figure 10. (**a**–**c**) Synthetic strategy, and corresponding (**d**) TEM image of g-C₃N₄ nanotubes. Reproduced with permission from [74]. Copyright Royal Society of Chemistry, 2014.

Ribbon-like g-C₃N₄ nanostructures have been prepared employing dicyandiamide (DCDA) and NaCl crystals as structure-directing agents [77], with a possible mechanism shown in Figure 11. These ribbon-like g-C₃N₄ nanostructures exhibit interesting optical and electronic properties, including a large blue shift in their absorption spectrum corresponding to an increased band gap from 2.7 eV to 3.0 eV. The latter may reflect the incorporation of some Na⁺ ions within the nitride pores, and functionalization by cyano groups. The ribbon-like g-C₃N₄ emits blue light at around 440 nm under 365 nm excitation, whereas bulk g-C₃N₄ exhibited a broad emission spanning 460–520 nm, i.e., yellow-green light. Unfortunately, these ribbon-like g-C₃N₄ nanostructures have not yet been tested for as photocatalysts.
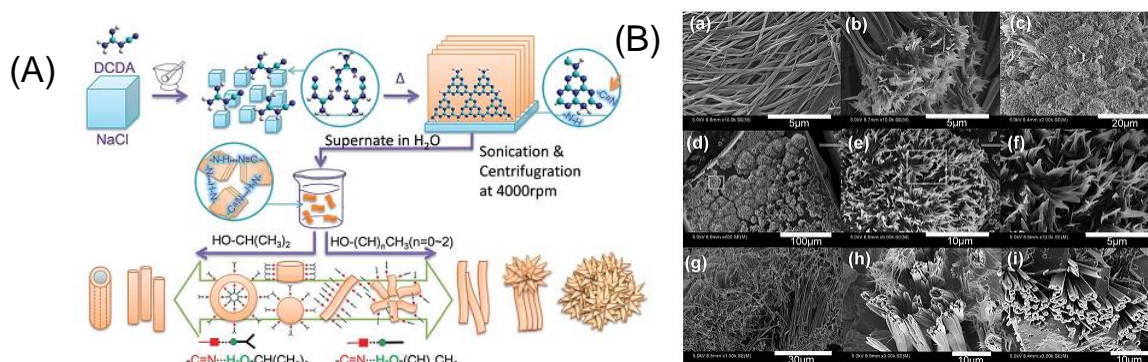
Figure 11. Synthesis strategy (**A**) Ribbon-like g-C₃N₄ nanostructures (**B**) TEM image. Reproduced from with permission from [77]. Copyright Royal Society of Chemistry, 2014.

0-dimensional g-C₃N₄: 0D materials such as quantum dots are of great interest in photocatalysis [78]. g-C₃N₄ quantum dots have been prepared from bulk g-C₃N₄ by thermochemical etching [74]. This tunable multi-step preparation involves thermal exfoliation of 3D bulk g-C₃N₄ into 2D nanosheets, followed by acid etching with concentrated H₂SO₄ and HNO₃ to produce 1D nanoribbons. In this second step, some C–N bonds which connect the tri-s-triazine units are oxidized, resulting in the introduction of oxygenate functional groups, such as carboxylates, at edges and on the basal plane. Cleavage of the nanosheets along preferential orientations yields nanoribbons with diameters <10 nm and several tens of nm in length. In a final step, nanoribbons are converted to 0D quantum dots of 5–9 nm across by hydrothermal treatment (Figure 12) that are highly soluble in water, and stable in solution under ambient conditions for almost eight months. These quantum dots exhibited light 'up-conversion' when excited by long wavelength light, for example, irradiation with

705–862 nm light resulted in 350–600 nm emission, encompassing a large portion of the visible-light spectrum. This up-conversion was proposed to occur via a multiphoton process involving anti-Stokes photoluminescence. The ability of g-C_3N_4 quantum dots to convert NIR to visible light renders them a promising universal energy transfer component in a photocatalytic system, able to harness long wavelength solar energy. This was demonstrated for water splitting, in which quantum dots were added to promote photocatalytic H_2 production by platinized bulk g-C_3N_4 and P25, with dramatic rate-enhancements (up to 52-fold) observed for the latter under visible light irradiation in the presence of a methanol sacrificial hole scavenger. Single layered g-C_3N_4 quantum dots were also prepared by Guoping and co-workers, although in this instance for two-photon fluorescence imaging of cellular nucleus [42]. They again adopted a multi-step synthesis involving acid treatment of bulk g-C_3N_4 to form a porous material and subsequently ultrathin nanosheets, with subsequent ammonia addition, hydrothermal treatment, and ultrasonication of the porous g-C_3N_4 nanosheets liberating aqueous suspensions of g-C_3N_4 quantum dots.
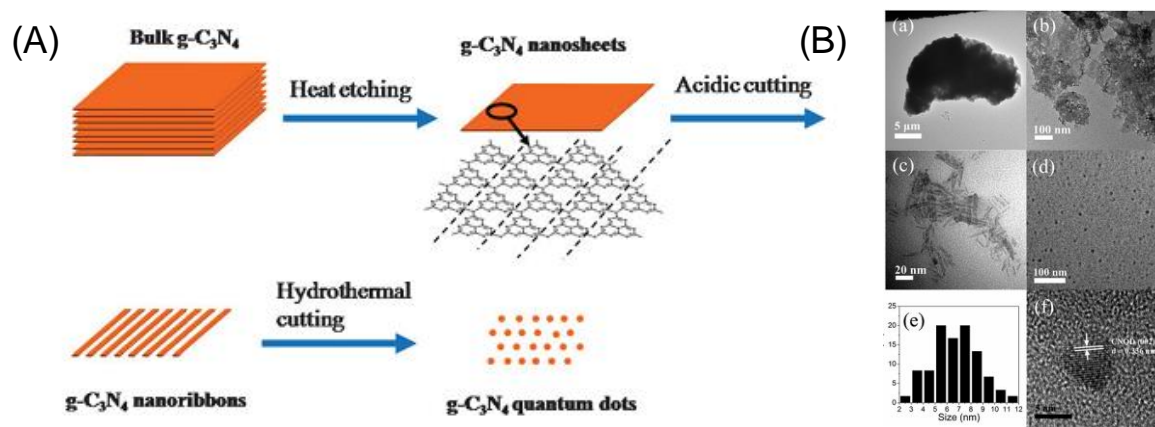

Figure 12. (**A**) Synthesis, and (**B**) TEM images of g-C_3N_4 quantum dots. Reproduced from with permission from [74]. Copyright Royal Society of Chemistry, 2014.

3D-dimensional g-C_3N_4: 3D nanomaterials unlock a vast and complex design space for constructing novel and efficient photocatalytic systems [79], such as hierarchical 3D nanoporous g-C_3N_4 microspheres using a template-free solvothermal synthesis [80]. In this example, a two-step synthesis was adopted: (i) amorphous and nanoporous g-C_3N_4 microspheres were prepared from melamine and cyanuric chloride in acetonitrile; and (ii) subsequently subjected to thermal processing at 550 °C under argon to transform the amorphous microspheres into hierarchical g-C_3N_4 microspheres (Figure 13). Surprisingly, the hierarchical g-C_3N_4 microspheres exhibited a red-shift relative to the bulk counterpart, and uncalcined microspheres, attributed to the high degree of condensation and packing between the layers within the microspheres. The photoluminescence emission intensity of hierarchical g-C_3N_4 microspheres was low compared to bulk and uncalcined g-C_3N_4 microspheres indicating that calcination suppresses radiative charge recombination in the hierarchical structure. These porous g-C_3N_4 microspheres also exhibit a narrowed band gap (2.42 eV), lower electrical resistance and a higher photoresponse than the bulk material, facilitating visible-light harvesting and more efficient transport and separation of photo-induced charge carriers. Hierarchical g-C_3N_4 nanospheres, comprised of nanosheet assemblies, were also prepared by Jinshui and co-workers, but employing high area silica nanospheres as sacrificial templates [81]. The silica template offered efficient cyanamide adsorption, and a framework for the formation of interconnected 2D g-C_3N_4 nanosheets during self-polymerization on heating. The excellent thermal and mechanical stability of silica spheres enabled high temperature construction of the hierarchical g-C_3N_4 nanospheres, and could subsequently be removed through etching by NH_4HF_2 solution, with the hierarchical g-C_3N_4 retaining a spherical morphology. These hierarchal nanospheres are constructed of flat nanosheets emanating from the center (sphere surface) and then interconnecting to form a mesoporous shell (Figure 14), this structure may favour both charge separation and mass transport

in photocatalysis. The nanospheres had a wider band gap than bulk g-C₃N₄, possibly due to quantum size effects, but superior light harvesting across the optical spectrum, especially between 430–590 nm. This may arise from multiple reflections (and hence opportunities for absorption) of incident light within the hierarchical architectures, and/or presence of a high density of defective sites associated with exposure of low-coordination sites at the 'sharp' edges of the constituent nanosheets.
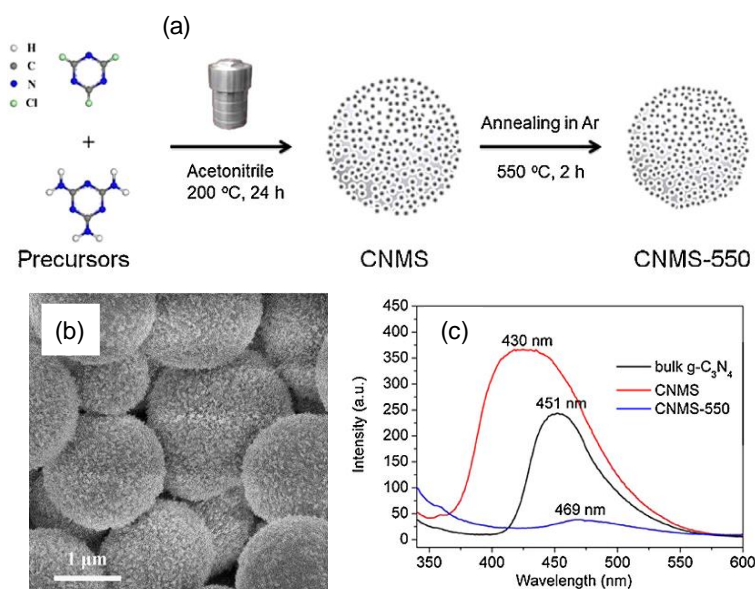
Figure 13. (**a**) Synthetic strategy, (**b**) TEM image, and (**c**) room-temperature photoluminescence spectra of porous g-C₃N₄ microspheres. Reprinted with permission from [80]. Copyright Elsevier, 2015.

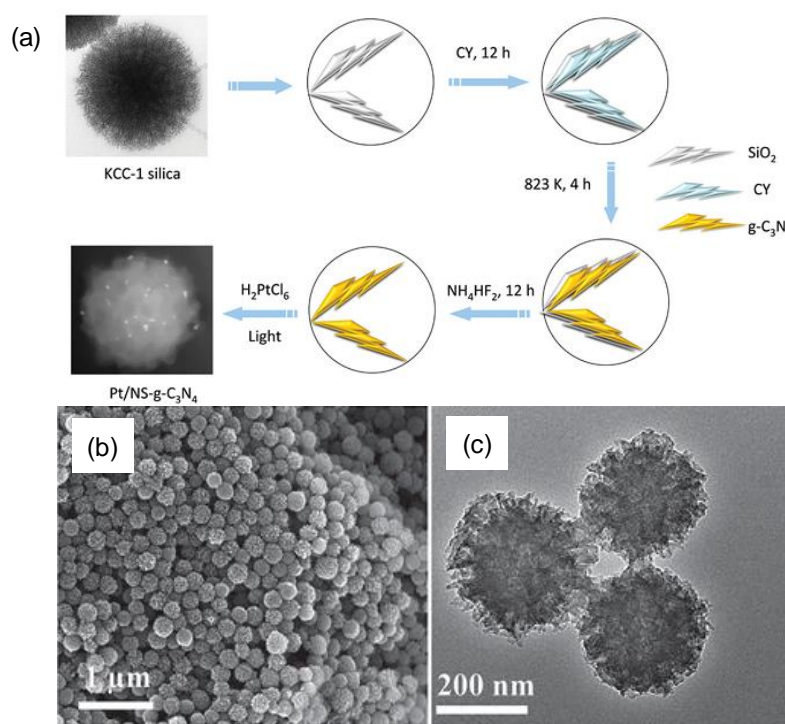**Figure 14.** (**a**) Synthetic strategy, and (**b**,**c**) Scanning electron microscopy and TEM images of hierarchical g-C₃N₄ microspheres. Reproduced with permission from [81]. Copyright John Wiley & Sons Inc., 2014.

Hollow g-C₃N₄: Hollow nanostructures are another promising morphology for energy storage and conversion applications, with significant research efforts devoted to the design and synthesis of hollow nanostructures with high complexity through manipulating their geometry, chemical composition, building blocks, and interior architecture to, e.g., enhance their electrochemical performance [82,83]. Hollow g-C₃N₄ nanospheres have been synthesized using silica nanoparticles as templates [83,84]. Careful control over the shell thickness of such polymeric g-C₃N₄ hollow nanospheres prevents deformation of the core–shell arrangement (Figure 15), even after 400 °C processing. Although a blue shift in the band gap accompanying their synthesis is undesirable, and attributed to either quantum effects or enhanced H-type interlayer packing, further chemical methods, such as extending the pi system by anchoring aromatic motifs, exist to improve visible light absorption, for example, through co-polymerization; such chemical modification and extended p-conjugation can red-shift optical absorption, and improve charge separation in the shell, without damaging the hollow polymeric architectures [85]. This strategy has been adopted to tune the semiconductor properties of the shell in the hollow g-C₃N₄ nanospheres to enhance photocatalytic activity for hydrogen evolution under visible light. A simple, molecular cooperative assembly of low cost triazine molecules into hollow g-C₃N₄ is also reported by Young-Si et al. [86], with this precursor enabling simultaneous optimization of the textural and photophysical properties of g-C₃N₄.
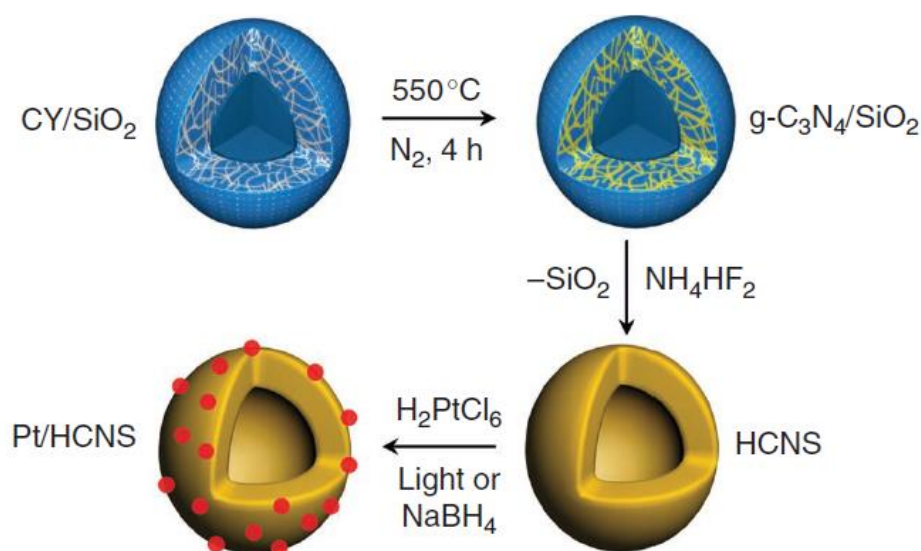
Figure 15. Synthetic strategy for fabricating hollow g-C₃N₄ nanospheres. Reprinted with permission from [84]. Copyright Springer Nature, 2012.

Mesoporous g-C₃N₄: Mesoporous photocatalysts have attracted attention for their (comparatively) high quantum efficiency associated with high surface areas, superior molecular mass transport in-pore [87], and opportunities for enhanced light harvesting through the internal scattering of incident light. An atomically thin mesoporous mesh of g-C₃N₄ nanosheets was recently prepared by solvothermal synthesis (Figure 16) which exhibits outstanding photocatalytic activity for H₂ production [88].
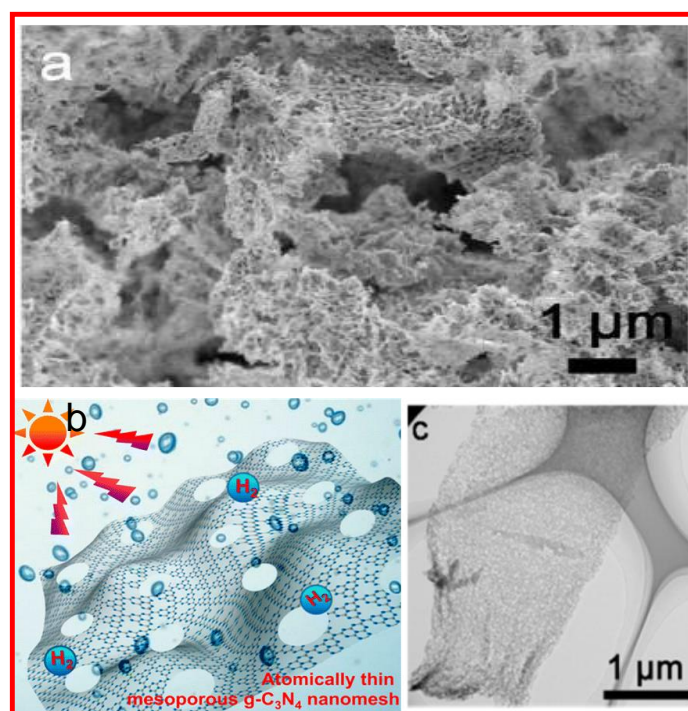
Figure 16. (**a**) SEM images, (**b**) cartoon of photocatalytic H_2 from water splitting, and (**c**) TEM image of atomically thin, mesoporous g-C_3N_4 nanosheets. Reprinted with permission from [88]. Copyright American Chemical Society, 2016.

5. Photocatalytic Applications of g-C_3N_4 Nanostructures

g-C_3N_4 nanostructures have proven excellent catalysts in diverse applications [39,85,89,90] including hydrogen production from water splitting [88,91], CO_2 reduction to fuels and chemicals [92], environmental remediation [39], fuel cells [93], and organic synthesis [89]. Here we focus on photocatalytic applications.

5.1. Solar Fuel Generation

Solar fuels production from CO_2 and water via artificial photosynthesis is one of the promising strategies to deliver H_2, syngas and hydrocarbons as sustainable energy and chemical feedstocks [19]. g-C_3N_4 offers the promise of metal-free and scalable photocatalysts for visible light use.

5.1.1. H_2 Evolution

Hydrogen is one of the most promising alternative energy sources to fossil fuels; however, the large energy barrier to water splitting still presents a challenge to practical photocatalytic systems [35]:

$$2H_2O \text{ (l)} \rightarrow 2H_2 \text{ (g)} + O_2 \text{ (g)}, \Delta G = +474 \text{ kJ/mol}$$
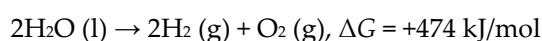
Advanced materials are hence sought that are amenable to harnessing sunlight for either direct photochemical, or photoelectrochemical water splitting. For photocatalytic water splitting, the conduction band (CB) energy must be sufficiently negative (relative to normal hydrogen electrode (NHE)) such that photoexcited electrons are sufficiently energetic to reduce water [94,95]:

$$2H_2O \rightarrow 2H_2 + O_2 \tag{1}$$

$$H_2O \leftrightarrow H^+ + OH^- \tag{2}$$

$$2H_2O + 2e^- \rightarrow H_2 + 2OH^- \tag{3}$$

$$2H_2O \rightarrow O_2 + 4H^+ + 4e^- \tag{4}$$
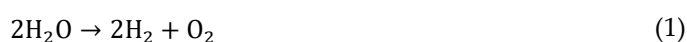
The redox potential for the overall reaction at pH = 7, E_H = −1.23 V (NHE), with the corresponding half-reactions of −0.41 V (Equation (4)) and 0.82 V, giving an overall ΔG^0 = +237 kJ·mol^{-1}.

Most single component photocatalysts exhibit poor activity for visible light-driven H$_2$ production. However, the combination of g-C$_3$N$_4$ with a metal co-catalyst and hole scavenger can afford high visible-light photoactivity. Shubin and co-workers [64] prepared g-C$_3$N$_4$ nanosheets by thermal exfoliation which demonstrated a superior hydrogen production from a water/triethanolamine solution relative to the bulk nitride; nanosheets with a thickness as low as 2 nm were optimal, achieving rate-enhancements of 5.5- and 3-fold under UV-vis and visible light irradiation respectively. Single atomic layer g-C$_3$N$_4$ nanosheets prepared by a chemical exfoliation [96] also display better photogenerated charge transport and separation than bulk g-C$_3$N$_4$, presumably due to the improved H$_2$ evolution. Atomically thin, mesoporous g-C$_3$N$_4$ nanomesh prepared by solvothermal routes exhibits an exceptional photocatalytic activity for H$_2$ evolution [88] of 8510 µmol·h^{-1}·g^{-1} (with an apparent quantum efficiency of 5.1% at 420 nm), far higher than the 1560 µmol·h^{-1}·g^{-1} achieved over non-porous 2D g-C$_3$N$_4$ nanostructures or 350 µmol·h^{-1}·g^{-1} observed for bulk g-C$_3$N$_4$ (apparent quantum efficiency 3.75% at 420 nm); the porous g-C$_3$N$_4$ nanomesh possessed a high surface area and better alignment of conduction and valence band edges. g-C$_3$N$_4$ nanorods also show high photocatalytic activity for hydrogen production from water in the presence of triethanolamine (TEOA) and a 1 wt % Pt co-catalyst [68] wherein the platinum nanoparticles uniformly decorate the g-C$_3$N$_4$ nanorods. Such materials are also superior to mesoporous analogues [70]. TEOA is the most common hole scavenger for g-C$_3$N$_4$ photocatalysts wherein it confers superior activity to methanol (a 14-fold rate enhancement); although the origin of this difference remains poorly understood, Jones and co-workers speculated that the nitrogen lone pair is responsible for the enhanced activity [62]. P25 also exhibited superior activity for photocatalytic hydrogen production when TEOA was employed as a hole scavenger (versus methanol), albeit to a lesser extent than for carbon nitride. g-C$_3$N$_4$ nanotubes synthesized through a rolling-up mechanism by water-induced morphological transformation also display superior visible-light H$_2$ production bulk g-C$_3$N$_4$ or g-C$_3$N$_4$ nanosheets [76]. g-C$_3$N$_4$ quantum dots [77] prepared from bulk g-C$_3$N$_4$ by thermochemical etching were three times more active than bulk g-C$_3$N$_4$ under visible irradiation when promoted by 1 wt % Pt and using 10% triethanolamine as a sacrificial agent, possibly due to up-conversion of NIR to visible light and concomitant increased light harvesting. Tuning of the electronic band structure of g-C$_3$N$_4$ quantum dots [97] to optimize their visible or NIR light response, further enhances photocatalytic H$_2$ evolution. P-doped g-C$_3$N$_4$ nanosheets also exhibit promising visible-light photocatalytic H$_2$ productivity of 1596 mmol·h^{-1}·g^{-1} (apparent quantum efficiency of 3.56% at 420 nm) superior to other metal-free g-C$_3$N$_4$ nanosheet photocatalysts [98]. The excellent photocatalytic activity originates from P-doped macroporous analogues arises from empty mid-gap states (−0.16 V vs. NHE) which extend light harvesting up to 557 nm. Macropores also increased the surface area to 123 m^2·g^{-1}, and shortened the charge-to-surface migration length to only 5–8 nm.

Hierarchically 3D nanoporous g-C$_3$N$_4$ microspheres [80] have also been exploited for water splitting in aqueous solution with 15 triethanolamine and 3 wt % Pt as a co-catalyst under visible light. These g-C$_3$N$_4$ microspheres showed H$_2$ productivity 2.5 times higher than that of bulk g-C$_3$N$_4$, and good stability over five consecutive recycles. Hierarchical g-C$_3$N$_4$ nanospheres [81] comprised of nanosheets with 3 wt % Pt co-catalyst showed significant improvements in H$_2$ production, with an apparent quantum yield of 9.6% at 420 nm, far superior to that for individual g-C$_3$N$_4$ nanosheets of 3.75%. Monodispersed, hollow g-C$_3$N$_4$ nanospheres are also reported to exhibit high photoactivity for water splitting, and a high apparent quantum yield of 7.5% [84]. H$_2$ evolution over these hollow g-C$_3$N$_4$ spheres was significantly enhanced by addition of a MoS$_2$ co-catalyst, with the formation of the MoS$_2$/g-C$_3$N$_4$ heterojunctions (Figure 17) improving light-harvesting, and fast charge separation [99].
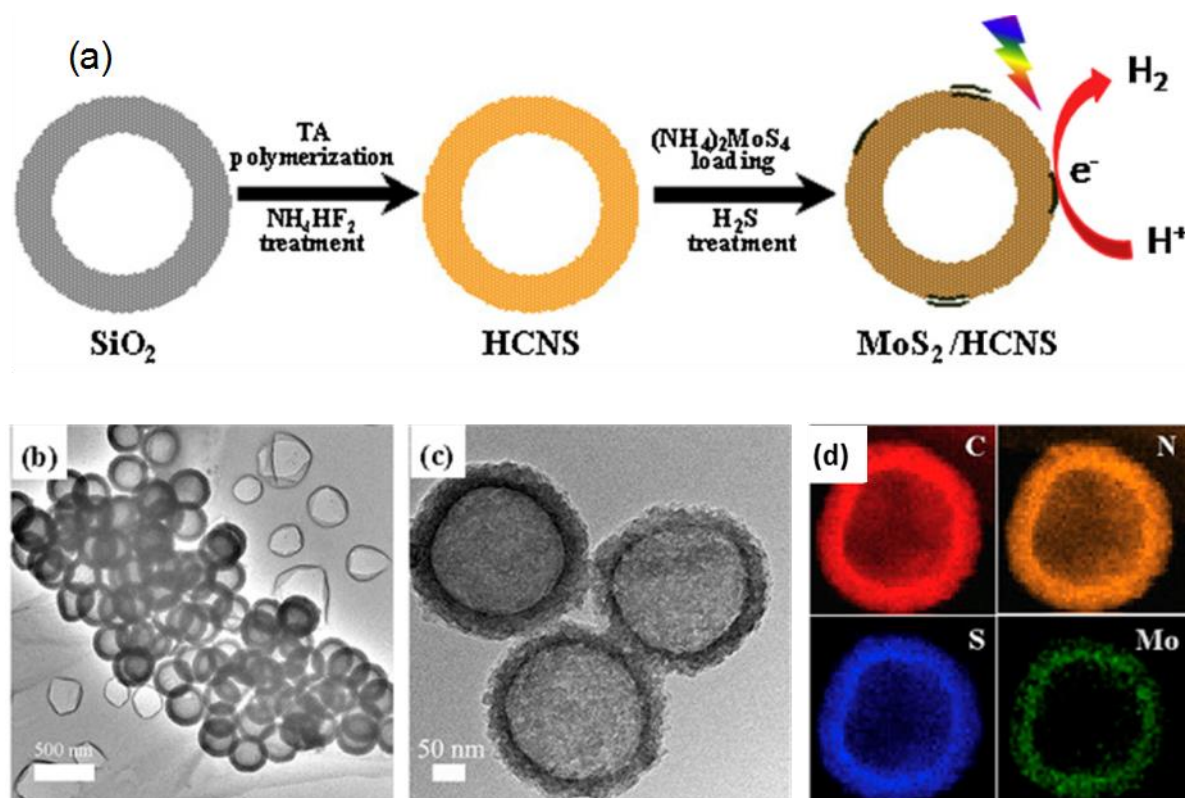
Figure 17. (**a**) Synthetic strategy and (**b**,**c**) TEM images and (**d**) Energy dispersive X-ray spectroscopy (EDX) elemental maps of MoS_2@hollow g-C_3N_4. Reprinted with permission from [99], copyright Elsevier, 2016.

g-C_3N_4 has also been coupled with semiconductors and metal nanoparticles that exhibit visible light surface plasmon resonances to extend their spectral range. Such heterojunction materials offer enhanced separation of photoexcited charge carriers, and hence suppressed recombination and energy loss through fluorescence [39,91]. Noble metal-promoted g-C_3N_4 offers improved UV and visible light harvesting, fast molecular diffusion, and a high density of photoactive sites [100–102]. TiO_2/g-C_3N_4 heterojunctions have been fabricated by a two-step hydrothermal-calcination route from melamine, followed by an in-situ solid-state reaction [103]. The resulting TiO_2/g-C_3N_4 heterostructures possess a narrow band gap and good photoactivity (556 $\mu mol^{-1} \cdot g^{-1}$) for H_2 evolution under visible-light irradiation compared to pure g-C_3N_4 (108 $\mu mol \cdot h^{-1} \cdot g^{-1}$) or TiO_2 (130 $\mu mol \cdot h^{-1} \cdot g^{-1}$. Core@shell heterojunction nanocomposites have additional advantages due to a high interfacial contact area between the shell and core components [104]. For example, CdS@g-C_3N_4 core/shell nanowires [104] with different g-C_3N_4 contents were prepared by a combined solvothermal and chemisorption method (Figure 18) in which g-C_3N_4 uniformly adsorbs over CdS nanowires resulting in enhanced improved photocatalytic H_2 production of 4152 $\mu mol \cdot h^{-1} \cdot g^{-1}$ for 2 wt % g-C_3N_4. A one-step self-assembly route was recently developed to fabricate core–shell architecture comprising carbon spheres decorated by g-C_3N_4. These composites showed extended light absorption and high mechanical stability, with enhanced conductivity for charge transport [105], delivering hydrogen evolution rates of 129 $mol \cdot h^{-1}$, and 8-fold improvement over pristine g-C_3N_4 (16 $mol \cdot h^{-1}$). Other g-C_3N_4 nanocomposites were investigated with a range of materials and morphologies [39,82,91,106–128], to access different charge transfer mechanisms between g-C_3N_4 and the other components. These include a g-C_3N_4-based type II heterojunction [103], g-C_3N_4-based p-n heterojunction [91,129], g-C_3N_4-based Z-scheme heterojunction [113,130], g-C_3N_4/metal heterojunction [100,102], and a g-C_3N_4/carbon heterojunction [131]. The design of g-C_3N_4 heterojunction photocatalysts is an attractive strategy to tune the electronic structure and redox potentials for visible-light absorption photocatalytic H_2 generation. Table 1 compares the performance of different g-C_3N_4 photocatalysts.

Table 1. Photocatalytic H_2 production over $g\text{-}C_3N_4$ nanostructured catalysts.

Entry	Photocatalyst	Co-Catalyst (Loading)	Experimental Details	H_2 Productivity /$\mu mol \cdot g^{-1} \cdot h^{-1}$	Reference Material /$\mu mol \cdot g^{-1} \cdot h^{-1}$	Enhancement Relative to Conventional $g\text{-}C_3N_4$	Apparent Quantum Efficiency/%	Reference
1	$g\text{-}C_3N_4$ nanosheets (thermal exfoliation)	Pt (6 wt %)	10 vol% TEOA 300 W Xe ($\lambda \geq 400$ nm)	170	bulk $g\text{-}C_3N_4$ 31.48	5.4		[61]
2	$g\text{-}C_3N_4$ nanosheets (liquid exfoliation)	Pt (3 wt %)	10 vol% TEOA 300 W Xe ($\lambda \geq 420$ nm)	93 μmol	bulk $g\text{-}C_3N_4$	10		[64]
3	$g\text{-}C_3N_4$ nanosheets (thermal treatment)	Pt (0.5 wt %)	15 vol% TEOA 300 W Xe ($\lambda > 420$ nm)	1400	$g\text{-}C_3N_4$ 450	3	2.6 (420 nm)	[132]
4	$g\text{-}C_3N_4$ nanosheets	Pt (1 wt %)	10 vol% TEOA full sunlight and $\lambda > 400$ nm	1395	bulk $g\text{-}C_3N_4$ 250	5.6		[133]
5	Single layer $g\text{-}C_3N_4$	Pt (3 wt %)	10 vol% TEOA 500 W Xe ($\lambda > 420$ nm)	230	bulk $g\text{-}C_3N_4$ 90	2.5		[96]
6	Urea derived $g\text{-}C_3N_4$	Pt (3 wt %)	~10 vol% TEOA 300 W Xe ($\lambda \geq 395$ nm)	3327.5	DCDA derived $g\text{-}C_3N_4$ thiourea derived $g\text{-}C_3N_4$	7 10	26.5 (400 nm)	[134]
7	Nano Spherical-$g\text{-}C_3N_4$	Pt (3 wt %)	10 wt % TEOA 300 W Xe ($\lambda > 420$ nm)	14,350	Pt/bulk $g\text{-}C_3N_4$ 318	45	9.6 (420 nm)	[81]
8	$g\text{-}C_3N_4$ nanostructure	Pt (3 wt %)	15 wt % TEOA 300 W Xe ($\lambda > 420$ nm)	689	bulk $g\text{-}C_3N_4$ 8	8.6		[135]
9	Porous $g\text{-}C_3N_4$ microspheres	Pt (3 wt %)	15 wt % TEOA 300 W Xe ($\lambda > 420$ nm)	180	bulk $g\text{-}C_3N_4$ 7.8	2.3	1.62 (420 nm)	[80]
10	Silica templated mesoporous $g\text{-}C_3N_4$	Pt (3 wt %)	10 vol% TEOA $\lambda > 420$ nm	237.4 (μmol^{-1} m^{-2})	$g\text{-}C_3N_4$ 9.16 ($\mu mol \cdot h^{-1} \cdot m^{-2}$)	25.8		[136]
11	macroscopic 3D porous $g\text{-}C_3N_4$ monolith	Pt (3 wt %)	10 vol% TEOA 300 W Xe ($\lambda > 420$ nm)	29	$g\text{-}C_3N_4$ 10.2	2.8		[137]
12	hollow $g\text{-}C_3N_4$ nanospheres	Pt (3 wt %)	10 wt % TEOA 300 W Xe	15,000	pure $g\text{-}C_3N_4$ 5000	3		[85]
13	Iodine doped-$g\text{-}C_3N_4$	Pt (3 wt %)	10 vol% TEOA 300 W Xe ($\lambda \geq 420$ nm)	890	bulk $g\text{-}C_3N_4$ 98.8	9		[138]
14	P doped-$g\text{-}C_3N_4$	Pt (3 wt %)	10 wt % TEOA 300 W Xe	2082	pure $g\text{-}C_3N_4$ 226.3	9.2		[139]
15	O-doping supramolecular porous $g\text{-}C_3N_4$	Pt (3 wt %)	10 vol% TEOA 300 W Xe ($\lambda \geq 420$ nm)	1204	bulk $g\text{-}C_3N_4$ 3D porous $g\text{-}C_3N_4$	6.1 3.1	7.8 (420 nm)	[140]

16	K-g-C_3N_4	Pt (0.5 wt %)	10 vol% TEOA 300 W Xe (λ > 400 nm)	1028	pure g-C_3N_4 73.4	14		[141]
17	AuPd/g-C_3N_4	Au and Pd	10 vol% TEOA 300 W Xe ($\lambda \geq$ 400 nm)	326	Au/g-C_3N_4 Pd/g-C_3N_4	3.5 1.6		[142]
18	Hydrogenated g-C_3N_4	Pt (3 wt %)	10 vol% TEOA 350 W mercury arc lamp (λ > 420 nm)	900	bulk g-C_3N_4 132.3	6.8		[143]
19	Surface alkalization of g-C_3N_4	Pt (1 wt %)	20 vol% aq. methanol 300 W Xe	2230	urea derived g-C_3N_4 159.3	14	6.67 (400 nm)	[144]
20	dye sensitized g-C_3N_4 nanosheets	Pt	5 vol% TEOA 300 W Xe (λ > 420 nm)	6525	Pt/g-C_3N_4 466	14	33.4 (460 nm)	[145]
21	2-Aminobenzonitrile-mp-g-C_3N_4	Pt (3 wt %)	10 vol% TEOA 300 W Xe ($\lambda \geq$ 420 nm)	229	mp-g-C_3N_4 127	1.8		[146]
22	PPy-g-C_3N_4	Pt (3 wt %)	No sacrificial reagent 350 W Xe (λ > 400 nm)	154	Pt-g-C_3N_4	49.3		[147]
23	Cu_2O@g-C_3N_4 core@shell		10 vol% TEOA 300 W Xe	202.28	Cu_2O 35.08	5.7		[148]
24	CdS/g-C_3N_4 core/shell	Pt (0.6 wt %)	0.35 M Na_2S and 0.25 M Na_2SO_3 300 W Xe ($\lambda \geq$ 420 nm)	4152	pure CdS 2001	2.1	4.3 (420 nm)	[104]
25	Core–shell Ni/NiO-decorated g-C_3N_4	Ni/NiO	10 vol% TEOA 300 W Xe	10	pure g-C_3N_4 1.01	10		[149]
26	MoS_2/g-C_3N_4	N/A	10 vol% TEOA 300 W Xe (λ > 400 nm)	252	pure g-C_3N_4 31.5	8		[150]
27	CdS QD/g-C_3N_4	Pt (0.5 wt %)	0.1 M L-ascorbic acid (pH = 4) 300 W Xe (λ > 420 nm)	4494	pure g-C_3N_4 299	15		[151]
28	CdS nanorods/g-C_3N_4	NiS	10 vol% triethanolamine 300 W Xe ($\lambda \geq$ 420 nm)	2563	pure g-C_3N_4 1582	1.6		[152]
29	$CaIn_2S_4$/g-C_3N_4	Pt (1 wt %)	0.5 M Na_2S and 0.5 M Na_2SO_3 300 W Xe	102	$CaIn_2S_4$ 34	3		[153]
30	$BiPO_4$/P-g-C_3N_4	N/A	Na_2S (0.1 M) 300 W Xe ($\lambda \geq$ 420 nm)	1110	P-g-C_3N_4 676	1.6		[154]
31	AgQCs/g-C_3N_4	Pt (1 wt %)	25 vol% methanol simulator AM 1.5 G	5.59	pure g-C_3N_4 3.29	1.7		[155]
32	Al_2O_3/g-C_3N_4	Pt (1 wt %)	25 vol% TEOA 300 W Xe ($\lambda \geq$ 420 nm)	52.10	pure g-C_3N_4 20.75	2.5		[156]
33	MoS_2/mp-g-C_3N_4	Pt	10 vol% lactic acid	1030	Pt/mp-g-C_3N_4	4.3	2.7	[157]

			300 W Xe ($\lambda \geq$ 420 nm)		239.5	(420 nm)	
34	carbon black/g-C$_3$N$_4$	Pt (3 wt %)	25 vol% methanol $\lambda >$ 420 nm	689	pure g-C$_3$N$_4$ 215	3.2	[158]
35	graphene/g-C$_3$N$_4$	Pt (1.5 wt %)	25 vol% methanol 350 W Xe ($\lambda >$ 400 nm)	451	g-C$_3$N$_4$ 150	3	[107]
36	carbon black/NiS/g-C$_3$N$_4$	NiS	15 vol% TEOA 300 W Xe ($\lambda \geq$ 420 nm)	992	g-C$_3$N$_4$/NiS 396	2.5	[159]
37	N,S-TiO$_2$/g-C$_3$N$_4$	N/A	10 vol% methanol 125 W Hg lamp	317	g-C$_3$N$_4$ 125	2.5	[160]
38	N-CeO$_x$/g-C$_3$N$_4$	Pt (1 wt %)	10 vol% TEOA 300 W Xe ($\lambda \geq$ 420 nm)	292.5	g-C$_3$N$_4$ 134.5	2	[161]
39	g-C3N4 (2D)/CdS (1D)/rGO (2D)	Pt (1 wt %)	10 vol% TEOA 300 W Xe ($\lambda \geq$ 420 nm)	4800	pure g-C$_3$N$_4$ g-C$_3$N$_4$/rGO g-C$_3$N$_4$/CdS	44 11 2.5	[122]
40	Au/(P3HT)/Pt/g-C$_3$N$_4$	Au and Pt	10 vol% TEOA 300 W Xe ($\lambda >$ 420 nm)	320	g-C$_3$N$_4$/Au; 73 and g-C$_3$N$_4$/Pt; 82	4	[162]
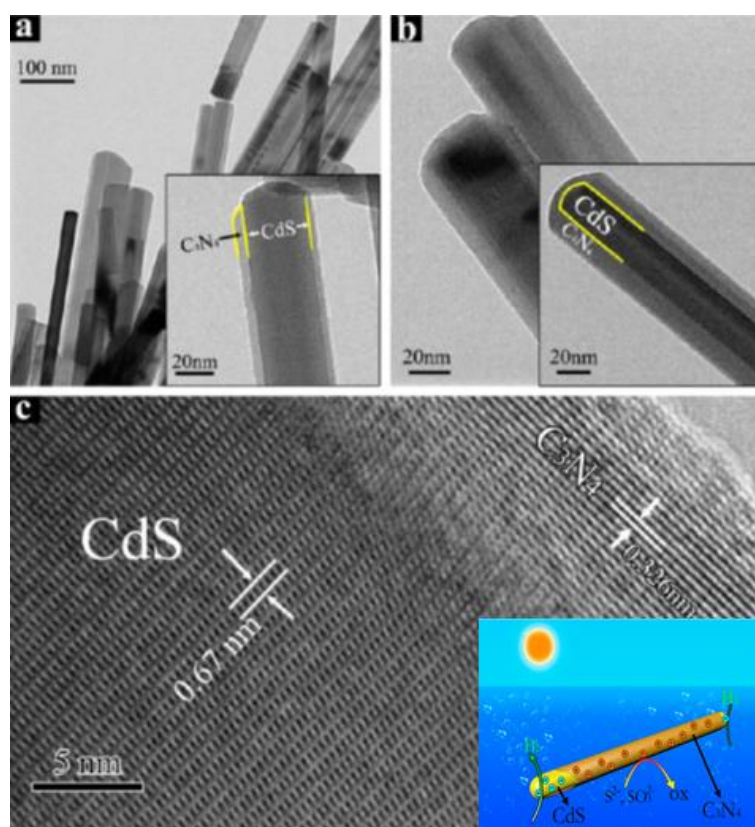
Figure 18. (**a**,**b**) TEM and (**c**) HR TEM image of core–shell CdS@g-C$_3$N$_4$ heterojunction nanocomposite. Reprinted with permission from [104]. Copyright 2013 American Chemical Society.

5.1.2. CO$_2$ Reduction

Rising atmospheric levels of carbon dioxide and the depletion of fossil fuel reserves raise serious concerns about the continued reliance on the use of fossil fuels for both energy and chemicals production [3,163], to which the photocatalytic reduction of CO$_2$ to light oxygenates and hydrocarbons could provide a sustainable solution. CO$_2$ reduction involves multi-electron transfer and hence the reaction kinetics for, e.g., formic acid, carbon monoxide, formaldehyde, methanol and methane production are intrinsically slower than for H$_2$ production. CO$_2$ photoreduction begins with molecular adsorption at the catalyst surface, wherein the anion radical is generated by the transfer of electrons photoexcited across the semiconductor band gap following light absorption. In the case of aqueous phase CO$_2$ reduction, charge-compensation occurs through concomitant water splitting and the transfer of photoexcited holes in the valence band onto hydrogen atoms, with the resulting protons migrating to the CO$_2$ anion. The reduction potentials for CO$_2$ photoreduction with water to various products are described below (relative to NHE at pH = 7) [11,164]:

$$CO_2 + e^- \rightarrow CO_2^{\bullet-} \quad E^0 = -1.90 \text{ eV} \tag{5}$$

$$CO_2 + H^+ + 2e^- \rightarrow HCO_2^{\bullet-} \quad E^0 = -0.49 \text{ eV} \tag{6}$$

$$CO_2 + 2H^+ + 2e^- \rightarrow CO + H_2O \quad E^0 = -0.53 \text{ eV} \tag{7}$$

$$CO_2 + 4H^+ + 4e^- \rightarrow HCHO + H_2O \quad E^0 = -0.48 \text{ eV} \tag{8}$$

$$CO_2 + 6H^+ + 6e^- \rightarrow CH_3OH + H_2O \quad E^0 = -0.38 \text{ eV} \tag{9}$$

$$CO_2 + 8H^+ + 8e^- \rightarrow CH_4 + 2H_2O \quad E^0 = -0.24 \text{ eV} \tag{10}$$

$$CO_2 + 10H^+ + 10e^- \rightarrow C_2H_4 + 4H_2O \; E^0 = -0.22 \text{ eV} \tag{11}$$

$$CO_2 + 12H^+ + 12e^- \rightarrow C_2H_5OH + 3H_2O \; E^0 = -0.33 \text{ eV} \tag{12}$$
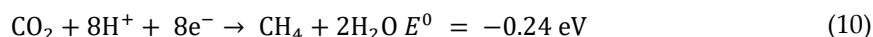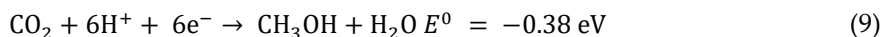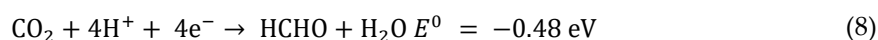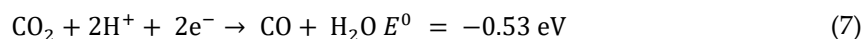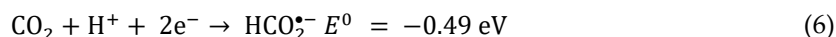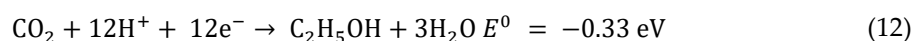
Key factors influencing CO_2 photocatalytic reduction include band energy matching, efficient charge-carrier separation, kinetic of e- and hole transfer to CO_2 and the reductant, and the basicity of the photocatalyst and hence strength and coverage of CO_2 adsorption [164]. In recent years, the g-C_3N_4 nanostructured materials have been studied for CO_2 photoreduction [92,165], due to their excellent stability, sufficiently negative CB energy and narrow band gap. Many strategies are reported to promote g-C_3N_4 with condensed matter and molecular sensitizers [166,167], such as doping with metals [168,169] and non-metal [170–172], heterojunction construction [173–176] and Z-scheme composites employing co-catalysts [165–167,173,175]. Pengfei et al. reported ultrathin C_3N_4 nanosheets for enhanced photocatalytic CO_2 reduction [177] in which surface functionalization and textural modification by NH_3-mediated thermal exfoliation enhanced light harvesting, charge-carrier redox potentials, and the surface area for CO_2 adsorption (to 0.2 mmol·g^{-1}), resulting in CH_4 and CH_3OH productivities of 1.39 and 1.87 µmol·h^{-1}·g^{-1} respectively, a five-fold increase over bulk g-C_3N_4. Jiaguo and co-workers [168] demonstrated that Pt promotion significantly influenced both the activity and selectivity of g-C_3N_4 for CO_2 photoreduction to CH_4, CH_3OH, and HCHO; Pt nanoparticles improved charge separation across the metal/semiconductor interface, and lowered the overpotential for CO_2 reduction. Qingqing et al. reported Pd nanoicosahedrons with twin defects promoted CO_2 reduction into CO and CH_4 over C_3N_4 nanosheets [126]. CO_2 conversion reached 61.4%, with an average CO productivity of 4.3 µmol·g^{-1}·h^{-1} and average CH_4 productivity of 0.45 µmol·g^{-1}·h^{-1}, indicating the presence of highly reactive sites for CO_2 adsorption and activation.

Hierarchical, porous O-doped g-C_3N_4 nanotubes prepared via successive thermal oxidation exfoliation and condensation of bulk g-C_3N_4 also show promise for photocatalytic CO_2 reduction under visible light [171]. As-prepared O-doped g-C_3N_4 nanotubes comprise interconnected, multi-walled nanotubes with uniform diameters of 20–30 nm, which evolve methanol at 0.88 µmol·g^{-1}·h^{-1}, five times faster than bulk g-C_3N_4 (0.17 µmol·g^{-1}·h^{-1}). Heterojunction composites of g-C_3N_4/ZnO synthesized by a one-step calcination route [165] are also superior to bulk g-C_3N_4 (2.5-fold enhancement), ascribed to a direct Z-scheme mechanism reflecting efficient ZnO → g-C_3N_4 electron transfer occurring the interface. Zhongxing et al. reported that CeO_2-modified C_3N_4 photocatalysts produced by a simple hydrothermal route were effective for the selective photocatalytic reduction of CO_2 to CH_4 [178], with a CH_4 productivity of 4.79 mmol·g^{-1}·h^{-1}, about 3.44 times that of g-C_3N_4. Wang et al. prepared a 2D-2D MnO_2/g-C_3N_4 heterojunction photocatalyst by an in-situ redox reaction between $KMnO_4$ and $MnSO_4$ adsorbed at the surface of g-C_3N_4 [179] for photocatalytic CO_2 reduction to CO (9.6 mmol·g^{-1}), in which band matching facilitated efficient separation of photogenerated charge-carriers. Photocatalytic CO_2 reduction reaction is also reported over a direct Z-scheme g-C_3N_4/SnS_2 catalyst [180] which yielded both CH_3OH (2.3 µmol·g^{-1}) and CH_4 (0.64 µmol·g^{-1}), with electrons in SnS_2 combining with holes in g-C_3N_4. Another Z-scheme mechanism is invoked for a MoO_3/g-C_3N_4 composite [181]. Ryo and co-workers adopted a different approach, attaching Ru(bipy)complexes to g-C_3N_4 nanostructures; these displayed improved activity for CO_2 photoreduction to formic acid, with a high apparent quantum yield of 5.7% at 400 nm under visible light (Figure 19). Anchoring of polyoxometalate clusters to C_3N_4 also creates active photocatalysts for CO_2 reduction [179]. Here, noble-metal-free Co_4 polyoxometallates were used to achieve a staggered band alignment, with the Co_4@g-C_3N_4 hybrid photocatalysts achieving 107 µmol·g^{-1}·h^{-1} and 94% selectivity for CO production under visible light ($\lambda \geq 420$ nm); cumulative CO production reached 896·µmol·g^{-1} after 10 h irradiation, far exceeding that for unpromoted g-C_3N_4.
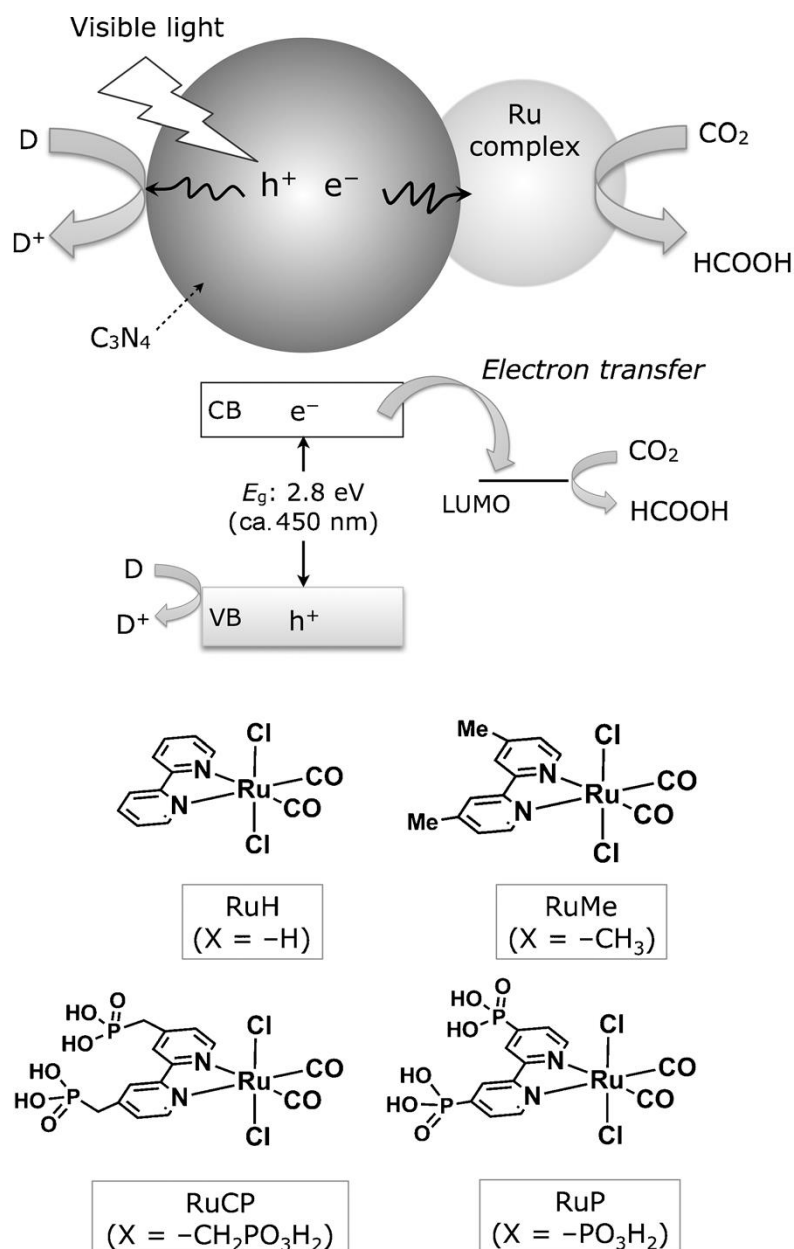
Figure 19. CO_2 reduction using a Ru complex/C_3N_4 hybrid photocatalyst, and structures of the Ru complexes. CB = conduction band, VB = valence band. Reproduced with permission from [166]. Copyright John Wiley & Sons Inc., 2015.

A multicomponent heterostructure, termed an intercorrelated superhybrid, comprising AgBr supported on g-C_3N_4 decorated in turn on N-doped graphene (prepared by wet-chemical synthesis) has also shown excellent activity for the photocatalytic reduction of CO_2 to methanol and ethanol (Figure 20) [174]. Oluwatobi et al. reported g-C_3N_4/(Cu/TiO_2) [182] nanocomposites prepared by pyrolysis and impregnation for enhanced photoreduction of CO_2 to CH_3OH and HCOOH under UV-vis irradiation wherein maximum productivities of CH_3OH and HCOOH under visible light were 2574 and 5069 mmol·g^{-1} respectively. Enhanced photoactivity was attributed to the location of the metal within the composite and consequent distribution of photoexcited electrons. Hailong et al. also studied g-C_3N_4/Ag-TiO_2 hybrid photocatalysts [183], wherein CO and CH_4 were preferentially formed, with a maximum CO_2 conversion of 47 μmol·g^{-1}, and product yields of 28 μmol·g^{-1} CH_4 formation and 19 μmol·g^{-1} CO. Enhanced activity was proposed to arise from the transfer of photoexcited electrons across the g-C_3N_4/TiO_2 heterojunction, and subsequently from $TiO_2 \rightarrow$ Ag nanoparticles due to the lower Fermi level; this spatial separation of charge greatly suppressed the

electron–hole recombination, with electrons accumulating on the Ag nanoparticles on the TiO_2 surface.

Figure 20. (**a**) Synthetic strategy, and (**b**,**c**) photocatalytic performance for CO_2 reduction of intercorrelated superhybrid g-C_3N_4 nanocomposites under visible light and corresponding apparent quantum efficiencies. Reproduced with permission from [174]. Copyright John Wiley & Sons Inc., 2015.

Table 2 compares the performance of different g-C_3N_4 photocatalysts for photocatalytic CO_2 reduction.
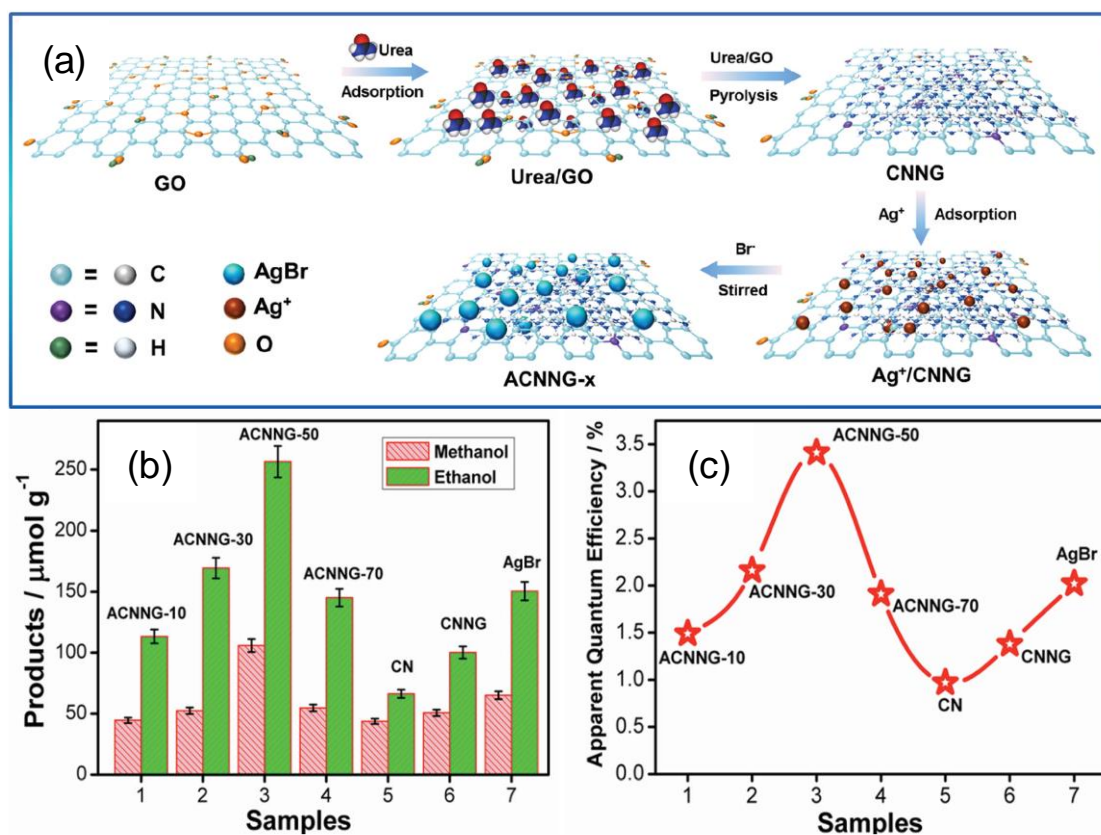
Table 2. Photocatalytic CO_2 reduction over g-C_3N_4 nanostructured catalysts.

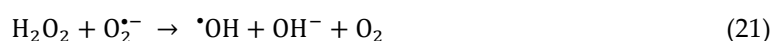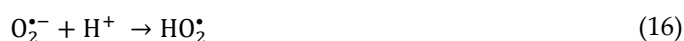| Entry	Photocatalyst	Experimental Details	Productivity /$\mu mol \cdot g^{-1} \cdot h^{-1}$	Reference Material /$\mu mol \cdot g^{-1} \cdot h^{-1}$	Enhancement Relative to Conventional g-C_3N_4	Apparent Quantum Efficiency/%	Reference
1	g-C_3N_4 nanosheets	300 W Xe ($l > 420$ nm), 15 °C and 25 kPa CO_2, catalyst in 80 mL of H_2O	CH_4: 0.94	Bulk g-C_3N_4: 0.30	3.1		[184]
2	g-C_3N_4 nanosheets	300 W Xe (400 nm), 200 mW/cm². 20 mg catalyst in 0.1 mL H_2O, CO_2 bubbled to 0.06 MPa	CH_4: 1.2 CH_3OH: 0.2	Bulk g-C_3N_4 CH_4: 0.28 CH_3OH: 0.24	CH_4: 4.3		[185]
3	Ultrathin g-C_3N_4 nanosheets	300 W Xe, 100 mg catalyst, 0.084 g $NaHCO_3$ + H_2SO_4 to release CO_2	CH_4: 1.39 and CH_3OH: 1.87	Bulk g-C_3N_4 CH_4: 0.14 and CH_3OH: 0.35	CH_3OH: 5.34		[177]
4	Thiourea and urea derived g-C_3N_4	300 W Xe/420 nm, 40 mg catalyst	Urea derived g-C_3N_4 CO: 0.56, CH_3CHO: 0.44, CH_4: 0.04 thiourea derived g-C_3N_4 CO: 0.36, CH_3CHO: 0.26, CH_4 = 0.025	N/A	N/A		[186]
5	Melamine and urea derived g-C_3N_4	300 W Xe (420 nm), 0.2 g and 1.0 M NaOH solution (100 mL)	Urea derived g-C_3N_4 CH_3OH: 6.28, C_2H_5OH: 4.51, O_2: 21.33 melamine derived g-C_3N_4 CH_3OH: TRACE, C_2H_5OH: 3.64, O_2: 10.29	N/A	N/A	Urea derived g-C_3N_4: 0.18, melamine derived g-C_3N_4: 0.08	[172]
6	Thiourea, urea and DCDA derived g-C_3N_4	300–795 nm KG1 filter, 40 mW cm² illumination, 0.5 mg catalyst per mL in CH_3CN/TEOA/H_2O (3:1:1), $t = 2$ h, $[Co(bpy)_n]^{2+}$ as a co-catalyst	Urea derived g-C_3N_4 CO: 460, H_2: 138 μmol thiourea derived g-C_3N_4 CO: 22, H_2: 86 μmol DCDA derived g-C_3N_4 CO: 92, H_2: 94 μmol	N/A	N/A		[167]
7	Sulfur-doped g-C_3N_4	300 W simulated solar Xe and 200 mL Pyrex reactor, 100 mg 1 wt % Pt co-catalyst, 0.12 g $NaHCO_3$ and 0.25 mL 4 M HCl solution	CH_3OH: 0.37	Bulk g-C_3N_4 CH_3OH: 0.27	1.37		[170]
8	Pd/g-C_3N_4	300 W Xe/UV420 cut-off filter	CO: 0.5, CH_4: 0.05, CH_3OH: 1 $\mu mol \cdot g^{-1}$	Bulk g-C_3N_4 CO: 4, CH_4: 0.15, CH_3OH: 2.5 $\mu mol \cdot g^{-1}$			[187]
9	Pt-loaded g-C_3N_4	15 W energy-saving daylight bulb, flow rate of CO_2 fixed at 5 mL·min^{-1}	CH_4: 1.3	Bulk g-C_3N_4 CH_4: 0.25	5.2		[188]

10	Pt-g-C_3N_4	200 mL Pyrex reactor, 300 W simulated solar Xe, 100 mg catalyst, $NaHCO_3$ (0.12 g) and HCl aq. solution (0.25 mL, 4 M)	CH_4: 0.25, CH_3OH: 0.25, HCHO: 0.125	Bulk g-C_3N_4 CH_4: 0.07, CH_3OH: 0.11, HCHO: 0.06	CH_4: 3.57		[168]
11	Amine-functionalized g-C_3N_4	300 W Xe, Pyrex 200 mL, 100 mg catalyst, 0.084 g $NaHCO_3$ + 0.3 mL of 2 M H_2SO_4	CH_4: 0.34 CH_3OH: 0.28	Bulk g-C_3N_4 CH_3OH: 0.26 CH_4: trace	CH_4: 1.3		[189]
12	SnO_2-coupled B and P co-doped g-C_3N_4	300 W Xe (420 nm), 0.2 g catalyst in 3 mL water/100 mL NaOH purged with CO_2	CH_4: 30	Bulk g-C_3N_4 CH_4: 3.5	8.57	2.02 (420 nm)	[190]
13	g-C_3N_4-Ru complex	400 W Hg lamp (400 nm) 11 mL reactor containing 4 mL 20 vol% TEA in acetonitrile and 8 mg catalyst purged with CO_2	HCOOH: 4.6	Bulk g-C_3N_4 HCOOH: trace	N/A		[191]
14	Ag_3PO_4/g-C_3N_4	500 W Xe/420 nm, stainless-steel reactor 132 mL, 10 mg in 4 mL H_2O, 0.4 MPa CO_2 at 80 °C	CO: 44, CH_3OH: 9, CH_4: 0.2, C_2H_5OH: 0.1	Bulk g-C_3N_4 CO: 4, CH_3OH: 0.35, CH_4: 0.09, C_2H_5OH: 0.01	CO: 11		[175]
15	AgX/g-C_3N_4 (X = Cl and Br)	15 W energy-saving daylight lamp, 100 mg catalyst, CO_2 flow of 5 mL/min	CH_4: 1.282	Bulk g-C_3N_4 CH_4: 0.388	3.3		[192]
16	B4C/g-C_3N_4	300 W Xe (UV/IR filter), 100 mL photoreactor, 6 mg catalyst, CO_2	CH4: 0.84	Bulk g-C_3N_4 CH4: 0.14	6		[193]
17	BiOI/g-C_3N_4	300 W Xe (400 nm), 0.10 g catalyst, CO_2 bubbled through water.	CO: 3.58, O_2: 1.96, H_2: 0.4, CH_4: 0.2	Bulk g-C_3N_4 CO: 0.2, O_2: 0.56, H_2: 0.92	CO: 17.9		[194]
18	g-C_3N_4/C	500 W Xe lamp, 0.1 g catalyst, CO_2 + H_2O mixture flow 20 mL min⁻¹, 30 °C and 110 KPa CO_2	CO: 2.5 CH_4: 1.4	Bulk g-C_3N_4 CO: 1.1 CH_4: 0.72	CO: 2.27		[195]
19	CeO_2/g-C_3N_4	300 W Xe, reactor volume 500 mL, 50 mg catalyst, CO_2 bubbled through water	2 wt % CO: 11.8 and CH_4: 9.08 3 wt % CO: 10.16 and CH_4: 13.88	Bulk g-C_3N_4 CO: 6.78 CH_4: 0.2	CH_4: 69.4		[196]
20	Graphene/g-C_3N_4	15 W energy saving daylight bulb, CO_2 5 mL min⁻¹	CH_4: 0.59 μmol·h⁻¹	Bulk g-C_3N_4 CH_4: 0.25 μmol·h⁻¹	2.36		[197]
21	g-C_3N_4/$NaNbO_3$	300 W Xe, reaction volume 230 mL, 50 mg catalyst, reactor purged with CO_2, then 2 mL H_2O injected	CH_4: 6.4	Bulk g-C_3N_4 CH_4: 0.8	8		[173]
22	g-C_3N_4/N-TiO_2	300 W Xe lamp, reaction system vol 780 mL, 0.1 g catalyst, flow rate of CO_2 15 mL min⁻¹	CO: 14.73 μmol	Bulk g-C_3N_4 CO: 4.20 μmol; P25: 3.19 μmol	3.5		[198]

23	rGO/g-C$_3$N$_4$	15 W energy-saving daylight lamp, CO$_2$ at a flow rate of 5 mL/min, 100 mg catalyst	CH$_4$: 14	Bulk g-C$_3$N$_4$ CH$_4$: 2.5	5.6	0.56 (420 nm)	[199]
24	g-C$_3$N$_4$ and a Ru(II) complex	400 W high-pressure Hg lamp, 8 mg catalyst, DMA (containing 20 vol% TEOA) 4.0 mL	CO: 2.9 μmol·h^{-1}, HCOOH: 1.5 μmol·h^{-1}; H$_2$: 0.13 μmol·h^{-1}	Bulk g-C$_3$N$_4$ Only trace	N/A		[200]
25	Ru complex/mp g-C$_3$N$_4$	450 W Xe lamp, 8.0 mg catalyst, acetonitrile and triethanolamine (4:1 *v/v*) 4 mL mix in 11 mL Pyrex test tube	CO: 0.6, H$_2$: 0.25, HCOOH: 4 μmol·h^{-1}	Bulk g-C$_3$N$_4$ HCOOH: trace	N/A		[201]
26	SnO$_2$/g-C$_3$N$_4$	500 W Xe, 20 mg catalyst, 4 mL water injected into the bottom of the reactor, 0.3 MPa CO$_2$, 80 °C	CO: 19, CH$_4$: 2, CH$_3$OH: 3	Bulk g-C$_3$N$_4$ CO: 2.4, CH$_4$: trace, CH$_3$OH: 2.8, P25: CO: 3.5, CH$_3$OH: 1	CO: 7.9		[202]
27	Brookite TiO$_2$/g-C$_3$N$_4$	300 W Xe, 60 mg catalyst, CO$_2$ produced from reaction of NaHCO$_3$ (1.50 g) and H$_2$SO$_4$ solution (5.0 mL, 4 M)	CO: 0.84, CH$_4$: 5.21	Bulk g-C$_3$N$_4$ CO: 7.10, CH$_4$: 1.84	CH$_4$: 2.83		[203]
28	TiO$_2$/g-C$_3$N$_4$	8 W Hg lamp (λ = 254 nm; intensity = 0.5 mW/cm^2), vol of SS reactor 355 cm^3, 0.1 g catalyst, 140 kPa CO$_2$	CO: 2.8, CH$_4$: 8.5, H$_2$:41	Bulk g-C$_3$N$_4$ CO: 0.93, CH$_4$: 4.75, H$_2$: 16.25	CO: 3		[204]
29	g-C$_3$N$_4$/WO$_3$	LED (λ = 435 nm) at 3.0 mW cm^2, 3 mg catalyst in 5 mL ion-exchanged water.	CH$_3$OH: 1.1 μmol, 0.5 wt % Au and Ag 2.5 and 1.5 μmol, resp.	Bulk g-C$_3$N$_4$ CH$_3$OH: 0.6 μmol	1.83		[205]
30	g-C$_3$N$_4$/ZnO	300 W Xe lamp, 200 mL Pyrex reactor, 100 mg catalyst CO$_2$ and H$_2$O vapor produced by NaHCO$_3$ (0.12 g) and HCl (0.25 mL, 4 M)	CH$_3$OH: 0.6	Bulk g-C$_3$N$_4$: CH$_3$OH: 0.26 Pure ZnO: CH$_3$OH: 0.37	2.3		[165]
31	ZnO/g-C$_3$N$_4$	500 W Xe/420 nm, steel reactor 132 mL, 10 mg catalyst in 4 mL H$_2$O, 0.4 MPa CO$_2$ and 80 °C	CO: 29, CH$_3$CHO: 9, CH$_4$: 3.5, C$_2$H$_5$OH: 1.5	Bulk g-C$_3$N$_4$ CO: 4.5, CH$_3$CHO: 4.3, CH$_4$: 0.5, C$_2$H$_5$OH: trace P25 CO: 4.5, CH$_3$CHO: 3, CH$_4$: 2, C$_2$H$_5$OH: trace	CO: 6.4		[206]
32	Co-porphyrin/g-C$_3$N$_4$	300 W Xe (UV/IR cut-off filter), 1 mL of TEOA and 4 mL of MeCN were mixed and injected into the cell, 80 kPa CO$_2$	CO: 17	Bulk g-C$_3$N$_4$ CO: 1.4	12.14	0.80 (420 nm)	[207]
33	Co-(bpy)$_3$Cl$_2$/g-C$_3$N$_4$	300 W Xe lamp with a 420 nm cut-off, 50 mg catalyst, MeCN (4 mL), TEOA (2 mL), CO$_2$ (1 bar), 60 °C	CO: 37 H2: 6		N/A		[176]
34	g-C$_3$N$_4$/Bi$_2$WO$_6$	300 W Xe/420 nm cut-off filter, reactor 500 mL, 0.1 g catalyst, CO$_2$ and H$_2$O vapour mixer	CO: 5.19	pure g-C$_3$N$_4$ CO: 0.23	22		[208]

No.	Photocatalyst	Reaction Conditions	Product Yield	Reference Yield	Ratio	AQE	Ref.
				Bi_2WO_6 CO: 0.81			
35	g-C_3N_4/$Bi_4O_5I_2$	300 W Xe lamp with 400 nm cut-off filter, 0.10 g catalyst, Pyrex glass 350 mL, 5 mL H_2SO_4 (4 M) with $NaHCO_3$ to achieve 1 bar CO_2, 15 °C	CO: 45.6	Bulk g-C_3N_4 CO: 5.8	7.86		[209]
36	Core–shell LaPO$_4$/g-C_3N_4 nanowires	300 W Xe lamp, reactor volume 500 mL, 30 mg catalyst, CO_2 and water vapor	CO: 14.43	0.41	10		[210]
37	CdIn$_2$S$_4$/mp g-C_3N_4	300 W Xe lamp with 420 nm cut-off filter, 0.1 g catalyst in 100 mL water containing 0.1 M NaOH, ultrapure CO_2 was continuously bubbled through	CH$_3$OH: 42.7	pure CdIn$_2$S$_4$ CH$_3$OH: 23.1	1.84	0.14 (420 nm)	[211]
38	Mesoporous phosphorylated g-C_3N_4	300 W Xe lamp, Pyrex glass 350 mL, 0.2 g catalyst, 5 mL of 4 M H_2SO_4 with $NaHCO_3$ (1.0 g) to give 1 bar CO_2 10 °C	CO: 20, CH$_4$: 40, H$_2$: 3, O$_2$: 10	CO: 4.5, CH$_4$: 4, H$_2$: 0.5, O$_2$: 1.75	CH$_4$: 10	0.85 (420 nm)	[212]
39	Pt-g-C_3N_4/KNbO$_3$	300 W Xe lamp with 420 nm cut-off filter, 0.1 g catalyst, CO_2, 2 mL of H_2O	CH$_4$: 2.37	CH$_4$: 0.62	3.8		[213]
40	g-C_3N_4/BiOBr/Au	300 W Xe lamp ($\lambda = 380$ nm), 350 mL Pyrex glass, 0.1 g catalyst, 5 mL H_2SO_4 (4 M) + 1.3 g $NaHCO_3$ to give 1 bar CO_2	CO: 6.67 CH$_4$: 0.92	N/A	N/A		[214]
41	g-C_3N_4/Ag-TiO$_2$	300 W Xe, 50 mg catalyst, CO_2 flow rate of 3 mL·min^{-1}, 45 °C	CH$_4$: 9.33 and CO: 6.33	N/A	N/A		[183]

5.2. Environmental Remediation

Many large-scale processes operated by the petrochemical, textile and food industries discharge polluted water into the aquatic environment [215]. Organic dyes are often used in textile, printing, and photographic industries, and a sizable fraction of these are lost during the dying process into effluent wastewater streams. Even low concentrations of such dyes pose serious risks to human and animal health, and their bio- or chemical degradation is challenging [216,217], hence the development advanced oxidation processes (AOPs) to treat contaminated drinking ground and surface waters, and wastewaters containing toxic or non-biodegradable compounds are sought [218,219]. Semiconductor photocatalysis offer an effective and economic approach to the treatment of recalcitrant organic compounds at low concentrations in wastewater [220–223]. Photoexcited holes are the key active species in such photocatalytic environmental remediation, being powerful oxidants in their own right, or reacting with water to produce hydroxyl radicals ($^{\bullet}$OH) which are themselves powerful oxidants with an oxidation potential of 2.8 eV (NHE). Reactively-formed $^{\bullet}$OH can rapidly attack adsorbed pollutants at the surface of photocatalysts or in solution, to achieve their mineralization as CO_2 and water. Mechanisms for the photocatalytic oxidation of organic pollutants in water are widely discussed in the literature [4,221,222]. Briefly:

$$SC + h\nu \rightarrow SC^*(e_{CB}^- + h_{VB}^+) \tag{13}$$

$$h_{VB}^+ + H_2O \rightarrow {}^{\bullet}OH + H^+ \tag{14}$$

$$O_2 + e_{CB}^- \rightarrow O_2^{\bullet-} \tag{15}$$

$$O_2^{\bullet-} + H^+ \rightarrow HO_2^{\bullet} \tag{16}$$

$$HO_2^{\bullet} + HO_2^{\bullet} \rightarrow H_2O_2 + O_2 \tag{17}$$

$$O_2^{\bullet-} + HO_2^{\bullet} \rightarrow O_2 + HO_2^- \tag{18}$$

$$HO_2^- + H^+ \rightarrow H_2O_2 \tag{19}$$

$$H_2O_2 + h\nu \rightarrow 2\,{}^{\bullet}OH \tag{20}$$

$$H_2O_2 + O_2^{\bullet-} \rightarrow {}^{\bullet}OH + OH^- + O_2 \tag{21}$$

$$H_2O_2 + e_{CB}^- \rightarrow {}^{\bullet}OH + OH^- \tag{22}$$

$$\text{Organic Compound} + {}^{\bullet}OH \rightarrow \text{degradation products} \tag{23}$$

$$\text{Organic Compound} + SC(h^+) \rightarrow \text{degradation products} \tag{24}$$

$$\text{Organic Compound} + SC(e^-) \rightarrow \text{degradation products} \tag{25}$$

A variety of active radicals, including $O_2^{\bullet-}$, $^{\bullet}$OH, $HO_2^{\bullet}$, in addition to H_2O_2 have been invoked as the oxidants responsible for mineralization, with $^{\bullet}$OH the most likely candidate Equation (23). Direct oxidation of carboxylic acids by photoexcited holes to generate CO_2 Equation (24) has also been evidenced, termed the 'photo-Kolbe reaction'. Reductive pathways involving photoexcited electrons Equation (25) are considered unimportant in dye degradation; however, thermodynamic requirements for semiconductor photocatalysts dictate that the VB and CB should be positioned such that the oxidation potential of hydroxyl radicals $E^0_{(H_2O/\,^{\bullet}OH)} = +2.8$ eV (NHE) and reduction potential of superoxide radicals $E^0_{(O_2/O_2^{\bullet-})} = -0.3$ eV (NHE) lie well within the band gap. In other words, the redox potential of photoexcited holes must be sufficiently positive to generate $^{\bullet}$OH radicals, and that of photoexcited electrons sufficiently negative to generate $O_2^{\bullet-}$.

Considerable efforts have been devoted to developing photocatalysts for water purification under solar irradiation. g-C$_3$N$_4$ based nanostructures are potential photocatalysts for the degradation of various pollutants [39,42], with photophysical properties of the parent nitride modified through doping with heteroatoms, heterojunction formation with other materials, and textural improvements to enhance surface area and porosity. For example, ultrathin g-C$_3$N$_4$ nanosheets derived from bulk g-C$_3$N$_4$ by exfoliation in methanol exhibit enhanced photocatalytic performance for methylene blue (MB) degradation [65]. g-C$_3$N$_4$ nanotubes show superior photoactivity under visible light for MB degradation than bulk g-C$_3$N$_4$ or P25 [74]. Tahir and co-workers also employed tubular g-C$_3$N$_4$ for MB and methyl orange (MO) photocatalytic degradation under visible light, observing better stability and activity than bulk g-C$_3$N$_4$, attributed to the high surface area (182 m^2·g^{-1}) and improved light absorption and charge separation/transfer [75]. 1D g-C$_3$N$_4$ nanorods with different aspect ratios have been screened for MB degradation under visible light (λ > 420 nm) and simulated solar irradiation (λ > 290 nm) [68]. The resulting photocatalytic activity and photocurrent response of g-C$_3$N$_4$ nanorods under visible light were 1.5–2.0 times that of g-C$_3$N$_4$ nanoplates. A simple chemical route was reported for preparing nanofiber-like g-C$_3$N$_4$ structures which showed promising activity for Rhodamine B (RhB) photodegradation [73].

g-C$_3$N$_4$ doping is a common strategy to broaden spectral utilization and band alignment to drive separate photogenerated charge carriers. Doping by metals such as Cu and Fe [224–226], non-metals such as B, C, O, or S [224,227–231], and co-doping [232–234] have all been employed for environmental depollution applications. For example, S and O co-doped g-C$_3$N$_4$ prepared by melamine polymerization and subsequent H$_2$O$_2$ activation prior to trithiocyanuric acid functionalization (Figure 21a) enhanced the photocatalytic degradation of RhB (Figure 21b) 6-fold relative to the parent g-C$_3$N$_4$ nanosheet [235]. Doping resulted in a strongly delocalized HOMO and LUMO that increased the number of active sites and improved the separation of photogenerated electrons and holes.
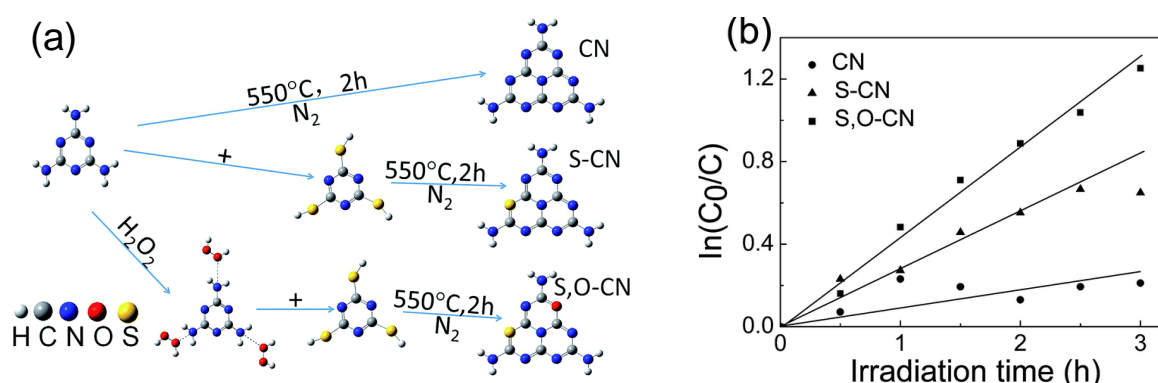

Figure 21. (**a**) Synthetic strategy, and (**b**) photocatalytic activity of S and O co-doped g-C$_3$N$_4$ for RhB degradation. Reproduced with permission from [235]. Copyright Royal Society of Chemistry, 2017.

Plasmonic photocatalysts have also been exploited for environmental remediation, for example, 7–15 nm Au and Pt nanoparticles photodeposited on g-C$_3$N$_4$ are promising for the photocatalytic degradation of tetracycline chloride as a representative antibiotic whose uncontrolled release is of concern [236]. The Au surface plasmon resonance broadens the optical adsorption range, while Pt acts as a sink for photoexcited electrons. The combination of noble metals and g-C$_3$N$_4$ enables tunable heterojunctions with improved charge transport than traditional nanocomposites [237–243], and such multicomponent heterostructures are a promising solution to environmental depollution [39,40,42], for example g-C$_3$N$_4$/Ag$_3$PO$_4$ systems for MO degradation [242,243]. Ag$_3$PO$_4$@g-C$_3$N$_4$ core–shell photocatalysts have also been applied to MB degradation under visible light, achieving 97% conversion in 30 min compared with only 79% for a physical mixture of the Ag$_3$PO$_4$ and g-C$_3$N$_4$ components, and 69% for pure Ag$_3$PO$_4$. The g-C$_3$N$_4$ shell may protect Ag$_3$PO$_4$ from dissolution in the composite, conferring superior stability. Core–shell g-C$_3$N$_4$@TiO$_2$ photocatalysts synthesized by a sol–gel and in situ re-assembly route and subsequently applied to phenol removal under visible light

were seven times more photoactive than bulk g-C$_3$N$_4$. Increasing the g-C$_3$N$_4$ shell thickness from 0 to 1 nm increased the photodegradation rate constant from 0.0018 to 0.0386 h^{-1}; however, thicker shells slowed charge transport to the external photocatalyst surface, lowering activity. Z-scheme N-doped ZnO/g-C$_3$N$_4$ hybrid core–shell nanostructures (Figure 22Aa,b) were successfully prepared via a facile, low-cost, and eco-friendly ultrasonic dispersion method [244]. The g-C$_3$N$_4$ shell thickness was tuned by varying the g-C$_3$N$_4$ loading. Direct contact between the N-doped ZnO core and g-C$_3$N$_4$ shell introduced a new energy level into the N-doped ZnO band gap, effectively narrowing the band gap. Consequently, these hybrid core–shell nanostructures showed greatly enhanced visible light photocatalysis for RhB degradation compared to pure N-doped ZnO surface or g-C$_3$N$_4$ components (Figure 22Ac) [240]. A facile, reproducible, and template-free synthesis has also been demonstrated to prepare magnetically separable g-C$_3$N$_4$–Fe$_3$O$_4$ nanocomposites (Figure 22Ba) [37]. Monodispersed Fe$_3$O$_4$ nanoparticles with 8 nm diameter were uniformly deposited over g-C$_3$N$_4$ sheets (Figure 22Bb) and exhibited enhanced charge separation and photocatalytic activity for RhB degradation under visible light irradiation (Figure 22Bc). These g-C$_3$N$_4$–Fe$_3$O$_4$ nanocomposites showed good stability with negligible loss in photocatalytic activity even after six recycles, and facilitated magnetic catalyst recovery (Figure 22Bd). Xiao et al. demonstrated that the excellent stability of g-C$_3$N$_4$ towards photocatalytic oxidation in the presence of organic pollutants reflects strong competition of the latter for •OH radicals under practical working conditions, resulting in preferential decomposition of the pollutants rather than the carbon nitride [245].
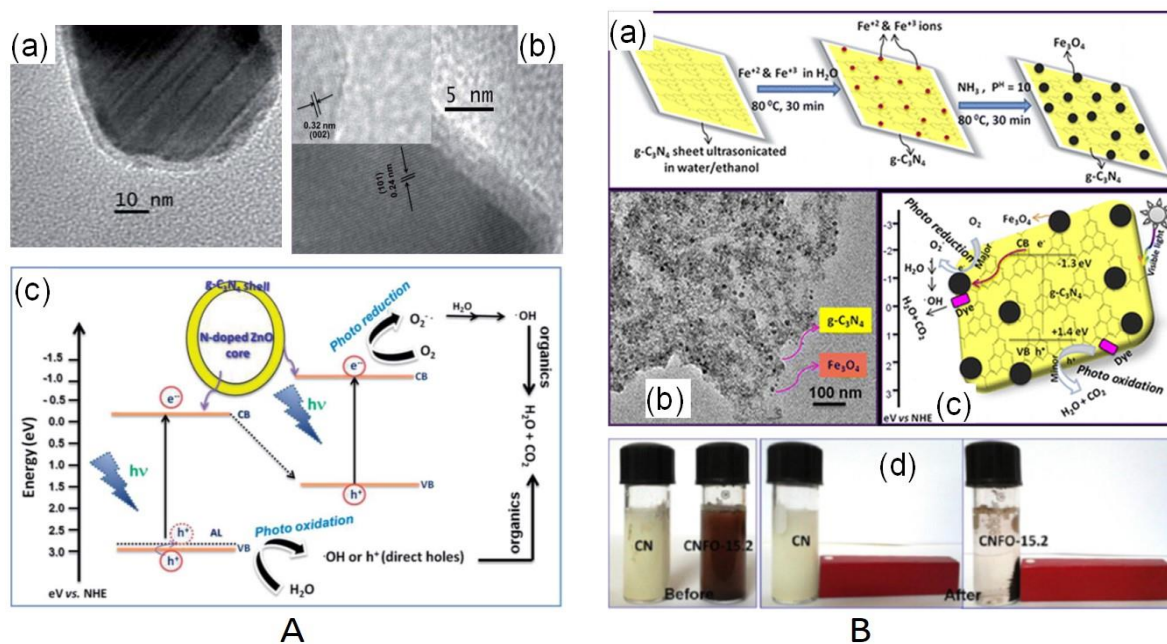
Figure 22. (**A**) (**a**,**b**) TEM images of N-ZnO-g-C$_3$N$_4$ core–shell nanoplates, and associated (**c**) Z-scheme mechanism. Reproduced from with permission from [244]. Copyright 2014 Royal Society of Chemistry. (**B**) (**a**) Synthetic strategy, (**b**) TEM image, and (**c**) photodegradation mechanism for g-C$_3$N$_4$–Fe$_3$O$_4$ nanocomposite, and (**d**) magnetic separation of photocatalyst post-reaction. Reprinted with permission from [37]. Copyright 2013 American Chemical Society.

Several multicomponent nanocomposites based on g-C$_3$N$_4$ nanosheets such as Au@g-C$_3$N$_4$–PANI [246], Au-NYF/g-C$_3$N$_4$ [105], g-C$_3$N$_4$/CNTs/Al$_2$O$_3$ [247], AgCl/Ag$_3$PO$_4$/g-C$_3$N$_4$ [248], and g-C$_3$N$_4$/Zn$_{0.11}$Sn$_{0.12}$Cd$_{0.88}$S$_{1.12}$ [249] are also reported; the performance of different g-C$_3$N$_4$ photocatalysts for the photodegradation of representative aqueous pollutants is summarized in Table 3.

Table 3. Photocatalytic degradation of aqueous pollutants over g-C_3N_4 nanostructured catalysts.

Entry	Photocatalyst	Organic Molecule	Experimental Details	Removal Efficiency/%	Reference Material Efficiency/%	Enhancement Relative to Conventional g-C_3N_4	Reference
1	g-C_3N_4@TiO_2 core–shell structure	Phenol	5 mg·L^{-1} phenol with 25 mg catalyst. 500 W Xe lamp with 420 nm cut-off filter, 23 mW/cm^2.	30	4.2	7.2	[250]
2	Ag-decorated S-doped g-C_3N_4	Bisphenol A (BPA)	50 mL of 10 mg·L^{-1} of BPA, catalyst loading of 0.60 g·L^{-1}. Light source, 155 W Xe arc lamp with the solar region of 280–630 nm.	95	31.66	3	[233]
3	Ultrathin urea-derived g-C_3N_4 nanosheets	p-Nitrophenol (PNP)	100 mg catalyst, aqueous PNP (10 mg L^{-1}, 100 mL). 300 W Xe lamp equipped with an IR cut filter and a 400 nm cut filter.	95	60	1.58	[251]
4	Mesoporous g-C_3N_4/TiO_2	Decomposition of dinitro butyl phenol (DNBP)	25 mg catalyst added to DNBP aqueous solution (20 mg·L^{-1}) with 500 W xenon lamp with λ < 420 nm using cut-off filter.	98.5	65	1.5	[252]
5	C_3N_4-nanosheets	Methylene blue (MB)	10 mg catalyst in 50 mL of 10 mg·L^{-1} MB solution. 150 W Xe lamp as the simulated sunlight source.	98	7.9	12.4	[253]
6	Z-scheme graphitic-C_3N_4/Bi_2MoO_6	Methylene blue	30 mL of 10 mg·L^{-1} MB solution, 0.03 g catalyst. 50 W LED light with of 410 nm emission.	90	18.75	4.8	[254]
7	Sm_2O_3/S-doped g-C_3N_4	Methylene blue	100 mL of MB solution (8 mg·L^{-1}), 300 W halogen lamp with UV-stop feature.	93	27	3.5	[255]
8	Porous CeO_2/sulfur-doped g-C_3N_4	Methylene blue	0.06–0.12 g catalyst in 6–14 mg L^{-1} MB, visible light (λ > 400 nm) 300 W Halogen lamp with UV stop.	91.4	25	3.65	[256]
9	ZnS/g-C_3N_4	Methylene blue	200 mL MB (6 mg·L^{-1}), 30 mg catalyst under visible light source, 100 W halogen lamp.	90	34.6	2.6	[257]

10	Mesoporous Carbon Nitride Decorated with Cu Particles	Methyl orange (MO)	0.07 g catalyst in 100 mL of MO (11 mg L^{-1}) solution under visible-light, 300 W halogen lamp with UV-stop feature.	100	28	3.57	[258]
11	Plasmonic Ag–AgBr/g-C$_3$N$_4$	Methyl orange	MO solution (100 mL, 10 mg L^{-1}), 50 mg catalyst, 300 W Xe lamp with 400 nm cut-off filter.	90	14.3	6.3	[259]
12	ZnFe$_2$O$_4$ nanoparticles on g-C$_3$N$_4$ sheets	Methyl orange	100 mL of 10 mg·L^{-1} MO solution, 25 mg catalyst. 500 W Xe lamp with cold filter.	98	15.31	6.4	[260]
13	AgNPs/g-C$_3$N$_4$ nanosheets	Methyl orange	50 mL 0.02 mmol/L MO solution, 25 mg catalyst. 300 W Xe lamp with a visible light reflector (350 nm < *l* < 780 nm) and a 420 nm longwave-pass cut-off filter (*l* > 420 nm).	95.2	13.8	7	[261]
14	BiOCl/C$_3$N$_4$ hybrid nanocomposite	Methyl orange	15 mL of 10 mg L^{-1} MO solution, 10 mg catalyst. 300 W Xe lamp equipped with 420 nm cut-off filter.	84.28	14	6	[262]
15	g-C$_3$N$_4$/GO aerogel	Methyl orange	50 mL of 20 mg L^{-1} MO solution. 300 W Xe lamp with a cut off filter ($\lambda >$ 420 nm).	91.1	33	2.76	[263]
16	g-C$_3$N$_4$ nanocrystals decorated Ag$_3$PO$_4$ hybrids	Methyl orange	80 mL MO, 80 mg catalyst. 500 W halogen lamp equipped with cut-off filters (420 nm < λ < 800 nm).	92	44	2	[264]
17	g-C$_3$N$_4$-NS/CuCr$_2$O$_4$ nanocomposites	Rhodamine B (RhB)	250 mL of 2.5 × 10^{-5} M RhB solution, 0.1 g of catalyst. 50 W LED lamp.	98.9	30	3.3	[265]
18	Porous Mn doped g-C$_3$N$_4$	Rhodamine B	100 mL of 10 mg·L^{-1} RhB solution, 50 mg catalyst. 300 W Xe lamp equipped with ultraviolet cut-off filter (>400 nm).	88.9	18	4.9	[266]
19	Mesoporous carbon nitride (mpg-C$_3$N$_4$/SnCoS$_4$)	Rhodamine B	100 mL of 20 mg·L^{-1} RhB solution, 20 mg catalyst. 300 W Xe lamp equipped with an UV cut-off filter ($\lambda \geq$ 420 nm).	70	13	5.4	[267]

20	Iron oxyhydroxide/ultrathin g-C$_3$N$_4$ nanosheets	Rhodamine B	50 mL of 10 mg·L^{-1} RhB solution, 50 mg catalyst. 500 W Xe lamp equipped with a cut-off filter ($\lambda \geq$ 420 nm).	98	5.5	17.8	[268]
21	Two-dimensional g-C$_3$N$_4$/Bi$_2$WO$_6$	Rhodamine B	100 mL of 10 mg L^{-1} RhB solution, 100 mg catalyst. 300 W Xe lamp with UV cut-off filter.	80	23.5	3.4	[269]
22	Ultrathin g-C$_3$N$_4$ nanosheets	Rhodamine B	100 mL of 20 mg L^{-1} RhB solution, 100 mg catalyst. 300 W Xe lamp (>420 nm).	99	16.2	6.1	[270]
23	Z-scheme g-C$_3$N$_4$/TiO$_2$ nanotube	Rhodamine B	20 mL of 5 mg·L^{-1} RhB solution, 2 cm × 2 cm catalyst film. 300 W Xe lamp with UV cut-off filter.	67	47.85	1.4	[271]
24	WO$_3$@g-C$_3$N$_4$	Rhodamine B	50 mL of 10 mg L^{-1} RhB solution, 10 mg catalyst. Xe lamp with 400 nm cut-off filter, 100 mW cm^{-2}.	90	25.7	3.5	[272]
25	Mesoporous graphitic carbon nitride modified PbBiO$_2$Br	Rhodamine B	100 mL of 10 mg·L^{-1} RhB solution, 30 mg catalyst. 300 W Xe lamp with UV cut-off filter (>400 nm).	98	N/A	N/A	[273]
26	g-C$_3$N$_4$/CuS p-n heterojunctions	Rhodamine B	30 mL of 10 mg L^{-1} RhB solution, 10 mg catalyst. 300 W Xe lamp with 420 nm cut-off filter.	93	27	3.5	[274]
27	g-C$_3$N$_4$/kaolinite composites	Rhodamine B	100 mL of 10 ppm RhB solution, 200 mg catalyst. 500 W Xenon lamp with 400 nm cut-off filter.	90	21.8	4.1	[275]
28	Hexagonal boron nitride (h-BN) decorated g-C$_3$N$_4$	Rhodamine B	100 mL of 20 mg L^{-1} RhB solution, 50 mg catalyst. 300 W Xe lamp with 420 nm cut-off filter.	99.5	13.63	7.3	[276]
29	ZnO/g-C$_3$N$_4$	Rhodamine B	50 mL of 10 mg L^{-1} RhB solution, 50 mg catalyst. 500 W Xe lamp equipped with 420 nm cut-off filter.	51.3	24.43	2.1	[277]
30	Ag/AgO loaded g-C$_3$N$_4$ microspheres	Acid Violet-7 (AV-7)	100 mL of 20 mg·L^{-1} AV-7 solution, 100 mg catalyst. 12 × 100 W fluorescent lamps (mainly visible light, with only 3% UV).	98	48	2	[278]

31	g-C$_3$N$_4$/TiO$_2$/kaolinite composite	Ciprofloxacin (CIP) antibiotic	100 mL of 10 ppm CIP solution, 200 mg catalyst. Xe lamp (90 mW/cm^2) with 400 nm cut-off filter.	92	14.48	6.4	[279]
32	Z-scheme CdS/Fe$_3$O$_4$/g-C$_3$N$_4$	Ciprofloxacin	100 mL of 20 mg L^{-1} CIP, 50 mg photocatalyst. 300 W Xe lamp with UV filter (λ > 420 nm).	92	3.53	26	[280]
33	Carbon-Doped g-C$_3$N$_4$	Tetracycline (TC)	80 mL of 10^{-4} M TC, 40 mg catalyst. Sunlight (07/10/2015, Trivandrum, India, between 11 pm and 1 pm, 78,000–80,000 lux).	95	50	1.9	[231]
34	Phosphorous-doped ultrathin graphitic carbon nitride nanosheets	Tetracycline	100 mL of 10 mg·L^{-1} TC solution, 100 mg catalyst. 300 W Xe lamp equipped with UV cut-off filter (>420 nm).	96.95	71.78	1.35	[281]
35	Hierarchical WO$_3$/g-C$_3$N$_4$	Tetracycline hydrochloride (TC-HCl)	100 mL of 25 mg·L^{-1} TC-HCL solution, 50 mg catalyst. 300 W Xe lamp with 420 nm cut-off filter.	82	48	1.7	[282]
36	Co$_3$O$_4$ modified g-C$_3$N$_4$	Diclofenac sodium (DCF)	100 mL of 10 mg·L^{-1} DCF solution, 50 mg catalyst. 300 W Xe lamp with 420 nm cut-off filter.	100	17	5.9	[283]
37	silver and carbon quantum dots co-loaded with ultrathin g-C$_3$N$_4$	Naproxen NPX	50 mL of 4 mg·L^{-1} NPX solution, 50 mg catalyst. 350 W Xe lamp with 420 nm and 290 nm light for visible and simulated sunlight sources.	87.5	8.75	10	[284]
38	g-C$_3$N$_4$	Decabromodiphenyl ether (BDE209)	20 mL of 1 × 10^{-3} mol/L BDE209 solution, 20 mg catalyst. 300 W Xe lamp for UV-visible irradiation (>360 nm).	65	N/A	N/A	[285]
39	Metal-free sulfur doped g-C$_3$N$_4$	UO$_2^{2+}$ removal	200 mL of 0.12 mM UO$_2^{2+}$ solution, 100 mg catalyst. 350 W Xe lamp with a 420 nm cut-off filter.	95	71	1.3	[286]

6. Conclusions

g-C$_3$N$_4$ nanostructures offer tunable textural, electronic and optical properties that are amenable to tailoring for solar energy harvesting and subsequent photocatalytic transformations for energy and environmental applications. Diverse synthetic methods are available to prepare pure g-C$_3$N$_4$ nanostructures of different dimensionality and porosity, and to integrate these within multi-functional nanocomposites with enhanced solar spectral utilization, apparent quantum yields, charge separation and transport, and ultimately photocatalytic activity and stability. The sustainable production of H$_2$ as an energy vector from water splitting is perhaps the most promising application, although issues remain regarding the use of sacrificial reagents and a lack of interdisciplinary efforts to improve photoreactor design. Photocatalytic reduction of CO$_2$ is at a more preliminary stage, with improvements in both activity, and the ability to select specific products for either energy (e.g., CO, CH$_4$, methanol, and formic acid) or chemicals (e.g., >C$_2$ olefins or alkanes) pre-requisites to bench scale demonstrations. Wastewater treatment using g-C$_3$N$_4$-based photocatalysts appears promising; however, a lack of standardization in either reactor design or experimental protocols hampers quantitative comparisons due to issues such as decoupling adsorption versus reaction, and photocatalysis from direct photochemical activation of chromophores.

Conflicts of Interest: The authors declare no conflict of interest.

References

1. Lewis, N.S.; Nocera, D.G. Powering the planet: Chemical challenges in solar energy utilization. *Proc. Natl. Acad. Sci. USA* **2006**, *103*, 15729–15735.
2. Rhind, S.M. Anthropogenic pollutants: A threat to ecosystem sustainability? *Philos. Trans. R. Soc. B Biol. Sci.* **2009**, *364*, 3391–3401.
3. Faunce, T.; Styring, S.; Wasielewski, M.R.; Brudvig, G.W.; Rutherford, A.W.; Messinger, J.; Lee, A.F.; Hill, C.L.; deGroot, H.; Fontecave, M.; et al. Artificial photosynthesis as a frontier technology for energy sustainability. *Energy Environ. Sci.* **2013**, *6*, 1074–1076.
4. Mills, A.; Davies, R.H.; Worsley, D. Water purification by semiconductor photocatalysis. *Chem. Soc. Rev.* **1993**, *22*, 417–425.
5. Fujishima, A.; Honda, K. Electrochemical Photolysis of Water at a Semiconductor Electrode. *Nature* **1972**, *238*, 37–38.
6. Inoue, T.; Fujishima, A.; Konishi, S.; Honda, K. Photoelectrocatalytic reduction of carbon-dioxide in aqueous suspensions of semiconductor powders. *Nature* **1979**, *277*, 637–638.
7. Fujishima, A.; Zhang, X.T.; Tryk, D.A. TiO$_2$ photocatalysis and related surface phenomena. *Surf. Sci. Rep.* **2008**, *63*, 515–582.
8. Ma, Y.; Wang, X.; Jia, Y.; Chen, X.; Han, H.; Li, C. Titanium Dioxide-Based Nanomaterials for Photocatalytic Fuel Generations. *Chem. Rev.* **2014**, *114*, 9987–10043.
9. Gaya, U.I.; Abdullah, A.H. Heterogeneous photocatalytic degradation of organic contaminants over titanium dioxide: A review of fundamentals, progress and problems. *J. Photochem. Photobiol. C Photochem. Rev.* **2008**, *9*, 1–12.
10. Schneider, J.; Matsuoka, M.; Takeuchi, M.; Zhang, J.; Horiuchi, Y.; Anpo, M.; Bahnemann, D.W. Understanding TiO$_2$ Photocatalysis: Mechanisms and Materials. *Chem. Rev.* **2014**, *114*, 9919–9986.
11. Habisreutinger, S.N.; Schmidt-Mende, L.; Stolarczyk, J.K. Photocatalytic Reduction of CO$_2$ on TiO$_2$ and Other Semiconductors. *Angew. Chem. Int. Ed.* **2013**, *52*, 7372–7408.
12. Daghrir, R.; Drogui, P.; Robert, D. Modified TiO$_2$ for Environmental Photocatalytic Applications: A Review. *Ind. Eng. Chem. Res.* **2013**, *52*, 3581–3599.
13. Nakata, K.; Fujishima, A. TiO$_2$ photocatalysis: Design and applications. *J. Photochem. Photobiol. C Photochem. Rev.* **2012**, *13*, 169–189.
14. Asahi, R.; Morikawa, T.; Ohwaki, T.; Aoki, K.; Taga, Y. Visible-Light Photocatalysis in Nitrogen-Doped Titanium Oxides. *Science* **2001**, *293*, 269–271.

15. Kumar, S.G.; Devi, L.G. Review on Modified TiO$_2$ Photocatalysis under UV/Visible Light: Selected Results and Related Mechanisms on Interfacial Charge Carrier Transfer Dynamics. *J. Phys. Chem. A* **2011**, *115*, 13211–13241.

16. Moniz, S.J.A.; Shevlin, S.A.; Martin, D.J.; Guo, Z.-X.; Tang, J. Visible-light driven heterojunction photocatalysts for water splitting—A critical review. *Energy Environ. Sci.* **2015**, *8*, 731–759.

17. Rochkind, M.; Pasternak, S.; Paz, Y. Using Dyes for Evaluating Photocatalytic Properties: A Critical Review. Molecules. *Molecules* **2015**, *20*, 88–110.

18. Barbero, N.; Vione, D. Why Dyes Should Not Be Used to Test the Photocatalytic Activity of Semiconductor Oxides. *Environ. Sci. Technol.* **2016**, *50*, 2130–2131.

19. Styring, S. Artificial photosynthesis for solar fuels. *Faraday Discuss.* **2012**, *155*, 357–376.

20. Listorti, A.; Durrant, J.; Barber, J. Solar to fuel. *Nat. Mater.* **2009**, *8*, 929–930.

21. Chen, D.; Zhang, X.; Lee, A.F. Synthetic strategies to nanostructured photocatalysts for CO$_2$ reduction to solar fuels and chemicals. *J. Mater. Chem. A* **2015**, *3*, 14487–14516.

22. Nosaka, Y.; Nosaka, A.Y. Generation and Detection of Reactive Oxygen Species in Photocatalysis. *Chem. Rev.* **2017**, *117*, 11302–11336.

23. Karamian, E.; Sharifnia, S. On the general mechanism of photocatalytic reduction of CO$_2$. *J. CO$_2$ Util.* **2016**, *16*, 194–203.

24. White, J.L.; Baruch, M.F.; Pander, J.E.; Hu, Y.; Fortmeyer, I.C.; Park, J.E.; Zhang, T.; Liao, K.; Gu, J.; Yan, Y.; et al. Light-Driven Heterogeneous Reduction of Carbon Dioxide: Photocatalysts and Photoelectrodes. *Chem. Rev.* **2015**, *115*, 12888–12935.

25. Kubacka, A.; Fernández-García, M.; Colón, G. Advanced Nanoarchitectures for Solar Photocatalytic Applications. *Chem. Rev.* **2012**, *112*, 1555–1614.

26. Frank, S.N.; Bard, A.J. Heterogeneous photocatalytic oxidation of cyanide ion in aqueous solutions at titanium dioxide powder. *J. Am. Chem. Soc.* **1977**, *99*, 303–304.

27. Lee, K.M.; Lai, C.W.; Ngai, K.S.; Juan, J.C. Recent developments of zinc oxide based photocatalyst in water treatment technology: A review. *Water Res.* **2016**, *88*, 428–448.

28. Li, L.; Chu, Y.; Liu, Y.; Dong, L. Template-Free Synthesis and Photocatalytic Properties of Novel Fe$_2$O$_3$ Hollow Spheres. *J. Phys. Chem. C* **2007**, *111*, 2123–2127.

29. Wang, W.; Cheng, B.; Yu, J.; Liu, G.; Fan, W. Visible-Light Photocatalytic Activity and Deactivation Mechanism of Ag$_3$PO$_4$ Spherical Particles. *Chem. Asian J.* **2012**, *7*, 1902–1908.

30. Kato, H.; Kudo, A. Visible-Light-Response and Photocatalytic Activities of TiO$_2$ and SrTiO$_3$ Photocatalysts Codoped with Antimony and Chromium. *J. Phys. Chem. B* **2002**, *106*, 5029–5034.

31. Kato, H.; Kudo, A. Water Splitting into H$_2$ and O$_2$ on Alkali Tantalate Photocatalysts ATaO$_3$ (A = Li, Na, and K). *J. Phys. Chem. B* **2001**, *105*, 4285–4292.

32. Jing, D.; Guo, L. A Novel Method for the Preparation of a Highly Stable and Active CdS Photocatalyst with a Special Surface Nanostructure. *J. Phys. Chem. B* **2006**, *110*, 11139–11145.

33. Pan, C.; Zhu, Y. New Type of BiPO$_4$ Oxy-Acid Salt Photocatalyst with High Photocatalytic Activity on Degradation of Dye. *Environ. Sci. Technol.* **2010**, *44*, 5570–5574.

34. Wang, X.; Maeda, K.; Thomas, A.; Takanabe, K.; Xin, G.; Carlsson, J.M.; Domen, K.; Antonietti, M. A metal-free polymeric photocatalyst for hydrogen production from water under visible light. *Nat. Mater.* **2009**, *8*, 76–80.

35. Hernandez-Alonso, M.D.; Fresno, F.; Suarez, S.; Coronado, J.M. Development of alternative photocatalysts to TiO$_2$: Challenges and opportunities. *Energy Environ. Sci.* **2009**, *2*, 1231–1257.

36. Herron, J.A.; Kim, J.; Upadhye, A.A.; Huber, G.W.; Maravelias, C.T. A general framework for the assessment of solar fuel technologies. *Energy Environ. Sci.* **2015**, *8*, 126–157.

37. Kumar, S.; Kumar, B.; Baruah, A.; Shanker, V. Synthesis of Magnetically Separable and Recyclable g-C$_3$N$_4$–Fe$_3$O$_4$ Hybrid Nanocomposites with Enhanced Photocatalytic Performance under Visible-Light Irradiation. *J. Phys. Chem. C* **2013**, *117*, 26135–26143.

38. Kumar, S.; Surendar, T.; Baruah, A.; Shanker, V. Synthesis of a novel and stable g-C$_3$N$_4$-Ag$_3$PO$_4$ hybrid nanocomposite photocatalyst and study of the photocatalytic activity under visible light irradiation. *J. Mater. Chem. A* **2013**, *1*, 5333–5340.

39. Ong, W.-J.; Tan, L.-L.; Ng, Y.H.; Yong, S.-T.; Chai, S.-P. Graphitic Carbon Nitride (g-C$_3$N$_4$)-Based Photocatalysts for Artificial Photosynthesis and Environmental Remediation: Are We a Step Closer to Achieving Sustainability? *Chem. Rev.* **2016**, *116*, 7159–7329.

40. Fu, J.; Yu, J.; Jiang, C.; Cheng, B. g-C₃N₄-Based Heterostructured Photocatalysts. *Adv. Energy Mater.* **2017**, doi:10.1002/aenm.201701503.

41. Wang, X.; Blechert, S.; Antonietti, M. Polymeric Graphitic Carbon Nitride for Heterogeneous Photocatalysis. *ACS Catal.* **2012**, *2*, 1596–1606.

42. Dong, G.; Zhang, Y.; Pan, Q.; Qiu, J. A fantastic graphitic carbon nitride (g-C₃N₄) material: Electronic structure, photocatalytic and photoelectronic properties. *J. Photochem. Photobiol. C Photochem. Rev.* **2014**, *20*, 33–50.

43. Zhu, J.; Xiao, P.; Li, H.; Carabineiro, S.A.C. Graphitic Carbon Nitride: Synthesis, Properties, and Applications in Catalysis. *ACS Appl. Mater. Interfaces* **2014**, *6*, 16449–16465.

44. Jariwala, D.; Sangwan, V.K.; Lauhon, L.J.; Marks, T.J.; Hersam, M.C. Carbon nanomaterials for electronics, optoelectronics, photovoltaics, and sensing. *Chem. Soc. Rev.* **2013**, *42*, 2824–2860.

45. Hu, M.; Yao, Z.; Wang, X. Graphene-Based Nanomaterials for Catalysis. *Ind. Eng. Chem. Res.* **2017**, *56*, 3477–3502.

46. Chen, A.; Chatterjee, S. Nanomaterials based electrochemical sensors for biomedical applications. *Chem. Soc. Rev.* **2013**, *42*, 5425–5438.

47. Su, S.; Wu, W.; Gao, J.; Lu, J.; Fan, C. Nanomaterials-based sensors for applications in environmental monitoring. *J. Mater. Chem.* **2012**, *22*, 18101–18110.

48. Mandal, G.; Ganguly, T. Applications of nanomaterials in the different fields of photosciences. *Indian J. Phys.* **2011**, *85*, 1229, doi:10.1007/s12648-011-0149-9.

49. Anpo, M.; Shima, T.; Kodama, S.; Kubokawa, Y. Photocatalytic hydrogenation of propyne with water on small-particle titania: Size quantization effects and reaction intermediates. *J. Phys. Chem.* **1987**, *91*, 4305–4310.

50. Chen, X.; Mao, S.S. Titanium Dioxide Nanomaterials: Synthesis, Properties, Modifications, and Applications. *Chem. Rev.* **2007**, *107*, 2891–2959.

51. Lu, X.; Wang, C.; Wei, Y. One-Dimensional Composite Nanomaterials: Synthesis by Electrospinning and Their Applications. *Small* **2009**, *5*, 2349–2370.

52. Daniel, M.-C.; Astruc, D. Gold Nanoparticles: Assembly, Supramolecular Chemistry, Quantum-Size-Related Properties, and Applications toward Biology, Catalysis, and Nanotechnology. *Chem. Rev.* **2004**, *104*, 293–346.

53. Yoshihide, W. Atomically precise cluster catalysis towards quantum controlled catalysts. *Sci. Technol. Adv. Mater.* **2014**, *15*, 063501, doi:10.1088/1468-6996/15/6/063501.

54. Claus, P.; Brückner, A.; Mohr, C.; Hofmeister, H. Supported Gold Nanoparticles from Quantum Dot to Mesoscopic Size Scale: Effect of Electronic and Structural Properties on Catalytic Hydrogenation of Conjugated Functional Groups. *J. Am. Chem. Soc.* **2000**, *122*, 11430–11439.

55. Bell, A.T. The Impact of Nanoscience on Heterogeneous Catalysis. *Science* **2003**, *299*, 1688–1691.

56. Hu, L.; Peng, Q.; Li, Y. Selective Synthesis of Co₃O₄ Nanocrystal with Different Shape and Crystal Plane Effect on Catalytic Property for Methane Combustion. *J. Am. Chem. Soc.* **2008**, *130*, 16136–16137.

57. Kumar, S.; Parlett, C.M.A.; Isaacs, M.A.; Jowett, D.V.; Douthwaite, R.E.; Cockett, M.C.R.; Lee, A.F. Facile synthesis of hierarchical Cu₂O nanocubes as visible light photocatalysts. *Appl. Catal. B Environ.* **2016**, *189*, 226–232.

58. McLaren, A.; Valdes-Solis, T.; Li, G.; Tsang, S.C. Shape and Size Effects of ZnO Nanocrystals on Photocatalytic Activity. *J. Am. Chem. Soc.* **2009**, *131*, 12540–12541.

59. Li, Y.-F.; Liu, Z.-P. Particle Size, Shape and Activity for Photocatalysis on Titania Anatase Nanoparticles in Aqueous Surroundings. *J. Am. Chem. Soc.* **2011**, *133*, 15743–15752.

60. Luo, B.; Liu, G.; Wang, L. Recent advances in 2D materials for photocatalysis. *Nanoscale* **2016**, *8*, 6904–6920.

61. Niu, P.; Zhang, L.; Liu, G.; Cheng, H.-M. Graphene-Like Carbon Nitride Nanosheets for Improved Photocatalytic Activities. *Adv. Funct. Mater.* **2012**, *22*, 4763–4770.

62. Alivisatos, A.P. Semiconductor Clusters, Nanocrystals, and Quantum Dots. *Science* **1996**, *271*, 933–937.

63. Zhang, X.; Xie, X.; Wang, H.; Zhang, J.; Pan, B.; Xie, Y. Enhanced Photoresponsive Ultrathin Graphitic-Phase C₃N₄ Nanosheets for Bioimaging. *J. Am. Chem. Soc.* **2013**, *135*, 18–21.

64. Yang, S.; Gong, Y.; Zhang, J.; Zhan, L.; Ma, L.; Fang, Z.; Vajtai, R.; Wang, X.; Ajayan, P.M. Exfoliated Graphitic Carbon Nitride Nanosheets as Efficient Catalysts for Hydrogen Evolution under Visible Light. *Adv. Mater.* **2013**, *25*, 2452–2456.

65. Pan, C.; Xu, J.; Wang, Y.; Li, D.; Zhu, Y. Dramatic Activity of $C_3N_4/BiPO_4$ Photocatalyst with Core/Shell Structure Formed by Self-Assembly. *Adv. Funct. Mater.* **2012**, *22*, 1518–1524.

66. Tian, J.; Zhao, Z.; Kumar, A.; Boughton, R.I.; Liu, H. Recent progress in design, synthesis, and applications of one-dimensional TiO_2 nanostructured surface heterostructures: A review. *Chem. Soc. Rev.* **2014**, *43*, 6920–6937.

67. Weng, B.; Liu, S.; Tang, Z.-R.; Xu, Y.-J. One-dimensional nanostructure based materials for versatile photocatalytic applications. *RSC Adv.* **2014**, *4*, 12685–12700.

68. Bai, X.; Wang, L.; Zong, R.; Zhu, Y. Photocatalytic Activity Enhanced via g-C_3N_4 Nanoplates to Nanorods. *J. Phys. Chem. C* **2013**, *117*, 9952–9961.

69. Zhang, Z.; Leinenweber, K.; Bauer, M.; Garvie, L.A.J.; McMillan, P.F.; Wolf, G.H. High-Pressure Bulk Synthesis of Crystalline $C_6N_9H_3 \cdot HCl$: A Novel C_3N_4 Graphitic Derivative. *J. Am. Chem. Soc.* **2001**, *123*, 7788–7796.

70. Liu, J.; Huang, J.; Zhou, H.; Antonietti, M. Uniform Graphitic Carbon Nitride Nanorod for Efficient Photocatalytic Hydrogen Evolution and Sustained Photoenzymatic Catalysis. *ACS Appl. Mater. Interfaces* **2014**, *6*, 8434–8440.

71. Li, X.-H.; Wang, X.; Antonietti, M. Mesoporous g-C_3N_4 nanorods as multifunctional supports of ultrafine metal nanoparticles: Hydrogen generation from water and reduction of nitrophenol with tandem catalysis in one step. *Chem. Sci.* **2012**, *3*, 2170–2174.

72. Zeng, Y.; Liu, X.; Liu, C.; Wang, L.; Xia, Y.; Zhang, S.; Luo, S.; Pei, Y. Scalable one-step production of porous oxygen-doped g-C_3N_4 nanorods with effective electron separation for excellent visible-light photocatalytic activity. *Appl. Catal. B Environ.* **2018**, *224*, 1–9.

73. Tahir, M.; Cao, C.; Mahmood, N.; Butt, F.K.; Mahmood, A.; Idrees, F.; Hussain, S.; Tanveer, M.; Ali, Z.; Aslam, I. Multifunctional g-C_3N_4 Nanofibers: A Template-Free Fabrication and Enhanced Optical, Electrochemical, and Photocatalyst Properties. *ACS Appl. Mater. Interfaces* **2014**, *6*, 1258–1265.

74. Wang, S.; Li, C.; Wang, T.; Zhang, P.; Li, A.; Gong, J. Controllable synthesis of nanotube-type graphitic C_3N_4 and their visible-light photocatalytic and fluorescent properties. *J. Mater. Chem. A* **2014**, *2*, 2885–2890.

75. Tahir, M.; Cao, C.; Butt, F.K.; Idrees, F.; Mahmood, N.; Ali, Z.; Aslam, I.; Tanveer, M.; Rizwan, M.; Mahmood, T. Tubular graphitic-C_3N_4: A prospective material for energy storage and green photocatalysis. *J. Mater. Chem. A* **2013**, *1*, 13949–13955.

76. Zeng, Z.; Li, K.; Yan, L.; Dai, Y.; Guo, H.; Huo, M.; Guo, Y. Fabrication of carbon nitride nanotubes by a simple water-induced morphological transformation process and their efficient visible-light photocatalytic activity. *RSC Adv.* **2014**, *4*, 59513–59518.

77. Yuan, B.; Chu, Z.; Li, G.; Jiang, Z.; Hu, T.; Wang, Q.; Wang, C. Water-soluble ribbon-like graphitic carbon nitride (g-C_3N_4): Green synthesis, self-assembly and unique optical properties. *J. Mater. Chem. C* **2014**, *2*, 8212–8215.

78. Weiss, E.A. Designing the Surfaces of Semiconductor Quantum Dots for Colloidal Photocatalysis. *ACS Energy Lett.* **2017**, *2*, 1005–1013.

79. Fattakhova-Rohlfing, D.; Zaleska, A.; Bein, T. Three-Dimensional Titanium Dioxide Nanomaterials. *Chem. Rev.* **2014**, *114*, 9487–9558.

80. Gu, Q.; Liao, Y.; Yin, L.; Long, J.; Wang, X.; Xue, C. Template-free synthesis of porous graphitic carbon nitride microspheres for enhanced photocatalytic hydrogen generation with high stability. *Appl. Catal. B Environ.* **2015**, *165*, 503–510.

81. Zhang, J.; Zhang, M.; Yang, C.; Wang, X. Nanospherical Carbon Nitride Frameworks with Sharp Edges Accelerating Charge Collection and Separation at a Soft Photocatalytic Interface. *Adv. Mater.* **2014**, *26*, 4121–4126.

82. Cheng, C.; Jinwen, S.; Yuchao, H.; Liejin, G. WO_3/g-C_3N_4 composites: One-pot preparation and enhanced photocatalytic H_2 production under visible-light irradiation. *Nanotechnology* **2017**, *28*, 164002, doi:10.1088/1361-6528/aa651a.

83. Nguyen, C.C.; Vu, N.N.; Do, T.-O. Recent advances in the development of sunlight-driven hollow structure photocatalysts and their applications. *J. Mater. Chem. A* **2015**, *3*, 18345–18359.

84. Sun, J.; Zhang, J.; Zhang, M.; Antonietti, M.; Fu, X.; Wang, X. Bioinspired hollow semiconductor nanospheres as photosynthetic nanoparticles. *Nat. Commun.* **2012**, *3*, 1139, doi:10.1038/ncomms2152.

85. Zheng, D.; Pang, C.; Liu, Y.; Wang, X. Shell-engineering of hollow g-C_3N_4 nanospheres via copolymerization for photocatalytic hydrogen evolution. *Chem. Commun.* **2015**, *51*, 9706–9709.

86. Jun, Y.-S.; Lee, E.Z.; Wang, X.; Hong, W.H.; Stucky, G.D.; Thomas, A. From Melamine-Cyanuric Acid Supramolecular Aggregates to Carbon Nitride Hollow Spheres. *Adv. Funct. Mater.* **2013**, *23*, 3661–3667.

87. Hong, J.; Yin, S.; Pan, Y.; Han, J.; Zhou, T.; Xu, R. Porous carbon nitride nanosheets for enhanced photocatalytic activities. *Nanoscale* **2014**, *6*, 14984–14990.

88. Han, Q.; Wang, B.; Gao, J.; Cheng, Z.; Zhao, Y.; Zhang, Z.; Qu, L. Atomically Thin Mesoporous Nanomesh of Graphitic C_3N_4 for High-Efficiency Photocatalytic Hydrogen Evolution. *ACS Nano* **2016**, *10*, 2745–2751.

89. Lang, X.; Chen, X.; Zhao, J. Heterogeneous visible light photocatalysis for selective organic transformations. *Chem. Soc. Rev.* **2014**, *43*, 473–486.

90. Zhang, J.; Chen, Y.; Wang, X. Two-dimensional covalent carbon nitride nanosheets: Synthesis, functionalization, and applications. *Energy Environ. Sci.* **2015**, *8*, 3092–3108.

91. Cao, S.; Yu, J. g-C_3N_4-Based Photocatalysts for Hydrogen Generation. *J. Phys. Chem. Lett.* **2014**, *5*, 2101–2107.

92. Ye, S.; Wang, R.; Wu, M.-Z.; Yuan, Y.-P. A review on g-C_3N_4 for photocatalytic water splitting and CO_2 reduction. *Appl. Surf. Sci.* **2015**, *358*, 15–27.

93. Zheng, Y.; Liu, J.; Liang, J.; Jaroniec, M.; Qiao, S.Z. Graphitic carbon nitride materials: Controllable synthesis and applications in fuel cells and photocatalysis. *Energy Environ. Sci.* **2012**, *5*, 6717–6731.

94. Maeda, K. Photocatalytic water splitting using semiconductor particles: History and recent developments. *J. Photochem. Photobiol. C Photochem. Rev.* **2011**, *12*, 237–268.

95. Ahmad, H.; Kamarudin, S.K.; Minggu, L.J.; Kassim, M. Hydrogen from photo-catalytic water splitting process: A review. *Renew. Sustain. Energy Rev.* **2015**, *43*, 599–610.

96. Xu, J.; Zhang, L.; Shi, R.; Zhu, Y. Chemical exfoliation of graphitic carbon nitride for efficient heterogeneous photocatalysis. *J. Mater. Chem. A* **2013**, *1*, 14766–14772.

97. Bandyopadhyay, A.; Ghosh, D.; Kaley, N.M.; Pati, S.K. Photocatalytic Activity of g-C_3N_4 Quantum Dots in Visible Light: Effect of Physicochemical Modifications. *J. Phys. Chem. C* **2017**, *121*, 1982–1989.

98. Ran, J.; Ma, T.Y.; Gao, G.; Du, X.-W.; Qiao, S.Z. Porous P-doped graphitic carbon nitride nanosheets for synergistically enhanced visible-light photocatalytic H_2 production. *Energy Environ. Sci.* **2015**, *8*, 3708–3717.

99. Zheng, D.; Zhang, G.; Hou, Y.; Wang, X. Layering MoS_2 on soft hollow g-C_3N_4 nanostructures for photocatalytic hydrogen evolution. *Appl. Catal. A Gen.* **2016**, *521*, 2–8.

100. Di, Y.; Wang, X.; Thomas, A.; Antonietti, M. Making Metal Carbon Nitride Heterojunctions for Improved Photocatalytic Hydrogen Evolution with Visible Light. *ChemCatChem* **2010**, *2*, 834–838.

101. Ou, M.; Wan, S.; Zhong, Q.; Zhang, S.; Wang, Y. Single Pt atoms deposition on g-C_3N_4 nanosheets for photocatalytic H_2 evolution or NO oxidation under visible light. *Int. J. Hydrogen Energy* **2017**, *42*, 27043–27054.

102. Wang, J.; Cong, J.; Xu, H.; Wang, J.; Liu, H.; Liang, M.; Gao, J.; Ni, Q.; Yao, J. Facile Gel-Based Morphological Control of Ag/g-C_3N_4 Porous Nanofibers for Photocatalytic Hydrogen Generation. *ACS Sustain. Chem. Eng.* **2017**, *5*, 10633–10639.

103. Shen, L.; Xing, Z.; Zou, J.; Li, Z.; Wu, X.; Zhang, Y.; Zhu, Q.; Yang, S.; Zhou, W. Black TiO_2 nanobelts/g-C_3N_4 nanosheets Laminated Heterojunctions with Efficient Visible-Light-Driven Photocatalytic Performance. *Sci. Rep.* **2017**, *7*, 41978, doi:10.1038/srep41978.

104. Zhang, J.; Wang, Y.; Jin, J.; Zhang, J.; Lin, Z.; Huang, F.; Yu, J. Efficient Visible-Light Photocatalytic Hydrogen Evolution and Enhanced Photostability of Core/Shell CdS/g-C_3N_4 Nanowires. *ACS Appl. Mater. Interfaces* **2013**, *5*, 10317–10324.

105. Zhang, Q.; Deng, J.; Xu, Z.; Chaker, M.; Ma, D. High-Efficiency Broadband C_3N_4 Photocatalysts: Synergistic Effects from Upconversion and Plasmons. *ACS Catal.* **2017**, *7*, 6225–6234.

106. Ge, L.; Zuo, F.; Liu, J.; Ma, Q.; Wang, C.; Sun, D.; Bartels, L.; Feng, P. Synthesis and Efficient Visible Light Photocatalytic Hydrogen Evolution of Polymeric g-C_3N_4 Coupled with CdS Quantum Dots. *J. Phys. Chem. C* **2012**, *116*, 13708–13714.

107. Xiang, Q.; Yu, J.; Jaroniec, M. Preparation and Enhanced Visible-Light Photocatalytic H_2-Production Activity of Graphene/C_3N_4 Composites. *J. Phys. Chem. C* **2011**, *115*, 7355–7363.

108. Sun, Z.; Zhu, M.; Fujitsuka, M.; Wang, A.; Shi, C.; Majima, T. Phase Effect of Ni_xP_y Hybridized with g-C_3N_4 for Photocatalytic Hydrogen Generation. *ACS Appl. Mater. Interfaces* **2017**, *9*, 30583–30590.

109. Fang, L.J.; Li, Y.H.; Liu, P.F.; Wang, D.P.; Zeng, H.D.; Wang, X.L.; Yang, H.G. Facile Fabrication of Large-Aspect-Ratio g-C_3N_4 Nanosheets for Enhanced Photocatalytic Hydrogen Evolution. *ACS Sustain. Chem. Eng.* **2017**, *5*, 2039–2043.

110. Naseri, A.; Samadi, M.; Pourjavadi, A.; Moshfegh, A.Z.; Ramakrishna, S. Graphitic carbon nitride (g-C₃N₄)-based photocatalysts for solar hydrogen generation: Recent advances and future development directions. *J. Mater. Chem. A* **2017**, *5*, 23406–23433.

111. Lu, D.; Wang, H.; Zhao, X.; Kondamareddy, K.K.; Ding, J.; Li, C.; Fang, P. Highly Efficient Visible-Light-Induced Photoactivity of Z-Scheme g-C₃N₄/Ag/MoS₂ Ternary Photocatalysts for Organic Pollutant Degradation and Production of Hydrogen. *ACS Sustain. Chem. Eng.* **2017**, *5*, 1436–1445.

112. Xu, D.; Hai, Y.; Zhang, X.; Zhang, S.; He, R. Bi₂O₃ cocatalyst improving photocatalytic hydrogen evolution performance of TiO₂. *Appl. Surf. Sci.* **2017**, *400*, 530–536.

113. Zeng, D.; Ong, W.-J.; Zheng, H.; Wu, M.; Chen, Y.; Peng, D.-L.; Han, M.-Y. Ni₁₂P₅ nanoparticles embedded into porous g-C₃N₄ nanosheets as a noble-metal-free hetero-structure photocatalyst for efficient H₂ production under visible light. *J. Mater. Chem. A* **2017**, *5*, 16171–16178.

114. Mao, Z.; Chen, J.; Yang, Y.; Wang, D.; Bie, L.; Fahlman, B.D. Novel g-C₃N₄/CoO Nanocomposites with Significantly Enhanced Visible-Light Photocatalytic Activity for H₂ Evolution. *ACS Appl. Mater. Interfaces* **2017**, *9*, 12427–12435.

115. Yu, W.; Chen, J.; Shang, T.; Chen, L.; Gu, L.; Peng, T. Direct Z-scheme g-C₃N₄/WO₃ photocatalyst with atomically defined junction for H₂ production. *Appl. Catal. B Environ.* **2017**, *219*, 693–704.

116. Wen, J.; Xie, J.; Zhang, H.; Zhang, A.; Liu, Y.; Chen, X.; Li, X. Constructing Multifunctional Metallic Ni Interface Layers in the g-C₃N₄ Nanosheets/Amorphous NiS Heterojunctions for Efficient Photocatalytic H₂ Generation. *ACS Appl. Mater. Interfaces* **2017**, *9*, 14031–14042.

117. Zhao, H.; Wang, J.; Dong, Y.; Jiang, P. Noble-Metal-Free Iron Phosphide Cocatalyst Loaded Graphitic Carbon Nitride as an Efficient and Robust Photocatalyst for Hydrogen Evolution under Visible Light Irradiation. *ACS Sustain. Chem. Eng.* **2017**, *5*, 8053–8060.

118. Barrio, J.; Lin, L.; Wang, X.; Shalom, M. Design of a Unique Energy-Band Structure and Morphology in a Carbon Nitride Photocatalyst for Improved Charge Separation and Hydrogen Production. *ACS Sustain. Chem. Eng.* **2017**, doi:10.1021/acssuschemeng.7b02807.

119. Jin, A.; Jia, Y.; Chen, C.; Liu, X.; Jiang, J.; Chen, X.; Zhang, F. Efficient Photocatalytic Hydrogen Evolution on Band Structure Tuned Polytriazine/Heptazine Based Carbon Nitride Heterojunctions with Ordered Needle-like Morphology Achieved by an In Situ Molten Salt Method. *J. Phys. Chem. C* **2017**, *121*, 21497–21509.

120. Pramoda, K.; Gupta, U.; Chhetri, M.; Bandyopadhyay, A.; Pati, S.K.; Rao, C.N.R. Nanocomposites of C₃N₄ with Layers of MoS₂ and Nitrogenated RGO, Obtained by Covalent Cross-Linking: Synthesis, Characterization, and HER Activity. *ACS Appl. Mater. Interfaces* **2017**, *9*, 10664–10672.

121. Masih, D.; Ma, Y.; Rohani, S. Graphitic C₃N₄ C₃N₄ based noble-metal-free photocatalyst systems: A review. *Appl. Catal. B Environ.* **2017**, *206*, 556–588.

122. Tonda, S.; Kumar, S.; Gawli, Y.; Bhardwaj, M.; Ogale, S. g-C₃N₄ (2D)/CdS (1D)/rGO (2D) dual-interface nano-composite for excellent and stable visible light photocatalytic hydrogen generation. *Int. J. Hydrog. Energy* **2017**, *42*, 5971–5984.

123. Yuan, Y.-P.; Cao, S.-W.; Liao, Y.-S.; Yin, L.-S.; Xue, C. Red phosphor/g-C₃N₄ heterojunction with enhanced photocatalytic activities for solar fuels production. *Appl. Catal. B Environ.* **2013**, *140–141*, 164–168.

124. He, F.; Chen, G.; Yu, Y.; Hao, S.; Zhou, Y.; Zheng, Y. Facile Approach to Synthesize g-PAN/g-C₃N₄ Composites with Enhanced Photocatalytic H₂ Evolution Activity. *ACS Appl. Mater. Interfaces* **2014**, *6*, 7171–7179.

125. Zhang, Z.; Liu, K.; Feng, Z.; Bao, Y.; Dong, B. Hierarchical Sheet-on-Sheet ZnIn₂S₄/g-C₃N₄ Heterostructure with Highly Efficient Photocatalytic H₂ production Based on Photoinduced Interfacial Charge Transfer. *Sci. Rep.* **2016**, *6*, 19221, doi:10.1038/srep19221.

126. Qingqing, L.; Wenli, H.; Penghui, Z.; Tianlong, H.; Shuxian, Z.; Lining, Y.; Jianrong, C.; Song, B. Twin defects engineered Pd cocatalyst on C₃N₄ nanosheets for enhanced photocatalytic performance in CO₂ reduction reaction. *Nanotechnology* **2017**, *28*, 484003, doi:10.1088/1361-6528/aa9137.

127. Gu, W.; Lu, F.; Wang, C.; Kuga, S.; Wu, L.; Huang, Y.; Wu, M. Face-to-Face Interfacial Assembly of Ultrathin g-C₃N₄ and Anatase TiO₂ Nanosheets for Enhanced Solar Photocatalytic Activity. *ACS Appl. Mater. Interfaces* **2017**, *9*, 28674–28684.

128. Hafeez, H.Y.; Lakhera, S.K.; Bellamkonda, S.; Rao, G.R.; Shankar, M.V.; Bahnemann, D.W.; Neppolian, B. Construction of ternary hybrid layered reduced graphene oxide supported g-C$_3$N$_4$-TiO$_2$ nanocomposite and its photocatalytic hydrogen production activity. *Int. J. Hydrogen Energy* **2017**, doi:10.1016/j.ijhydene.2017.09.048.

129. Guo, F.; Shi, W.; Wang, H.; Han, M.; Li, H.; Huang, H.; Liu, Y.; Kang, Z. Facile fabrication of a CoO/g-C$_3$N$_4$ p-n heterojunction with enhanced photocatalytic activity and stability for tetracycline degradation under visible light. *Catal. Sci. Technol.* **2017**, *7*, 3325–3331.

130. Ye, R.; Fang, H.; Zheng, Y.-Z.; Li, N.; Wang, Y.; Tao, X. Fabrication of CoTiO$_3$/g-C$_3$N$_4$ Hybrid Photocatalysts with Enhanced H$_2$ Evolution: Z-Scheme Photocatalytic Mechanism Insight. *ACS Appl. Mater. Interfaces* **2016**, *8*, 13879–13889.

131. Xu, L.; Huang, W.-Q.; Wang, L.-L.; Tian, Z.-A.; Hu, W.; Ma, Y.; Wang, X.; Pan, A.; Huang, G.-F. Insights into Enhanced Visible-Light Photocatalytic Hydrogen Evolution of g-C$_3$N$_4$ and Highly Reduced Graphene Oxide Composite: The Role of Oxygen. *Chem. Mater.* **2015**, *27*, 1612–1621.

132. Yuan, Y.-P.; Xu, W.-T.; Yin, L.-S.; Cao, S.-W.; Liao, Y.-S.; Tng, Y.-Q.; Xue, C. Large impact of heating time on physical properties and photocatalytic H$_2$ production of g-C$_3$N$_4$ nanosheets synthesized through urea polymerization in Ar atmosphere. *Int. J. Hydrogen Energy* **2013**, *38*, 13159–13163.

133. Tong, J.; Zhang, L.; Li, F.; Li, M.; Cao, S. An efficient top-down approach for the fabrication of large-aspect-ratio g-C$_3$N$_4$ nanosheets with enhanced photocatalytic activities. *Phys. Chem. Chem. Phys.* **2015**, *17*, 23532–23537.

134. Martin, D.J.; Qiu, K.; Shevlin, S.A.; Handoko, A.D.; Chen, X.; Guo, Z.; Tang, J. Highly Efficient Photocatalytic H$_2$ Evolution from Water using Visible Light and Structure-Controlled Graphitic Carbon Nitride. *Angew. Chem. Int. Ed.* **2014**, *53*, 9240–9245.

135. Gu, Q.; Gao, Z.; Zhao, H.; Lou, Z.; Liao, Y.; Xue, C. Temperature-controlled morphology evolution of graphitic carbon nitride nanostructures and their photocatalytic activities under visible light. *RSC Adv.* **2015**, *5*, 49317–49325.

136. Li, X.; Masters, A.F.; Maschmeyer, T. Photocatalytic Hydrogen Evolution from Silica-Templated Polymeric Graphitic Carbon Nitride—Is the Surface Area Important? *ChemCatChem* **2015**, *7*, 121–126.

137. Liang, Q.; Li, Z.; Yu, X.; Huang, Z.-H.; Kang, F.; Yang, Q.-H. Macroscopic 3D Porous Graphitic Carbon Nitride Monolith for Enhanced Photocatalytic Hydrogen Evolution. *Adv. Mater.* **2015**, *27*, 4634–4639.

138. Han, Q.; Hu, C.; Zhao, F.; Zhang, Z.; Chen, N.; Qu, L. One-step preparation of iodine-doped graphitic carbon nitride nanosheets as efficient photocatalysts for visible light water splitting. *J. Mater. Chem. A* **2015**, *3*, 4612–4619.

139. Zhu, Y.-P.; Ren, T.-Z.; Yuan, Z.-Y. Mesoporous Phosphorus-Doped g-C$_3$N$_4$ Nanostructured Flowers with Superior Photocatalytic Hydrogen Evolution Performance. *ACS Appl. Mater. Interfaces* **2015**, *7*, 16850–16856.

140. Huang, Z.-F.; Song, J.; Pan, L.; Wang, Z.; Zhang, X.; Zou, J.-J.; Mi, W.; Zhang, X.; Wang, L. Carbon nitride with simultaneous porous network and O-doping for efficient solar-energy-driven hydrogen evolution. *Nano Energy* **2015**, *12*, 646–656.

141. Wu, M.; Yan, J.-M.; Tang, X.-N.; Zhao, M.; Jiang, Q. Synthesis of Potassium-Modified Graphitic Carbon Nitride with High Photocatalytic Activity for Hydrogen Evolution. *ChemSusChem* **2014**, *7*, 2654–2658.

142. Han, C.; Wu, L.; Ge, L.; Li, Y.; Zhao, Z. AuPd bimetallic nanoparticles decorated graphitic carbon nitride for highly efficient reduction of water to H$_2$ under visible light irradiation. *Carbon* **2015**, *92*, 31–40.

143. Li, X.; Hartley, G.; Ward, A.J.; Young, P.A.; Masters, A.F.; Maschmeyer, T. Hydrogenated Defects in Graphitic Carbon Nitride Nanosheets for Improved Photocatalytic Hydrogen Evolution. *J. Phys. Chem. C* **2015**, *119*, 14938–14946.

144. Wu, P.; Wang, J.; Zhao, J.; Guo, L.; Osterloh, F.E. High alkalinity boosts visible light driven H$_2$ evolution activity of g-C$_3$N$_4$ in aqueous methanol. *Chem. Commun.* **2014**, *50*, 15521–15524.

145. Wang, Y.; Hong, J.; Zhang, W.; Xu, R. Carbon nitride nanosheets for photocatalytic hydrogen evolution: Remarkably enhanced activity by dye sensitization. *Catal. Sci. Technol.* **2013**, *3*, 1703–1711.

146. Zhang, J.; Zhang, G.; Chen, X.; Lin, S.; Möhlmann, L.; Dołęga, G.; Lipner, G.; Antonietti, M.; Blechert, S.; Wang, X. Co-Monomer Control of Carbon Nitride Semiconductors to Optimize Hydrogen Evolution with Visible Light. *Angew. Chem. Int. Ed.* **2012**, *51*, 3183–3187.

147. Sui, Y.; Liu, J.; Zhang, Y.; Tian, X.; Chen, W. Dispersed conductive polymer nanoparticles on graphitic carbon nitride for enhanced solar-driven hydrogen evolution from pure water. *Nanoscale* **2013**, *5*, 9150–9155.

148. Liu, L.; Qi, Y.; Hu, J.; An, W.; Lin, S.; Liang, Y.; Cui, W. Stable Cu2O@g-C3N4 core@shell nanostructures: Efficient visible-light photocatalytic hydrogen evolution. *Mater. Lett.* **2015**, *158*, 278–281.

149. Zhang, G.; Li, G.; Wang, X. Surface Modification of Carbon Nitride Polymers by Core–Shell Nickel/Nickel Oxide Cocatalysts for Hydrogen Evolution Photocatalysis. *ChemCatChem* **2015**, *7*, 2864–2870.

150. Zhao, H.; Dong, Y.; Jiang, P.; Miao, H.; Wang, G.; Zhang, J. In situ light-assisted preparation of MoS2 on graphitic C3N4 nanosheets for enhanced photocatalytic H2 production from water. *J. Mater. Chem. A* **2015**, *3*, 7375–7381.

151. Cao, S.-W.; Yuan, Y.-P.; Fang, J.; Shahjamali, M.M.; Boey, F.Y.C.; Barber, J.; Joachim Loo, S.C.; Xue, C. In-situ growth of CdS quantum dots on g-C3N4 nanosheets for highly efficient photocatalytic hydrogen generation under visible light irradiation. *Int. J. Hydrogen Energy* **2013**, *38*, 1258–1266.

152. Yuan, J.; Wen, J.; Zhong, Y.; Li, X.; Fang, Y.; Zhang, S.; Liu, W. Enhanced photocatalytic H2 evolution over noble-metal-free NiS cocatalyst modified CdS nanorods/g-C3N4 heterojunctions. *J. Mater. Chem. A* **2015**, *3*, 18244–18255.

153. Jiang, D.; Li, J.; Xing, C.; Zhang, Z.; Meng, S.; Chen, M. Two-Dimensional CaIn2S4/g-C3N4 Heterojunction Nanocomposite with Enhanced Visible-Light Photocatalytic Activities: Interfacial Engineering and Mechanism Insight. *ACS Appl. Mater. Interfaces* **2015**, *7*, 19234–19242.

154. Yuan, J.; Gao, Q.; Li, X.; Liu, Y.; Fang, Y.; Yang, S.; Peng, F.; Zhou, X. Novel 3-D nanoporous graphitic-C3N4 nanosheets with heterostructured modification for efficient visible-light photocatalytic hydrogen production. *RSC Adv.* **2014**, *4*, 52332–52337.

155. Sridharan, K.; Jang, E.; Park, J.H.; Kim, J.-H.; Lee, J.-H.; Park, T.J. Silver Quantum Cluster (Ag9)-Grafted Graphitic Carbon Nitride Nanosheets for Photocatalytic Hydrogen Generation and Dye Degradation. *Chem. Eur. J.* **2015**, *21*, 9126–9132.

156. Li, F.-T.; Liu, S.-J.; Xue, Y.-B.; Wang, X.-J.; Hao, Y.-J.; Zhao, J.; Liu, R.-H.; Zhao, D. Structure Modification Function of g-C3N4 for Al2O3 in the in situ Hydrothermal Process for Enhanced Photocatalytic Activity. *Chem. Eur. J.* **2015**, *21*, 10149–10159.

157. Hou, Y.; Laursen, A.B.; Zhang, J.; Zhang, G.; Zhu, Y.; Wang, X.; Dahl, S.; Chorkendorff, I. Layered Nanojunctions for Hydrogen-Evolution Catalysis. *Angew. Chem. Int. Ed.* **2013**, *52*, 3621–3625.

158. Wu, Z.; Gao, H.; Yan, S.; Zou, Z. Synthesis of carbon black/carbon nitride intercalation compound composite for efficient hydrogen production. *Dalton Trans.* **2014**, *43*, 12013–12017.

159. Wen, J.; Li, X.; Li, H.; Ma, S.; He, K.; Xu, Y.; Fang, Y.; Liu, W.; Gao, Q. Enhanced visible-light H2 evolution of g-C3N4 photocatalysts via the synergetic effect of amorphous NiS and cheap metal-free carbon black nanoparticles as co-catalysts. *Appl. Surf. Sci.* **2015**, *358*, 204–212.

160. Pany, S.; Parida, K.M. A facile in situ approach to fabricate N,S-TiO2/g-C3N4 nanocomposite with excellent activity for visible light induced water splitting for hydrogen evolution. *Phys. Chem. Chem. Phys.* **2015**, *17*, 8070–8077.

161. Chen, J.; Shen, S.; Wu, P.; Guo, L. Nitrogen-doped CeOx nanoparticles modified graphitic carbon nitride for enhanced photocatalytic hydrogen production. *Green Chem.* **2015**, *17*, 509–517.

162. Zhang, Y.; Mao, F.; Yan, H.; Liu, K.; Cao, H.; Wu, J.; Xiao, D. A polymer-metal-polymer-metal heterostructure for enhanced photocatalytic hydrogen production. *J. Mater. Chem. A* **2015**, *3*, 109–115.

163. Kamat, P.V. Meeting the Clean Energy Demand: Nanostructure Architectures for Solar Energy Conversion. *J. Phys. Chem. C* **2007**, *111*, 2834–2860.

164. Kumar, B.; Llorente, M.; Froehlich, J.; Dang, T.; Sathrum, A.; Kubiak, C.P. Photochemical and Photoelectrochemical Reduction of CO2. *Annu. Rev. Phys. Chem.* **2012**, *63*, 541–569.

165. Yu, W.; Xu, D.; Peng, T. Enhanced photocatalytic activity of g-C3N4 for selective CO2 reduction to CH3OH via facile coupling of ZnO: A direct Z-scheme mechanism. *J. Mater. Chem. A* **2015**, *3*, 19936–19947.

166. Kuriki, R.; Sekizawa, K.; Ishitani, O.; Maeda, K. Visible-Light-Driven CO2 Reduction with Carbon Nitride: Enhancing the Activity of Ruthenium Catalysts. *Angew. Chem. Int. Ed.* **2015**, *54*, 2406–2409.

167. Walsh, J.J.; Jiang, C.; Tang, J.; Cowan, A.J. Photochemical CO2 reduction using structurally controlled g-C3N4. *Phys. Chem. Chem. Phys.* **2016**, *18*, 24825–24829.

168. Yu, J.; Wang, K.; Xiao, W.; Cheng, B. Photocatalytic reduction of CO2 into hydrocarbon solar fuels over g-C3N4-Pt nanocomposite photocatalysts. *Phys. Chem. Chem. Phys.* **2014**, *16*, 11492–11501.

169. Gao, G.; Jiao, Y.; Waclawik, E.R.; Du, A. Single Atom (Pd/Pt) Supported on Graphitic Carbon Nitride as an Efficient Photocatalyst for Visible-Light Reduction of Carbon Dioxide. *J. Am. Chem. Soc.* **2016**, *138*, 6292–6297.

170. Wang, K.; Li, Q.; Liu, B.; Cheng, B.; Ho, W.; Yu, J. Sulfur-doped g-C₃N₄ with enhanced photocatalytic CO₂-reduction performance. *Appl. Catal. B Environ.* **2015**, *176–177*, 44–52.

171. Fu, J.; Zhu, B.; Jiang, C.; Cheng, B.; You, W.; Yu, J. Hierarchical Porous O-Doped g-C₃N₄ with Enhanced Photocatalytic CO₂ Reduction Activity. *Small* **2017**, *13*, doi:10.1002/smll.201603938.

172. Mao, J.; Peng, T.; Zhang, X.; Li, K.; Ye, L.; Zan, L. Effect of graphitic carbon nitride microstructures on the activity and selectivity of photocatalytic CO₂ reduction under visible light. *Catal. Sci. Technol.* **2013**, *3*, 1253–1260.

173. Shi, H.; Chen, G.; Zhang, C.; Zou, Z. Polymeric g-C₃N₄ Coupled with NaNbO₃ Nanowires toward Enhanced Photocatalytic Reduction of CO₂ into Renewable Fuel. *ACS Catal.* **2014**, *4*, 3637–3643.

174. Li, H.; Gan, S.; Wang, H.; Han, D.; Niu, L. Intercorrelated Superhybrid of AgBr Supported on Graphitic-C₃N₄-Decorated Nitrogen-Doped Graphene: High Engineering Photocatalytic Activities for Water Purification and CO₂ Reduction. *Adv. Mater.* **2015**, *27*, 6906–6913.

175. He, Y.; Zhang, L.; Teng, B.; Fan, M. New Application of Z-Scheme Ag₃PO₄/g-C₃N₄ Composite in Converting CO₂ to Fuel. *Environ. Sci. Technol.* **2015**, *49*, 649–656.

176. Lin, J.; Pan, Z.; Wang, X. Photochemical Reduction of CO₂ by Graphitic Carbon Nitride Polymers. *ACS Sustain. Chem. Eng.* **2014**, *2*, 353–358.

177. Xia, P.; Zhu, B.; Yu, J.; Cao, S.; Jaroniec, M. Ultra-thin nanosheet assemblies of graphitic carbon nitride for enhanced photocatalytic CO₂ reduction. *J. Mater. Chem. A* **2017**, *5*, 3230–3238.

178. Han, Z.; Yu, Y.; Zheng, W.; Cao, Y. The band structure and photocatalytic mechanism for a CeO₂-modified C₃N₄ photocatalyst. *New J. Chem.* **2017**, *41*, 9724–9730.

179. Wang, M.; Shen, M.; Zhang, L.; Tian, J.; Jin, X.; Zhou, Y.; Shi, J. 2D-2D MnO₂/g-C₃N₄ heterojunction photocatalyst: In-situ synthesis and enhanced CO₂ reduction activity. *Carbon* **2017**, *120*, 23–31.

180. Di, T.; Zhu, B.; Cheng, B.; Yu, J.; Xu, J. A direct Z-scheme g-C₃N₄/SnS₂ photocatalyst with superior visible-light CO₂ reduction performance. *J. Catal.* **2017**, *352*, 532–541.

181. Feng, Z.; Zeng, L.; Chen, Y.; Ma, Y.; Zhao, C.; Jin, R.; Lu, Y.; Wu, Y.; He, Y. In situ preparation of Z-scheme MoO₃/g-C₃N₄ composite with high performance in photocatalytic CO₂ reduction and RhB degradation. *J. Mater. Res.* **2017**, *32*, 3660–3668.

182. Adekoya, D.O.; Tahir, M.; Amin, N.A.S. g-C₃N₄/(Cu/TiO₂) nanocomposite for enhanced photoreduction of CO₂ to CH₃OH and HCOOH under UV/visible light. *J. CO₂ Util.* **2017**, *18*, 261–274.

183. Li, H.; Gao, Y.; Wu, X.; Lee, P.-H.; Shih, K. Fabrication of Heterostructured g-C₃N₄/Ag-TiO₂ Hybrid Photocatalyst with Enhanced Performance in Photocatalytic Conversion of CO₂ Under Simulated Sunlight Irradiation. *Appl. Surf. Sci.* **2017**, *402*, 198–207.

184. Huang, Y.; Wang, Y.; Bi, Y.; Jin, J.; Ehsan, M.F.; Fu, M.; He, T. Preparation of 2D hydroxyl-rich carbon nitride nanosheets for photocatalytic reduction of CO₂. *RSC Adv.* **2015**, *5*, 33254–33261.

185. Niu, P.; Yang, Y.; Yu, J.C.; Liu, G.; Cheng, H.-M. Switching the selectivity of the photoreduction reaction of carbon dioxide by controlling the band structure of a g-C₃N₄ photocatalyst. *Chem. Commun.* **2014**, *50*, 10837–10840.

186. Wang, H.; Sun, Z.; Li, Q.; Tang, Q.; Wu, Z. Surprisingly advanced CO₂ photocatalytic conversion over thiourea derived g-C₃N₄ with water vapor while introducing 200–420 nm UV light. *J. CO₂ Util.* **2016**, *14*, 143–151.

187. Ni, Z.; Dong, F.; Huang, H.; Zhang, Y. New insights into how Pd nanoparticles influence the photocatalytic oxidation and reduction ability of g-C₃N₄ nanosheets. *Catal. Sci. Technol.* **2016**, *6*, 6448–6458.

188. Ong, W.-J.; Tan, L.-L.; Chai, S.-P.; Yong, S.-T. Heterojunction engineering of graphitic carbon nitride (g-C₃N₄) via Pt loading with improved daylight-induced photocatalytic reduction of carbon dioxide to methane. *Dalton Trans.* **2015**, *44*, 1249–1257.

189. Huang, Q.; Yu, J.; Cao, S.; Cui, C.; Cheng, B. Efficient photocatalytic reduction of CO₂ by amine-functionalized g-C₃N₄. *Appl. Surf. Sci.* **2015**, *358*, 350–355.

190. Raziq, F.; Qu, Y.; Humayun, M.; Zada, A.; Yu, H.; Jing, L. Synthesis of SnO₂/B-P codoped g-C₃N₄ nanocomposites as efficient cocatalyst-free visible-light photocatalysts for CO₂ conversion and pollutant degradation. *Appl. Catal. B Environ.* **2017**, *201*, 486–494.

191. Maeda, K.; Kuriki, R.; Zhang, M.; Wang, X.; Ishitani, O. The effect of the pore-wall structure of carbon nitride on photocatalytic CO₂ reduction under visible light. *J. Mater. Chem. A* **2014**, *2*, 15146–15151.

192. Ong, W.-J.; Putri, L.K.; Tan, L.-L.; Chai, S.-P.; Yong, S.-T. Heterostructured AgX/g-C₃N₄ (X = Cl and Br) nanocomposites via a sonication-assisted deposition-precipitation approach: Emerging role of halide ions in the synergistic photocatalytic reduction of carbon dioxide. *Appl. Catal. B Environ.* **2016**, *180*, 530–543.

193. Zhang, X.; Wang, L.; Du, Q.; Wang, Z.; Ma, S.; Yu, M. Photocatalytic CO_2 reduction over B_4C/C_3N_4 with internal electric field under visible light irradiation. *J. Colloid Interface Sci.* **2016**, *464*, 89–95.

194. Wang, J.-C.; Yao, H.-C.; Fan, Z.-Y.; Zhang, L.; Wang, J.-S.; Zang, S.-Q.; Li, Z.-J. Indirect Z-Scheme BiOI/g-C_3N_4 Photocatalysts with Enhanced Photoreduction CO_2 Activity under Visible Light Irradiation. *ACS Appl. Mater. Interfaces* **2016**, *8*, 3765–3775.

195. Wang, Y.; Bai, X.; Qin, H.; Wang, F.; Li, Y.; Li, X.; Kang, S.; Zuo, Y.; Cui, L. Facile One-Step Synthesis of Hybrid Graphitic Carbon Nitride and Carbon Composites as High-Performance Catalysts for CO_2 Photocatalytic Conversion. *ACS Appl. Mater. Interfaces* **2016**, *8*, 17212–17219.

196. Li, M.; Zhang, L.; Wu, M.; Du, Y.; Fan, X.; Wang, M.; Zhang, L.; Kong, Q.; Shi, J. Mesostructured CeO_2/g-C_3N_4 nanocomposites: Remarkably enhanced photocatalytic activity for CO_2 reduction by mutual component activations. *Nano Energy* **2016**, *19*, 145–155.

197. Ong, W.-J.; Tan, L.-L.; Chai, S.-P.; Yong, S.-T. Graphene oxide as a structure-directing agent for the two-dimensional interface engineering of sandwich-like graphene-g-C_3N_4 hybrid nanostructures with enhanced visible-light photoreduction of CO_2 to methane. *Chem. Commun.* **2015**, *51*, 858–861.

198. Zhou, S.; Liu, Y.; Li, J.; Wang, Y.; Jiang, G.; Zhao, Z.; Wang, D.; Duan, A.; Liu, J.; Wei, Y. Facile in situ synthesis of graphitic carbon nitride (g-C_3N_4)-N-TiO_2 heterojunction as an efficient photocatalyst for the selective photoreduction of CO_2 to CO. *Appl. Catal. B Environ.* **2014**, *158–159*, 20–29.

199. Ong, W.-J.; Tan, L.-L.; Chai, S.-P.; Yong, S.-T.; Mohamed, A.R. Surface charge modification via protonation of graphitic carbon nitride (g-C_3N_4) for electrostatic self-assembly construction of 2D/2D reduced graphene oxide (rGO)/g-C_3N_4 nanostructures toward enhanced photocatalytic reduction of carbon dioxide to methane. *Nano Energy* **2015**, *13*, 757–770.

200. Kuriki, R.; Ishitani, O.; Maeda, K. Unique Solvent Effects on Visible-Light CO_2 Reduction over Ruthenium(II)-Complex/Carbon Nitride Hybrid Photocatalysts. *ACS Appl. Mater. Interfaces* **2016**, *8*, 6011–6018.

201. Maeda, K.; Sekizawa, K.; Ishitani, O. A polymeric-semiconductor-metal-complex hybrid photocatalyst for visible-light CO_2 reduction. *Chem. Commun.* **2013**, *49*, 10127–10129.

202. He, Y.; Zhang, L.; Fan, M.; Wang, X.; Walbridge, M.L.; Nong, Q.; Wu, Y.; Zhao, L. Z-scheme SnO_{2-x}/g-C_3N_4 composite as an efficient photocatalyst for dye degradation and photocatalytic CO_2 reduction. *Sol. Energy Mater. Sol. Cells* **2015**, *137*, 175–184.

203. Li, K.; Peng, B.; Jin, J.; Zan, L.; Peng, T. Carbon nitride nanodots decorated brookite TiO_2 quasi nanocubes for enhanced activity and selectivity of visible-light-driven CO_2 reduction. *Appl. Catal. B Environ.* **2017**, *203*, 910–916.

204. Reli, M.; Huo, P.; Šihor, M.; Ambrožová, N.; Troppová, I.; Matějová, L.; Lang, J.; Svoboda, L.; Kuśtrowski, P.; Ritz, M.; et al. Novel TiO_2/C_3N_4 Photocatalysts for Photocatalytic Reduction of CO_2 and for Photocatalytic Decomposition of N_2O. *J. Phys. Chem. A* **2016**, *120*, 8564–8573.

205. Ohno, T.; Murakami, N.; Koyanagi, T.; Yang, Y. Photocatalytic reduction of CO_2 over a hybrid photocatalyst composed of WO_3 and graphitic carbon nitride (g-C_3N_4) under visible light. *J. CO_2 Util.* **2014**, *6*, 17–25.

206. He, Y.; Wang, Y.; Zhang, L.; Teng, B.; Fan, M. High-efficiency conversion of CO_2 to fuel over ZnO/g-C_3N_4 photocatalyst. *Appl. Catal. B Environ.* **2015**, *168–169*, 1–8.

207. Zhao, G.; Pang, H.; Liu, G.; Li, P.; Liu, H.; Zhang, H.; Shi, L.; Ye, J. Co-porphyrin/carbon nitride hybrids for improved photocatalytic CO_2 reduction under visible light. *Appl. Catal. B Environ.* **2017**, *200*, 141–149.

208. Li, M.; Zhang, L.; Fan, X.; Zhou, Y.; Wu, M.; Shi, J. Highly selective CO_2 photoreduction to CO over g-C_3N_4/Bi_2WO_6 composites under visible light. *J. Mater. Chem. A* **2015**, *3*, 5189–5196.

209. Bai, Y.; Ye, L.; Wang, L.; Shi, X.; Wang, P.; Bai, W.; Wong, P.K. g-$C_3N_4/Bi_4O_5I_2$ heterojunction with I_3^-/I^- redox mediator for enhanced photocatalytic CO_2 conversion. *Appl. Catal. B Environ.* **2016**, *194*, 98–104.

210. Li, M.; Zhang, L.; Fan, X.; Wu, M.; Wang, M.; Cheng, R.; Zhang, L.; Yao, H.; Shi, J. Core-shell $LaPO_4$/g-C_3N_4 nanowires for highly active and selective CO_2 reduction. *Appl. Catal. B Environ.* **2017**, *201*, 629–635.

211. Liu, H.; Zhang, Z.; Meng, J.; Zhang, J. Novel visible-light-driven $CdIn_2S_4$/mesoporous g-C_3N_4 hybrids for efficient photocatalytic reduction of CO_2 to methanol. *Mol. Catal.* **2017**, *430*, 9–19.

212. Ye, L.; Wu, D.; Chu, K.H.; Wang, B.; Xie, H.; Yip, H.Y.; Wong, P.K. Phosphorylation of g-C_3N_4 for enhanced photocatalytic CO_2 reduction. *Chem. Eng. J.* **2016**, *304*, 376–383.

213. Shi, H.; Zhang, C.; Zhou, C.; Chen, G. Conversion of CO_2 into renewable fuel over Pt-g-C_3N_4/$KNbO_3$ composite photocatalyst. *RSC Adv.* **2015**, *5*, 93615–93622.

214. Bai, Y.; Chen, T.; Wang, P.; Wang, L.; Ye, L.; Shi, X.; Bai, W. Size-dependent role of gold in g-C_3N_4/BiOBr/Au system for photocatalytic CO_2 reduction and dye degradation. *Sol. Energy Mater. Sol. Cells* **2016**, *157*, 406–414.

215. Richardson, S.D.; Ternes, T.A. Water Analysis: Emerging Contaminants and Current Issues. *Anal. Chem.* **2014**, *86*, 2813–2848.

216. Bolong, N.; Ismail, A.F.; Salim, M.R.; Matsuura, T. A review of the effects of emerging contaminants in wastewater and options for their removal. *Desalination* **2009**, *239*, 229–246.

217. Lofrano, G.; Meriç, S.; Zengin, G.E.; Orhon, D. Chemical and biological treatment technologies for leather tannery chemicals and wastewaters: A review. *Sci. Total Environ.* **2013**, *461–462*, 265–281.

218. Karthikeyan, S.; Dionysiou, D.D.; Lee, A.F.; Suvitha, S.; Maharaja, P.; Wilson, K.; Sekaran, G. Hydroxyl radical generation by cactus-like copper oxide nanoporous carbon catalysts for microcystin-LR environmental remediation. *Catal. Sci. Technol.* **2016**, *6*, 530–544.

219. Karthikeyan, S.; Pachamuthu, M.P.; Isaacs, M.A.; Kumar, S.; Lee, A.F.; Sekaran, G. Cu and Fe oxides dispersed on SBA-15: A Fenton type bimetallic catalyst for N,N-diethyl-p-phenyl diamine degradation. *Appl. Catal. B Environ.* **2016**, *199*, 323–330.

220. Binas, V.; Venieri, D.; Kotzias, D.; Kiriakidis, G. Modified TiO_2 based photocatalysts for improved air and health quality. *J. Mater.* **2017**, *3*, 3–16.

221. Ollis, D.F.; Pelizzetti, E.; Serpone, N. Photocatalyzed destruction of water contaminants. *Environ. Sci. Technol.* **1991**, *25*, 1522–1529.

222. Hoffmann, M.R.; Martin, S.T.; Choi, W.; Bahnemann, D.W. Environmental Applications of Semiconductor Photocatalysis. *Chem. Rev.* **1995**, *95*, 69–96.

223. Jo, W.-K.; Kumar, S.; Isaacs, M.A.; Lee, A.F.; Karthikeyan, S. Cobalt promoted TiO_2/GO for the photocatalytic degradation of oxytetracycline and Congo Red. *Appl. Catal. B Environ.* **2017**, *201*, 159–168.

224. Li, Z.; Kong, C.; Lu, G. Visible Photocatalytic Water Splitting and Photocatalytic Two-Electron Oxygen Formation over Cu- and Fe-Doped $g-C_3N_4$. *J. Phys. Chem. C* **2016**, *120*, 56–63.

225. Tonda, S.; Kumar, S.; Kandula, S.; Shanker, V. Fe-doped and -mediated graphitic carbon nitride nanosheets for enhanced photocatalytic performance under natural sunlight. *J. Mater. Chem. A* **2014**, *2*, 6772–6780.

226. Gao, J.; Wang, J.; Qian, X.; Dong, Y.; Xu, H.; Song, R.; Yan, C.; Zhu, H.; Zhong, Q.; Qian, G.; et al. One-pot synthesis of copper-doped graphitic carbon nitride nanosheet by heating Cu–melamine supramolecular network and its enhanced visible-light-driven photocatalysis. *J. Solid State Chem.* **2015**, *228*, 60–64.

227. Yan, S.C.; Li, Z.S.; Zou, Z.G. Photodegradation of Rhodamine B and Methyl Orange over Boron-Doped $g-C_3N_4$ under Visible Light Irradiation. *Langmuir* **2010**, *26*, 3894–3901.

228. Liu, G.; Niu, P.; Sun, C.; Smith, S.C.; Chen, Z.; Lu, G.Q.; Cheng, H.-M. Unique Electronic Structure Induced High Photoreactivity of Sulfur-Doped Graphitic C_3N_4. *J. Am. Chem. Soc.* **2010**, *132*, 11642–11648.

229. Li, J.; Shen, B.; Hong, Z.; Lin, B.; Gao, B.; Chen, Y. A facile approach to synthesize novel oxygen-doped $g-C_3N_4$ with superior visible-light photoreactivity. *Chem. Commun.* **2012**, *48*, 12017–12019.

230. Ma, X.; Lv, Y.; Xu, J.; Liu, Y.; Zhang, R.; Zhu, Y. A Strategy of Enhancing the Photoactivity of $g-C_3N_4$ via Doping of Nonmetal Elements: A First-Principles Study. *J. Phys. Chem. C* **2012**, *116*, 23485–23493.

231. Panneri, S.; Ganguly, P.; Mohan, M.; Nair, B.N.; Mohamed, A.A.P.; Warrier, K.G.; Hareesh, U.S. Photoregenerable, Bifunctional Granules of Carbon-Doped $g-C_3N_4$ as Adsorptive Photocatalyst for the Efficient Removal of Tetracycline Antibiotic. *ACS Sustain. Chem. Eng.* **2017**, *5*, 1610–1618.

232. Hu, S.; Ma, L.; You, J.; Li, F.; Fan, Z.; Lu, G.; Liu, D.; Gui, J. Enhanced visible light photocatalytic performance of $g-C_3N_4$ photocatalysts co-doped with iron and phosphorus. *Appl. Surf. Sci.* **2014**, *311*, 164–171.

233. Oh, W.-D.; Lok, L.-W.; Veksha, A.; Giannis, A.; Lim, T.-T. Enhanced photocatalytic degradation of bisphenol A with Ag-decorated S-doped $g-C_3N_4$ under solar irradiation: Performance and mechanistic studies. *Chem. Eng. J.* **2018**, *333*, 739–749.

234. Hu, S.; Ma, L.; Xie, Y.; Li, F.; Fan, Z.; Wang, F.; Wang, Q.; Wang, Y.; Kang, X.; Wu, G. Hydrothermal synthesis of oxygen functionalized S-P codoped $g-C_3N_4$ nanorods with outstanding visible light activity under anoxic conditions. *Dalton Trans.* **2015**, *44*, 20889–20897.

235. You, R.; Dou, H.; Chen, L.; Zheng, S.; Zhang, Y. Graphitic carbon nitride with S and O codoping for enhanced visible light photocatalytic performance. *RSC Adv.* **2017**, *7*, 15842–15850.

236. Xue, J.; Ma, S.; Zhou, Y.; Zhang, Z.; He, M. Facile Photochemical Synthesis of Au/Pt/$g-C_3N_4$ with Plasmon-Enhanced Photocatalytic Activity for Antibiotic Degradation. *ACS Appl. Mater. Interfaces* **2015**, *7*, 9630–9637.

237. Li, K.; Zeng, Z.; Yan, L.; Luo, S.; Luo, X.; Huo, M.; Guo, Y. Fabrication of platinum-deposited carbon nitride nanotubes by a one-step solvothermal treatment strategy and their efficient visible-light photocatalytic activity. *Appl. Catal. B Environ.* **2015**, *165*, 428–437.

238. Zhou, X.; Zhang, G.; Shao, C.; Li, X.; Jiang, X.; Liu, Y. Fabrication of g-C$_3$N$_4$/SiO$_2$-Au composite nanofibers with enhanced visible photocatalytic activity. *Ceram. Int.* **2017**, *43*, 15699–15707.

239. Tonda, S.; Kumar, S.; Shanker, V. Surface plasmon resonance-induced photocatalysis by Au nanoparticles decorated mesoporous g-C$_3$N$_4$ nanosheets under direct sunlight irradiation. *Mater. Res. Bull.* **2016**, *75*, 51–58.

240. Patnaik, S.; Sahoo, D.P.; Parida, K. An overview on Ag modified g-C$_3$N$_4$ based nanostructured materials for energy and environmental applications. *Renew. Sustain. Energy Rev.* **2018**, *82*, 1297–1312.

241. Ling, Y.; Liao, G.; Feng, W.; Liu, Y.; Li, L. Excellent performance of ordered Ag-g-C$_3$N$_4$/SBA-15 for photocatalytic ozonation of oxalic acid under simulated solar light irradiation. *J. Photochem. Photobiol. A Chem.* **2017**, *349*, 108–114.

242. Fu, Y.; Liang, W.; Guo, J.; Tang, H.; Liu, S. MoS$_2$ quantum dots decorated g-C$_3$N$_4$/Ag heterostructures for enhanced visible light photocatalytic activity. *Appl. Surf. Sci.* **2018**, *430*, 234–242.

243. Nagajyothi, P.C.; Pandurangan, M.; Vattikuti, S.V.P.; Tettey, C.O.; Sreekanth, T.V.M.; Shim, J. Enhanced photocatalytic activity of Ag/g-C$_3$N$_4$ composite. *Sep. Purif. Technol.* **2017**, *188*, 228–237.

244. Kumar, S.; Baruah, A.; Tonda, S.; Kumar, B.; Shanker, V.; Sreedhar, B. Cost-effective and eco-friendly synthesis of novel and stable N-doped ZnO/g-C$_3$N$_4$ core-shell nanoplates with excellent visible-light responsive photocatalysis. *Nanoscale* **2014**, *6*, 4830–4842.

245. Xiao, J.; Han, Q.; Xie, Y.; Yang, J.; Su, Q.; Chen, Y.; Cao, H. Is C$_3$N$_4$ Chemically Stable toward Reactive Oxygen Species in Sunlight-Driven Water Treatment? *Environ. Sci. Technol.* **2017**, *51*, 13380–13387.

246. Vellaichamy, B.; Periakaruppan, P. Catalytic hydrogenation performance of an in situ assembled Au@g-C$_3$N$_4$-PANI nanoblend: Synergistic inter-constituent interactions boost the catalysis. *New J. Chem.* **2017**, *41*, 7123–7132.

247. Wang, X.; Wang, G.; Chen, S.; Fan, X.; Quan, X.; Yu, H. Integration of membrane filtration and photoelectrocatalysis on g-C$_3$N$_4$/CNTs/Al$_2$O$_3$ membrane with visible-light response for enhanced water treatment. *J. Membr. Sci.* **2017**, *541*, 153–161.

248. Zhou, L.; Zhang, W.; Chen, L.; Deng, H.; Wan, J. A novel ternary visible-light-driven photocatalyst AgCl/Ag$_3$PO$_4$/g-C$_3$N$_4$: Synthesis, characterization, photocatalytic activity for antibiotic degradation and mechanism analysis. *Catal. Commun.* **2017**, *100*, 191–195.

249. Hu, S.; Li, Y.; Li, F.; Fan, Z.; Ma, H.; Li, W.; Kang, X. Construction of g-C$_3$N$_4$/Zn$_{0.11}$Sn$_{0.12}$Cd$_{0.88}$S$_{1.12}$ Hybrid Heterojunction Catalyst with Outstanding Nitrogen Photofixation Performance Induced by Sulfur Vacancies. *ACS Sustain. Chem. Eng.* **2016**, *4*, 2269–2278.

250. Wang, Y.; Yang, W.; Chen, X.; Wang, J.; Zhu, Y. Photocatalytic activity enhancement of core-shell structure g-C$_3$N$_4$@TiO$_2$ via controlled ultrathin g-C$_3$N$_4$ layer. *Appl. Catal. B Environ.* **2018**, *220*, 337–347.

251. Yang, Y.; Geng, L.; Guo, Y.; Meng, J.; Guo, Y. Easy dispersion and excellent visible-light photocatalytic activity of the ultrathin urea-derived g-C$_3$N$_4$ nanosheets. *Appl. Surf. Sci.* **2017**, *425*, 535–546.

252. Wei, X.-N.; Wang, H.-L.; Wang, X.-K.; Jiang, W.-F. Facile fabrication of mesoporous g-C$_3$N$_4$/TiO$_2$ photocatalyst for efficient degradation of DNBP under visible light irradiation. *Appl. Surf. Sci.* **2017**, *426*, 1271–1280.

253. Zhou, M.; Hou, Z.; Chen, X. Graphitic-C$_3$N$_4$ nanosheets: Synergistic effects of hydrogenation and n/n junctions for enhanced photocatalytic activities. *Dalton Trans.* **2017**, *46*, 10641–10649.

254. Lv, J.; Dai, K.; Zhang, J.; Geng, L.; Liang, C.; Liu, Q.; Zhu, G.; Chen, C. Facile synthesis of Z-scheme graphitic-C$_3$N$_4$/Bi$_2$MoO$_6$ nanocomposite for enhanced visible photocatalytic properties. *Appl. Surf. Sci.* **2015**, *358*, 377–384.

255. Jourshabani, M.; Shariatinia, Z.; Badiei, A. Synthesis and characterization of novel Sm$_2$O$_3$/S-doped g-C$_3$N$_4$ nanocomposites with enhanced photocatalytic activities under visible light irradiation. *Appl. Surf. Sci.* **2018**, *427*, 375–387.

256. Jourshabani, M.; Shariatinia, Z.; Badiei, A. Facile one-pot synthesis of cerium oxide/sulfur-doped graphitic carbon nitride (g-C$_3$N$_4$) as efficient nanophotocatalysts under visible light irradiation. *J. Colloid Interface Sci.* **2017**, *507*, 59–73.

257. Kim, W.J.; Jang, E.; Park, T.J. Enhanced visible-light photocatalytic activity of ZnS/g-C$_3$N$_4$ type-II heterojunction nanocomposites synthesized with atomic layer deposition. *Appl. Surf. Sci.* **2017**, *419*, 159–164.

258. Jourshabani, M.; Shariatinia, Z.; Badiei, A. Sulfur-Doped Mesoporous Carbon Nitride Decorated with Cu Particles for Efficient Photocatalytic Degradation under Visible-Light Irradiation. *J. Phys. Chem. C* **2017**, *121*, 19239–19253.

259. Li, Y.; Zhao, Y.; Fang, L.; Jin, R.; Yang, Y.; Xing, Y. Highly efficient composite visible light-driven Ag–AgBr/g-C₃N₄ plasmonic photocatalyst for degrading organic pollutants. *Mater. Lett.* **2014**, *126*, 5–8.

260. Zhang, S.; Li, J.; Zeng, M.; Zhao, G.; Xu, J.; Hu, W.; Wang, X. In Situ Synthesis of Water-Soluble Magnetic Graphitic Carbon Nitride Photocatalyst and Its Synergistic Catalytic Performance. *ACS Appl. Mater. Interfaces* **2013**, *5*, 12735–12743.

261. Ye, M.; Wang, R.; Shao, Y.; Tian, C.; Zheng, Z.; Gu, X.; Wei, W.; Wei, A. Silver nanoparticles/graphitic carbon nitride nanosheets for improved visible-light-driven photocatalytic performance. *J. Photochem. Photobiol. A Chem.* **2018**, *351*, 145–153.

262. Liu, W.; Qiao, L.; Zhu, A.; Liu, Y.; Pan, J. Constructing 2D BiOCl/C₃N₄ layered composite with large contact surface for visible-light-driven photocatalytic degradation. *Appl. Surf. Sci.* **2017**, *426*, 897–905.

263. Tang, L.; Jia, C.-T.; Xue, Y.-C.; Li, L.; Wang, A.-Q.; Xu, G.; Liu, N.; Wu, M.-H. Fabrication of compressible and recyclable macroscopic g-C₃N₄/GO aerogel hybrids for visible-light harvesting: A promising strategy for water remediation. *Appl. Catal. B Environ.* **2017**, *219*, 241–248.

264. Sun, M.; Zeng, Q.; Zhao, X.; Shao, Y.; Ji, P.; Wang, C.; Yan, T.; Du, B. Fabrication of novel g-C₃N₄ nanocrystals decorated Ag₃PO₄ hybrids: Enhanced charge separation and excellent visible-light driven photocatalytic activity. *J. Hazard. Mater.* **2017**, *339*, 9–21.

265. Akhundi, A.; Habibi-Yangjeh, A. Graphitic carbon nitride nanosheets decorated with CuCr₂O₄ nanoparticles: Novel photocatalysts with high performances in visible light degradation of water pollutants. *J. Colloid Interface Sci.* **2017**, *504*, 697–710.

266. Wang, J.-C.; Cui, C.-X.; Li, Y.; Liu, L.; Zhang, Y.-P.; Shi, W. Porous Mn doped g-C₃N₄ photocatalysts for enhanced synergetic degradation under visible-light illumination. *J. Hazard. Mater.* **2017**, *339*, 43–53.

267. Liang, Q.; Jin, J.; Zhang, M.; Liu, C.; Xu, S.; Yao, C.; Li, Z. Construction of mesoporous carbon nitride/binary metal sulfide heterojunction photocatalysts for enhanced degradation of pollution under visible light. *Appl. Catal. B Environ.* **2017**, *218*, 545–554.

268. Yang, H.; Zhang, S.; Cao, R.; Deng, X.; Li, Z.; Xu, X. Constructing the novel ultrafine amorphous iron oxyhydroxide/g-C₃N₄ nanosheets heterojunctions for highly improved photocatalytic performance. *Sci. Rep.* **2017**, *7*, 8686, doi:10.1038/s41598-017-09283-1.

269. Chen, F.; Li, D.; Luo, B.; Chen, M.; Shi, W. Two-dimensional heterojunction photocatalysts constructed by graphite-like C₃N₄ and Bi₂WO₆ nanosheets: Enhanced photocatalytic activities for water purification. *J. Alloy. Compd.* **2017**, *694*, 193–200.

270. Yang, Y.; Chen, J.; Mao, Z.; An, N.; Wang, D.; Fahlman, B.D. Ultrathin g-C₃N₄ nanosheets with an extended visible-light-responsive range for significant enhancement of photocatalysis. *RSC Adv.* **2017**, *7*, 2333–2341.

271. Zhou, D.; Chen, Z.; Yang, Q.; Dong, X.; Zhang, J.; Qin, L. In-situ construction of all-solid-state Z-scheme g-C₃N₄/TiO₂ nanotube arrays photocatalyst with enhanced visible-light-induced properties. *Sol. Energy Mater. Sol. Cells* **2016**, *157*, 399–405.

272. Wang, P.; Lu, N.; Su, Y.; Liu, N.; Yu, H.; Li, J.; Wu, Y. Fabrication of WO₃@g-C₃N₄ with core@shell nanostructure for enhanced photocatalytic degradation activity under visible light. *Appl. Surf. Sci.* **2017**, *423*, 197–204.

273. Wang, B.; Di, J.; Liu, G.; Yin, S.; Xia, J.; Zhang, Q.; Li, H. Novel mesoporous graphitic carbon nitride modified PbBiO₂Br porous microspheres with enhanced photocatalytic performance. *J. Colloid Interface Sci.* **2017**, *507*, 310–322.

274. Cai, Z.; Zhou, Y.; Ma, S.; Li, S.; Yang, H.; Zhao, S.; Zhong, X.; Wu, W. Enhanced visible light photocatalytic performance of g-C₃N₄/CuS p-n heterojunctions for degradation of organic dyes. *J. Photochem. Photobiol. A Chem.* **2017**, *348*, 168–178.

275. Sun, Z.; Li, C.; Du, X.; Zheng, S.; Wang, G. Facile synthesis of two clay minerals supported graphitic carbon nitride composites as highly efficient visible-light-driven photocatalysts. *J. Colloid Interface Sci.* **2018**, *511*, 268–276.

276. Jiang, L.; Yuan, X.; Zeng, G.; Wu, Z.; Liang, J.; Chen, X.; Leng, L.; Wang, H.; Wang, H. Metal-free efficient photocatalyst for stable visible-light photocatalytic degradation of refractory pollutant. *Appl. Catal. B Environ.* **2018**, *221*, 715–725.

277. Chen, Q.; Hou, H.; Zhang, D.; Hu, S.; Min, T.; Liu, B.; Yang, C.; Pu, W.; Hu, J.; Yang, J. Enhanced visible-light driven photocatalytic activity of hybrid ZnO/g-C₃N₄ by high performance ball milling. *J. Photochem. Photobiol. A Chem.* **2018**, *350*, 1–9.

278. Vidyasagar, D.; Ghugal, S.G.; Kulkarni, A.; Mishra, P.; Shende, A.G.; Jagannath; Umare, S.S.; Sasikala, R. Silver/Silver(II) oxide (Ag/AgO) loaded graphitic carbon nitride microspheres: An effective visible light active photocatalyst for degradation of acidic dyes and bacterial inactivation. *Appl. Catal. B Environ.* **2018**, *221*, 339–348.

279. Li, C.; Sun, Z.; Zhang, W.; Yu, C.; Zheng, S. Highly efficient g-C_3N_4/TiO_2/kaolinite composite with novel three-dimensional structure and enhanced visible light responding ability towards ciprofloxacin and *S. aureus*. *Appl. Catal. B Environ.* **2018**, *220*, 272–282.

280. Zhu, Z.; Huo, P.; Lu, Z.; Yan, Y.; Liu, Z.; Shi, W.; Li, C.; Dong, H. Fabrication of magnetically recoverable photocatalysts using g-C_3N_4 for effective separation of charge carriers through like-Z-scheme mechanism with Fe_3O_4 mediator. *Chem. Eng. J.* **2018**, *331*, 615–625.

281. Deng, Y.; Tang, L.; Zeng, G.; Wang, J.; Zhou, Y.; Wang, J.; Tang, J.; Wang, L.; Feng, C. Facile fabrication of mediator-free Z-scheme photocatalyst of phosphorous-doped ultrathin graphitic carbon nitride nanosheets and bismuth vanadate composites with enhanced tetracycline degradation under visible light. *J. Colloid Interface Sci.* **2018**, *509*, 219–234.

282. Xiao, T.; Tang, Z.; Yang, Y.; Tang, L.; Zhou, Y.; Zou, Z. In situ construction of hierarchical WO_3/g-C_3N_4 composite hollow microspheres as a Z-scheme photocatalyst for the degradation of antibiotics. *Appl. Catal. B Environ.* **2018**, *220*, 417–428.

283. Shao, H.; Zhao, X.; Wang, Y.; Mao, R.; Wang, Y.; Qiao, M.; Zhao, S.; Zhu, Y. Synergetic activation of peroxymonosulfate by Co_3O_4 modified g-C_3N_4 for enhanced degradation of diclofenac sodium under visible light irradiation. *Appl. Catal. B Environ.* **2017**, *218*, 810–818.

284. Wang, F.; Wang, Y.; Feng, Y.; Zeng, Y.; Xie, Z.; Zhang, Q.; Su, Y.; Chen, P.; Liu, Y.; Yao, K.; et al. Novel ternary photocatalyst of single atom-dispersed silver and carbon quantum dots co-loaded with ultrathin g-C_3N_4 for broad spectrum photocatalytic degradation of naproxen. *Appl. Catal. B Environ.* **2018**, *221*, 510–520.

285. Sun, C.; Chen, C.; Ma, W.; Zhao, J. Photocatalytic debromination of decabromodiphenyl ether by graphitic carbon nitride. *Sci. China Chem.* **2012**, *55*, 2532–2536.

286. Lu, C.; Zhang, P.; Jiang, S.; Wu, X.; Song, S.; Zhu, M.; Lou, Z.; Li, Z.; Liu, F.; Liu, Y.; et al. Photocatalytic reduction elimination of UO_2^{2+} pollutant under visible light with metal-free sulfur doped g-C_3N_4 photocatalyst. *Appl. Catal. B Environ.* **2017**, *200*, 378–385.